

# Characteristic Mode Analysis for Multiport Antennas

by  
Wei Su

A thesis submitted to the University of London for the  
degree of Doctor of Philosophy

Department of Electronic Engineering  
Queen Mary, University of London  
United Kingdom

July 2020

**TO MY FAMILY**

# Declaration

I, Wei Su, confirm that the research included within this thesis is my own work or that where it has been carried out in collaboration with, or supported by others, that this is duly acknowledged below and my contribution indicated. Previously published material is also acknowledged below.

I attest that I have exercised reasonable care to ensure that the work is original, and does not to the best of my knowledge break any UK law, infringe any third partys copyright or other Intellectual Property Right, or contain any confidential material.

I accept that Queen Mary University of London has the right to use plagiarism detection software to check the electronic version of the thesis.

I confirm that this thesis has not been previously submitted for the award of a degree by this or any other university.

The copyright of this thesis rests with the author and no quotation from it or information derived from it may be published without the prior written consent of the author.

Signature: Wei Su

Date:20/07/2020

# Abstract

This thesis focuses on the research to overcome challenges in using the theory of characteristic mode (TCM) for multiport antennas. TCM is particularly useful for exploiting multiple radiations on the same structure, making it well-suited for dealing with multiport antennas. However, when multiple characteristic modal radiation are activated, many of the previous designs lack a satisfactory frequency band coverage, and the number of antenna ports is often limited. Furthermore, when applying TCM to analyse the coupling in multiport antennas, the previous methods is not sufficiently clear and does not accommodate a higher number of ports. On the other hand, for a typical dual-polarized Base station (BS) antenna whose radiation pattern is more worthy of concern than coupling and the number of ports, its ground size is typically much larger than the operating wavelength, resulting in a considerable number of irrelevant characteristic modes (CMs) that can disrupt the analysis.

In this thesis, several novel research approaches are proposed to overcome the aforementioned challenges and further exploit the application of TCM in multiport antennas.

Firstly, a novel planar hexagonal antenna design, developed solely based on the principles of TCM, is proposed. The study centers around the degenerate characteristic mode (CM) pairs of symmetrical shape and their excitation during the design process. By harnessing a higher number of degenerate CM pairs, the proposed design achieves a satisfactory bandwidth among four ports and a satisfying port-to-port isolation.

The second proposal introduces a method to evaluate the radiation energy and mutual coupling. This new perspective enables the enhancement of the operating band and isolation in arbitrary multiport antennas. As a result, the design and analysis of multiport antennas become easier.

In line with this method, a four-port hexagonal antenna is later proposed. This four-port hexagonal antenna consists of a planar hexagonal plate, vertical tapered baluns, and a feeding network at the ground plane. The antenna exhibits a broadband impedance bandwidth while minimizing mutual coupling among its ports.

The last contribution focuses on a dual-port antenna from a BS array. It examines the improvement of radiation performance of the antenna. Instead of the conventional TCM, the sub-



structure TCM is employed to isolate the antenna unit from its ground and study the variations of its CMs as the frequency increases. The irrelevant CMs are thus eliminated. Modifications have been implemented to enhance the beamwidth stability across the entire band.

# Acknowledgments

I cannot express enough thanks to my supervisor, Prof. Yue Gao for the continued support and encouragement. I offer my sincere appreciation for your invaluable help, patience and guidance in the research topics.

I would also like to thank Prof. Clive Parini, my co-supervisor and Dr. Khalid Rajab, my stage examiner, for your hard work and supports.

The completion of my research cannot have been accomplished without the support of my colleagues: Qianyun, Xingjian, Qiao and Ben and all the other members of the Antennas and Electromagnetic Group. Thank you for offering precious help and I cannot forget inspiring conversations with you in the past three years. For Haoran, Shaker, I admire your talent and genius ideas and appreciate those suggestions and help in the my research. Hope your all have a bright future!

Finally, to my beloved family, it was a great comfort and relief to know that you were always there for me. With your love and support, I felt fulfilled. Thanks for your support and understanding.

# Table of Contents

<b>Declaration</b>	<b>i</b>
<b>Abstract</b>	<b>ii</b>
<b>Acknowledgments</b>	<b>iv</b>
<b>Table of Contents</b>	<b>v</b>
<b>List of Figures</b>	<b>ix</b>
<b>List of Tables</b>	<b>xvi</b>
<b>List of Abbreviations</b>	<b>xvi</b>
<b>List of Mathematical Symbols</b>	<b>xix</b>
<b>1 Introduction</b>	<b>1</b>
1.1 Background and Motivation . . . . .	1
1.2 Problems to be Solved and Contributions . . . . .	4
1.3 Outline of the Thesis . . . . .	5
References . . . . .	6
<b>2 Background</b>	<b>10</b>

2.1	Theory of Characteristic Mode . . . . .	10
2.1.1	Characteristic Mode Basis . . . . .	11
2.1.2	Significance of Eigenvalue . . . . .	13
2.1.3	Excitation of Characteristic Mode . . . . .	14
2.1.4	Q Factor with TCM . . . . .	17
2.1.5	State-of-art Review on Antenna Research with TCM . . . .	20
2.2	Multiport Antenna for MIMO System . . . . .	22
2.2.1	MIMO System . . . . .	22
2.2.2	State-of-art Review on MIMO Antenna Research with TCM	23
2.3	Dual-polarized Base Station Antenna . . . . .	28
2.3.1	Base Station Antenna . . . . .	28
2.3.2	State-of-art Review BS Antenna Design with TCM . . . .	29
2.4	Summary . . . . .	30
	References . . . . .	30
<b>3</b>	<b>Characteristic Analysis on Hexagonal Shapes</b>	<b>38</b>
3.1	Introduction . . . . .	38
3.2	Degenerate Characteristic Modes on Symmetrical Plates . . . . .	40
3.3	Excitation of Degenerate Modes on Hexagonal Plate . . . . .	46
3.3.1	Adding Slots for CM Excitation . . . . .	46
3.3.2	Performance of the Hexagonal Antenna . . . . .	52
3.4	Lumped Loading to Tune the Common Band . . . . .	55
3.5	Size Reduction with Edges Slots . . . . .	58
3.6	Alternative Distribution Loading . . . . .	61
3.7	Summary . . . . .	64
	References . . . . .	66
<b>4</b>	<b>Radiation Energy and Mutual Coupling Evaluation</b>	<b>70</b>

4.1	Introduction . . . . .	70
4.2	Mutual Coupling Evaluation in the CMA Sense . . . . .	71
4.3	MEOC for Multimode MIMO System . . . . .	75
4.4	Numerical Examples . . . . .	78
4.4.1	Coupling Analysis on a Twin-dipole System . . . . .	78
4.4.2	Coupling Analysis on a Four-port Square Plate . . . . .	83
4.5	Summary . . . . .	88
	References . . . . .	88
<b>5</b>	<b>MEOC Application on the Design of Multiport Antenna</b>	<b>92</b>
5.1	Introduction . . . . .	92
5.2	Application Example with MEOC . . . . .	93
5.2.1	MEOC Analysis for a Square Plate . . . . .	93
5.2.2	Impedance Matching for Hexagonal Plate . . . . .	96
5.3	Antenna Realization and Measurement . . . . .	103
5.3.1	Feeding Network Design . . . . .	103
5.3.2	Final Combination . . . . .	104
5.3.3	Simulated and Measured Results . . . . .	111
5.4	Summary . . . . .	113
	References . . . . .	113
<b>6</b>	<b>Base Station Antenna Radiation Control with Sub-Structure</b>	
	<b>TCM</b>	<b>117</b>
6.1	Introduction . . . . .	117
6.2	Sub-structure Characteristic Mode Theory and BS Antennas . . . .	119
6.2.1	Sub-structure Characteristic Mode Theory . . . . .	119
6.2.2	Sub-structure TCM Analysis on Base Station Antennas . . .	123
6.2.3	Modification to Improve Radiation Stability . . . . .	131

6.3	Summary . . . . .	133
	References . . . . .	133
<b>7</b>	<b>Conclusion and Future Work</b>	<b>137</b>
7.1	Conclusion . . . . .	137
7.2	Future Work . . . . .	138
7.2.1	Radiation Pattern Synthesis . . . . .	139
7.2.2	Applications on MIMO Antenna . . . . .	139
7.2.3	Broadband Antennas Design . . . . .	139
<b>Appendix A</b>	<b>Author's publications</b>	<b>140</b>

# List of Figures

1.1	Schematic view of multiport antenna radiation. . . . .	3
2.1	Partial view of the feeding on a strip drawn with FEKO. . . . .	15
2.2	A handset chassis with two CMs separately excited by 2 ports. Port 1 is excited by a folded monopole and port 2 is excited by a T-shape strip with the source between its pin and chassis . . . . .	25
2.3	A seven-layer structure, three CMs of which are excited through 3 sets of stripline feeding network. The whole feeding network is inside the rectangle box . . . . .	25
2.4	The massive MIMO antenna. Four CMs are excited through a multiport antenna. The antenna is fed by a feeding network at its bottom. A massive MIMO array with $11 \times 11$ is formed with the element . . . . .	26
3.1	Eigenvalue tracked at $1 \sim 6$ GHz in decibel scale and modal current distributions at their resonant frequencies of (a) a triangular plate, (b) a rectangular plate, and (c) a square plate. At resonance, eigenvalues that are close to zero turn into sharp minimum. . . . .	43
3.2	Eigenvalue tracking in decibel scale and modal current distributions at their resonant frequencies of a hexagonal plate. . . . .	44

3.3	(a) Eigenvalue tracking in decibel scale and modal current distributions at their resonant frequencies of the hexagonal plate with inserted slots, (b) eigenvalue tracking in linear representation, (c) MS curves and modal current of Mode 3 and the third degenerate pair. . . . .	48
3.4	The normalized modal radiation patterns of discussed CMs at their resonant frequencies. From top to bottom are the original hexagonal plate, the hexagonal plate with inserted straight slots, the slotted plate with central cut, and the size-reduced slotted plate. . . . .	49
3.5	(a) Port layout and numbering on the antenna plate, (b) Feed configurations to excite five CMs. . . . .	52
3.6	The circuit connection to feed the hexagonal antenna in CST's Design Studio. . . . .	53
3.7	Simulated S-parameters of the slotted hexagonal plate in Fig. 3.3. The relative bandwidth of the overlapping band is 36.7%. . . . .	54
3.8	(a) Eigenvalue tracking in decibel scale and modal current distributions of the slotted plate with central slot, (b) MS curves and modal current of the third degenerate pair, and (c) the hexagonal plate with edge ports and loading positions $A \sim F$ . . . . .	56
3.9	Evolution of the hexagonal antenna: (a) the slotted antenna, (b) the slotted antenna with inductive loadings. . . . .	57
3.10	The effect of inductive loading value on S-parameter of (a) port 1' and (b) port 3'. It shows that loading controls the second resonance of port 1', while shows lesser influence on port 2'. . . . .	57



3.11	Simulated S-parameters and radiation efficiencies of the slotted hexagonal antenna with loading inductors in Fig. 3.9 (b). The relative bandwidth of the overlapping band is 42%. Radiation efficiencies fluctuate within a range of 96% $\sim$ 99% in the common band. . . .	58
3.12	Simulated S-parameters and radiation efficiencies of the size-reduced slotted hexagonal antenna with loading inductors in Fig. 3.13 (c). The relative bandwidth of the overlapping band is 45.5%. Radiation efficiencies fluctuate within a range of 94% $\sim$ 99% in the common band. . . . .	59
3.13	Evolution of the hexagonal antenna: (a) the slotted antenna, (b) the slotted antenna with inductive loadings, (c) the slotted antenna with six inductive loadings and edge slots (d) the slotted antenna with distributed loadings and edge slots. . . . .	60
3.14	Eigenvalue tracking in decibel scale and modal current distributions of the slotted plate with central slot and edge slots. The modal resonant frequencies have moved to a lower frequency compared with those in Fig. 3.8. . . . .	61
3.15	Simulated total directivity w.r.t. Ports 1' $\sim$ 4' of the (a) slotted hexagonal antenna with lumped inductors, and (b) slotted hexagonal antenna with distributed inductors at central frequency 2.8 GHz. . . . .	62
3.16	Simulated S-parameters and radiation efficiencies of the size-reduced slotted hexagonal antenna with distributed inductors in Fig. 3.13 (d). The relative bandwidth of the overlapping band is 45.5%. Radiation efficiencies fluctuate within a range of 94% $\sim$ 99% in the common band. . . . .	64
4.1	Schematic view of multiport antenna radiation. . . . .	75

4.2	Two dipoles with different length are placed in space with a distance of 75 <i>cm</i> . The operating frequency is Ant. 2's resonance (280 MHz)	79
4.3	MEOC analysis and modal significance of the twin-dipole at 280 MHz. The order and naming rules of CMs is determined by the absolute values of their corresponding eigenvalues in ascending order at 280 MHz. The figure is plotted in decibel scale. It is shown that radiation by Ant. 1 is dominated by Mode 2 and 4. For Ant. 2, the dominant modes is Mode 1. . . . .	81
4.4	The stepped slot structure. (a) the structure of the slot (b) the S-parameter of this slot. The length of slot is 30 <i>mm</i> . This slot is fed at its end and works at 3 ~ 6.5 GHz. . . . .	84
4.5	Left: Four feed schemes through four different ports 1' ~ 4' for rectangular plates. The antenna ports are located at the end of each slot, which are named as port 1 ~ 4.  Right: MEOC comparison among the four input ports at 4.5 GHz. The order of CMs is determined by the absolute values of their corresponding eigenvalues in ascending order. The comparison clearly shows that port 2 and 4 are strongly coupled and that they mainly coupled at Mode 10, 11, 12, and 16. . . . .	87
5.1	Four feed schemes through four different ports 1' ~ 4' for rectangular plate and hexagonal plate. The antenna ports are located at the end of each slot, which are named as port 1 ~ 4 (rectangle) or port 1 ~ 6 (hexagon). . . . .	95

5.2	MEOC analysis of rectangular plate at 4.5 GHz. The order and naming rules of CMs is determined by the absolute values of their corresponding eigenvalues in ascending order. It is shown that radiation by port 1' is dominated by Mode 4, 9 and 13. For port 2', the dominant modes are Mode 9 ~ 12 and 16, 17. For port 3', they are 6, 8 and 14. And finally, for port 4', they are 10 ~ 12 and 16, 18. The surface current for the shared dominant modes of port 2 and 4 are also illustrated. . . . .	96
5.3	MEOC for hexagonal plate w/ and w/o extra slots. (a) MEOC and MS for the original plate at 4.5 GHz (b) dominant modes for port 3', (c) dominant modes after adding slots, (d)MEOC and MSs for the modified plate. The size for the extra slot is 32 mm and width 3 mm. . . . .	97
5.4	Reflection and transmitting coefficients of three mentioned structure (rectangular plate, hexagonal plate and hexagonal plate with extra slots). (a) Coupling among four ports for three structures. (b) Self reflection coefficients for all ports on hexagonal plates. . . . .	98
5.5	Comparison of dominant modes between two hexagonal plates with (W/) or without (W/O) extra slots. (a) the eigenvalue of port 3's dominant modes at 2.6 ~ 6.5 GHz of two hexagonal plates (b) the equivalent circuit for two hexagonal plates with reference to port 3'. . . . .	99
5.6	The feeding network with its performance. (a) The top view of feeding network. (b) The detail of the 180° hybrid. The feeding network has four input ports with SMA connector. Its ends connect to six Balun structures which are vertical to ground. The corresponding parameters are listed in Table 5-B. . . . .	105
5.7	Simulation performance of the feeding network . . . . .	106

5.8	Phase responses of the feeding network . . . . .	106
5.9	The Balun design and its configuration. It transforms the impedance from the antenna slots to the standard $50\ \Omega$ . . . . .	107
5.10	The final combination of antenna, balun and feeding network. (a) exploded view of the design (b) perspective view and back view. The antenna is fed through four SMA connectors on the bottom side of the ground. $h_1 = 0.813\ mm$ , $h_2 = 0.518\ mm$ and $H = 23\ mm$	108
5.11	The simulation inserting loss of the related Balun structure. For the two-port system, the result is satisfying. . . . .	108
5.12	The transversal cut of the combination of antenna, Balun and feeding network layers. The substrate of the Balun is extended, creating slots of the same width as the antenna plate, allowing the new substrate slots to interlock with the antenna plates. This design makes the whole structure fixed stable. . . . .	109
5.13	The prototype of proposed antenna (a) Perspective view. (b) Back view. . . . .	109
5.14	The scattering parameters of the antenna. It works well at 3~6 GHz, with coupling ( $S_{21}$ ) lower than $-20\ dB$ . (a) port reflection (b) isolation among ports. . . . .	110
5.15	Far-field pattern of all four ports at three frequencies (3 GHz, 4.6 GHz, and 6 GHz) at y-z plane . . . . .	112
5.16	Realized Gain of all ports at 3 ~ 6 GHz . . . . .	112

6.1	(a) The original BS array configuration [18]. (b) The original BS antenna unit [18], where the antenna is fed by two coaxial cables. The feeding coaxial cables are pointed out by arrows. Another two conducting cables are added for symmetry. (c) The antenna unit with feed cable omitted. The new feeding configuration enables the calculation of MEOC. (d) The aerial view of the antenna. (e) Two different views of the ground plate with two extra strips to improve beamwidth stability. The relevant parameters have been annotated in the figure. . . . .	124
6.2	The comparison of HPBW and Gain before and after the modification. The details for the extra strips can be found in Fig. 6.1(e). . .	125
6.3	The dominant mode's occupied power (Left) and pattern (Right) variation with frequency. From top to bottom, the tracking result of modes from low frequency 1.5 GHz to high frequency 3 GHz is illustrated. . . . .	128
6.4	The dominant modes current and pattern comparison before and after the modification at 2.7 GHz. . . . .	130
6.5	The VSWR and $S_{21}$ comparison before and after the modification.	131

# List of Tables

3-A	Design parameters for the modified antenna in Fig. 3.13(mm)	63
3-B	Comparison of several four-port antennas	65
4-A	The real part of modal admittance (MA) of the first 6 modes of the twin-dipole system [6]	82
4-B	The real part of modal admittance of the first 20 modes of the square antenna	91
5-A	Parameters for the equivalent circuits in Fig. 5.5 (b) (4.5 GHz)	102
5-B	Parameters for feeding network in Fig. 5.6	104
5-C	Parameters for feeding network in Fig. 5.6	113
5-D	Comparison of several four-port antennas	114
6-A	The characteristic angles of the first 16 modes of the BS antenna composed by TCM and sub-structure TCM (sub-TCM) at 2.5 GHz. The modes capable of radiating are written in bold style.	127

# List of Abbreviations

CCE	Capacitive Coupling Element
CM	Characteristic Mode
CMA	Characteristic Mode Analysis
ECC	Envelope Correlation Coefficient
EMI	Electromagnetic Interference
E-Plane	Electric Field Plane
HPBW	Half Power Beamwidth
H-Plane	Magnetic Field Plane
ICE	Inductive Coupling Element
IMT	International Mobile Telecommunication
MA	Modal Admittance
MEC	Modal Excitation Coefficient
MEOC	Modal Energy Occupied Coefficient
MIMO	Multiple Input, Multiple Output
MMA	Modal Mutual Admittance
MOM	Method of Moments

MS	Modal Significance
MSA	Modal Self Admittance
MWC	Modal Weighting Coefficient
PEC	Perfect Electric Conductor
PIFA	Planar Inverted-F Antenna
RF	Radio Frequency
RWG	Rao-Wilton-Glisson
SIW	Substrate Integrated Waveguide
SLL	Side Lobe Level
SMA Connector	Sub-Miniature Version A Connector
SNR	Signal to Noise Ratio
TCM	Theory of Characteristic Mode
VSWR	Voltage Standing Wave Ratio



# List of Mathematical Symbols

$ a $	Absolute Value
$\oint$	Closed Surface Integral
$\langle x, y \rangle$	Inner Product
$A^{-1}$	Inverse Matrix
$A^*$	Matrix Conjugate Transpose
$\sqrt{a}$	Square Root
$\Sigma$	Summation

# Chapter 1

## Introduction

### 1.1 Background and Motivation

Recently, research and development on the design of multiport antennas has attracted considerable attention. [1–3] With multiple modes/patterns excited by each port and radiating on one structure simultaneously [4], the antenna avoids the large spatial requirement of a conventional multiple-input multiple-output (MIMO) array and thus can be a competitive candidate in the construction of MIMO and Massive MIMO systems. However, these advantages also bring challenges in antenna design. All ports need to be well-matched at the operating band while maintaining high port-to-port isolation. Conventional examples include the classical dual-polarized antennas [5–8], the multimode circular/ring patch antennas utilizing a series of patch modes [4, 9, 10], and realizations with symmetric arrays of identical antennas which make use of the orthogonality of the eigenmode feeding network matrix [11, 12]. The majority of those realizations either have limited number of input ports (usually a maximum of two ports), or only achieve a narrow frequency

bandwidth [4, 9, 10, 13]. Besides, most of those applications have many limited conditions, e.g., antenna types, or symmetric placement. Conventional analysis methods tend to focus more on the mutual coupling aspect and often overlook other potential resonances. However, it is necessary to exploit these hidden resonances in order to utilize more input ports and achieve a wider operating band. Therefore, the theory of characteristic mode (TCM) is employed to design multi-mode antennas, making it a natural approach to address this challenge [1, 14], and since then, multiport antenna design has become one of the most popular applications of TCM. Providing unique insights into operating mechanisms of antennas, TCM significantly benefits the design of multiport antenna design process.

The most unique and interesting part of applying TCM in the design of multiport antenna is the instinct insight introduced by TCM. In the TCM analysis, the surface current  $\mathbf{J}$  of an antenna under arbitrary frequency and feeding methods can be regarded as a weighted composition of a series of modal current  $\mathbf{J}_n$ , which can be written as [15], [16]:

$$\mathbf{J} = \sum_{n=1}^{\infty} \frac{V_n^i \mathbf{J}_n}{1 + j\omega_n} \quad (1.1)$$

in which  $V_n^i$  is called the modal excitation coefficient (MEC) and lies on excitation methods.

Moreover, the far field radiating by each modal current is orthogonal to each other, i.e., [15]

$$\frac{1}{\eta} \oint\!\!\!\oint_{S_{infty}} \mathbf{E}_m \cdot \mathbf{E}_n^* ds = \delta_{mn} \quad (1.2)$$

$$\frac{1}{\eta} \oint\!\!\!\oint_{S_{infty}} \mathbf{H}_m \cdot \mathbf{H}_n^* ds = \delta_{mn} \quad (1.3)$$

where  $\delta_{mn}$  is the Kronecker delta (0 if  $m \neq n$ , and 1 if  $m=n$ ).

Hence, TCM research on multiport antenna focuses on dividing out, studying and

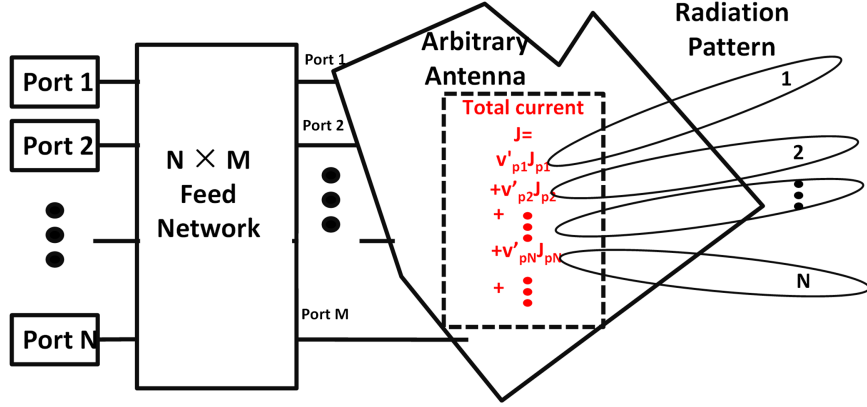


Figure 1.1: Schematic view of multiport antenna radiation.

utilizing those orthogonal modes. There has been quite a lot applications about that and in this thesis they can be roughly summarized with a network model. Suppose there are  $N$  ports feeding an  $M$ -port single antenna through an  $N \times M$  feeding network, as shown in Fig. 1.1. With careful selection of the feeding location and maximizing the MEC, each port can be independently dominated by one or more characteristic modes (CMs). In this way, port  $N$  maximizes  $v'_{pN}$ , while has little influence on other  $V'_n$ . This leads to a multimode antenna radiating  $N$  kinds of radiation pattern. Considering the far field orthogonality of different CMs, this multimode antenna thus has high port-to-port isolation and the potential of becoming a multiport antenna.

In conclusion, TCM proves to be an excellent approach for studying and designing multiport antennas with high isolation. In comparison to traditional methods, the modes in TCM are real current modes that can be visualized and accurately calculated. Additionally, the ability to analyze the variations of each mode makes TCM suitable for wideband applications. Therefore, studying TCM in the context of multiport antennas holds significant importance.

## 1.2 Problems to be Solved and Contributions

When designing multiport antennas using TCM, the ideal scenario is to have each port radiate pure CM(s) that will not be used by other ports. This simplifies the design process as it allows the designer to easily determine which CMs to choose or avoid. However, in most multiport antenna cases, the situation becomes more complex. At low frequencies ( $\lambda \geq 2 \times \text{antenna size}$ ), there are not enough CMs available to accommodate more than two ports or wide bandwidth. Therefore, the frequency needs to be increased in order to excite higher order CMs that can meet the requirements for the number of ports and bandwidth. The number of potentially radiating CMs increases greatly as the frequency goes up. Consequently, each port of multiport antennas will not be dominated by just one CM, especially in a relatively wide band. This could affect the bandwidth of each port and the mutual coupling among them. It is the main reason why the previous examples lack a satisfied operating frequency band, or have limitations on the maximum number of ports.

Moreover, when studying coupling in multiport antennas, regardless of whether the antenna is designed using TCM or pre-determined, there is currently a scarcity of evaluation methods. The potential application of TCM needs to be explored further, as it already offers the capability to linearly decompose various antenna parameters, such as Q factor and radiation pattern.

On the other hand, for a typical dual-polarized base station (BS) antenna, the challenges of isolation and port number are no longer the primary problem. Instead, the instability of radiation pattern over a wide frequency band becomes a significant challenge. The conventional TCM can be employed to analyse the radiation characteristics. However, when dealing with high frequencies and large ground sizes, numerous unnecessary CMs occurs, thereby disrupting the analysis.

In this thesis, the following contributions are proposed to meet those challenges

- The relationship between degenerated CM pairs and the symmetry of planar shapes is discussed, and a hexagonal shape was chosen and transformed to an antenna under the guidance of TCM to demonstrate that wisely selected degenerated CM pairs can result in a wider bandwidth.
- The second proposal is a novel method to evaluate the radiation energy and mutual coupling. With the new perspective brought by this method, the operating band and mutual coupling in a multiport antenna can be improved.
- The evaluation method is then utilized to analyse and improve the performance of a four-port antenna. The whole antenna works in  $3 \sim 6$  GHz and all its four ports are well-matched with high port-to-port isolation.
- The last contribution looks at improving the radiation performance of a dual-port antenna unit from a base station array. Sub-structure TCM instead of the conventional one, is used to isolate the antenna unit from its ground and study its CM variations when frequency increases. This section will demonstrate how beamwidth stability can be improved by making modifications on the ground plane rather than the antenna itself.

## 1.3 Outline of the Thesis

**Chapter 2** covers an introduction to the theoretical basics of TCM. The state-of-art research on TCM research and multiport antenna applications are also included.

**Chapter 3** analyses CMs of several symmetrical shapes and then presents a hexagon antennas with six ports designed for multimode usage.

**Chapter 4** proposes a new method to evaluate radiation energy and mutual coupling based on TCM. This method is then extended to multiport antenna system.

**Chapter 5** presents a multiport hexagonal antenna with its prototype to validate the previous evaluation method. In both simulation and measurement, the antenna works from 3 GHz to 6 GHz, and it realizes a high isolation between each port.

**Chapter 6** proposes a method to utilize an alternative version of TCM to improve the radiation performance of a dual-port base station antenna.

**Chapter 7** presents the conclusion and some thoughts for future work.

## References

- [1] E. Antonino-Daviu, M. Cabedo-Fabres, M. Gallo, M. Ferrando-Bataller, and M. Bozzetti, “Design of a multimode mimo antenna using characteristic modes,” in *2009 3rd European Conference on Antennas and Propagation*, pp. 1840–1844.
- [2] B. K. Lau, M. Capek, and A. M. Hassan, “Characteristic modes: Progress, overview, and emerging topics,” *IEEE Antennas and Propagation Magazine*, vol. 64, no. 2, pp. 14–22, 2022.
- [3] J. J. Adams, S. Genovesi, B. Yang, and E. Antonino-Daviu, “Antenna element design using characteristic mode analysis: Insights and research directions,”

- IEEE Antennas and Propagation Magazine*, vol. 64, no. 2, pp. 32–40, 2022.
- [4] T. T. Q and S. K. Sharma, “Radiation characteristics of a multimode concentric circular microstrip patch antenna by controlling amplitude and phase of modes,” *IEEE Transactions on Antennas and Propagation*, vol. 60, no. 3, pp. 1601–1605, Dec. 2012.
- [5] C.-X. Mao, S. Gao, Y. Wang, F. Qin, and Q.-X. Chu, “Multimode resonator-fed dual-polarized antenna array with enhanced bandwidth and selectivity,” *IEEE Transactions on Antennas and Propagation*, vol. 63, no. 12, pp. 5492–5499, 2015.
- [6] H. Sun, C. Ding, and Y. J. Guo, “A wideband base station antenna with reduced beam squint,” in *12th European Conference on Antennas and Propagation (EuCAP 2018)*, 2018, pp. 1–5.
- [7] Y. Cui, L. Wu, and R. Li, “Bandwidth enhancement of a broadband dual-polarized antenna for 2g/3g/4g and imt base stations,” *IEEE Transactions on Antennas and Propagation*, vol. 66, no. 12, pp. 7368–7373, 2018.
- [8] Y. Liu, H. Yi, F.-W. Wang, and S.-X. Gong, “A novel miniaturized broadband dual-polarized dipole antenna for base station,” *IEEE Antennas and Wireless Propagation Letters*, vol. 12, pp. 1335–1338, 2013.
- [9] D. Yang, Y. Wen, M. Chen, and H. Zeng, “A multimode annular ring patch antenna for mimo applications,” in *2015 IEEE 6th International Symposium on Microwave, Antenna, Propagation, and EMC Technologies (MAPE)*. IEEE, 2015, pp. 197–200.
- [10] R. Eva, Q. Oscar, and S. Matilde, “Compact multimode patch antennas for mimo applications,” *IEEE Antennas and Propagation Magazine*, vol. 50, no. 2, pp. 197–205, July 2008.
- [11] J. C. Coetzee and Y. Yu, “Port decoupling for small arrays by means of an eigenmode feed network,” *IEEE Transactions on Antennas and Propagation*,



- vol. 56, no. 6, pp. 1587–1593, 2008.
- [12] L. Zhao and K.-L. Wu, “A decoupling technique for four-element symmetric arrays with reactively loaded dummy elements,” *IEEE Transactions on Antennas and Propagation*, vol. 62, no. 8, pp. 4416–4421, June 2014.
- [13] J. Sarrazin, Y. Mahé, S. Avrillon, and S. Toutain, “A new multimode antenna for mimo systems using a mode frequency convergence concept,” *IEEE Transactions on Antennas and Propagation*, vol. 59, no. 12, pp. 4481–4489, Aug. 2011.
- [14] A. Araghi and G. Dadashzadeh, “Oriented design of an antenna for mimo applications using theory of characteristic modes,” *IEEE Antennas and Wireless Propagation Letters*, vol. 11, pp. 1040–1043, Aug. 2012.
- [15] R. Harrington and J. Mautz, “Theory of characteristic modes for conducting bodies,” *IEEE Transactions on Antennas and Propagation*, vol. 19, no. 5, pp. 622–628, Sep. 1971.
- [16] R. Harrington, J. Mautz, and Y. Chang, “Characteristic modes for dielectric and magnetic bodies,” *IEEE Transactions on Antennas and Propagation*, vol. 20, no. 2, pp. 194–198, Mar. 1972.
- [17] D. Manteuffel and R. Martens, “Compact multimode multielement antenna for indoor uwb massive mimo,” *IEEE Transactions on Antennas and Propagation*, vol. 64, no. 7, pp. 2689–2697, Mar. 2016.
- [18] D. Yang, H. Zeng, R. Chen, J. Qu, Y. Wen, and S. Liu, “Four port compact multimode patch antenna system for vehicular application,” in *2016 IEEE International Workshop on Electromagnetics: Applications and Student Innovation Competition (iWEM)*, pp. 1–3.
- [19] Z. Miers and B. K. Lau, “Design of multimode multiband antennas for mimo terminals using characteristic mode analysis,” in *2014 IEEE Antennas and Propagation Society International Symposium (APSURSI)*, pp. 1429–1430.

- 
- [20] M. Bouezzeddine and W. L. Schroeder, “Design of a wideband, tunable four-port mimo antenna system with high isolation based on the theory of characteristic modes,” *IEEE Transactions on Antennas and Propagation*, vol. 64, no. 7, pp. 2679–2688, Mar. 2016.
- [21] J. Ethier and D. A. McNamara, “Through the looking glass: A characteristic mode view of electromagnetic modeling & design,” in *2010 14th International Symposium on Antenna Technology and Applied Electromagnetics the American Electromagnetics Conference*, pp. 1–4.

# Chapter 2

## Background

### 2.1 Theory of Characteristic Mode

The theory of characteristic mode was firstly presented by Garbacz and Turpin in 1971 [1]. It is then refined and analysed with comprehensive depiction by Harrington et al. with linear operator [2], [3]. For a conducting (or complex) body with incident electromagnetic wave on its surface, the scattering field and surface current can be decomposed into a series of characteristic modes (CMs) [2], [3].

$$\mathbf{J} = \sum_{n=1}^{\infty} \frac{V_n^i \mathbf{J}_n}{1 + j\omega_n} \quad (2.1)$$

where the  $\omega_n$ ,  $V_n^i$  and  $J_n$  are the eigenvalue, modal excitation coefficients and modal current for the  $n^{th}$  mode.

Each CM is accompanied with a corresponding eigenvalue, which represents its radiation ability or energy allocation varied with frequency. Based on designer's specific design targets, these CMs distribution and eigenvalue can be used to iden-

tify and choose CMs that should be working (excited) and ones that should not (suppressed). These CMs could be excited or suppressed by feeding methods and light physical modification which are intuitive to understand with TCM.

Theoretically, TCM works well on a totally arbitrary object as long as it suits for the method of moment (MOM).

### 2.1.1 Characteristic Mode Basis

When an incident electric field occurs on the surface  $S$  of a conducting body, the following operator equation can be deduced by boundary condition [4]

$$[L(\mathbf{J}) - \mathbf{E}^i]_{tan} = 0 \quad (2.2)$$

Here  $\mathbf{E}^i$  is the incident electric field on the conductor surface and the operator  $L$  is defined as, [4]

$$L(\mathbf{J}) = j\omega\mathbf{A}(\mathbf{J}) + \nabla\Phi(\mathbf{J}) \quad (2.3)$$

in which,

$$\mathbf{A}(\mathbf{J}) = \mu \oint\!\!\!\oint_s \mathbf{J}(\mathbf{r}') \frac{\exp(jk|\mathbf{r} - \mathbf{r}'|)}{4\pi|\mathbf{r} - \mathbf{r}'|} d\mathbf{j} \quad (2.4)$$

$$\Phi(\mathbf{J}) = \frac{j}{n\varepsilon} \oint\!\!\!\oint_s \nabla' \cdot \mathbf{J}(\mathbf{r}') \frac{\exp(jk|\mathbf{r} - \mathbf{r}'|)}{4\pi|\mathbf{r} - \mathbf{r}'|} d\mathbf{j} \quad (2.5)$$

where  $\epsilon, \mu, k$  are permittivity, permeability and wave number, respectively. Operator  $\nabla'$  denotes divergence with respect to  $r'$ .

The operator  $L$  allows to relate externally impressed electric field to unknown current density on the object surface. When considering antenna problem, the incident  $\mathbf{E}^i$  is the excitation source on the antenna. This formula decides the surface current distribution.

Symmetrical operator  $Z$  is introduced and the equation (2.3) is rewritten as:

$$Z(\mathbf{J}) = [L(\mathbf{J})]_{\text{tan}} \quad (2.6)$$

Define the real and imaginary part of  $Z$  as

$$R = \frac{1}{2}(Z + Z^*) \quad (2.7)$$

$$X = \frac{1}{2j}(Z - Z^*) \quad (2.8)$$

Considering the general eigenvalue problem on  $Z$ ,

$$Z(\mathbf{J}_n) = v_n M(\mathbf{J}_n) \quad (2.9)$$

where  $v_n$  is eigenvalue,  $\mathbf{J}_n$  is eigenvector and  $M$  is the weighted operator to be choose.

To diagonalize  $Z$ , real part  $R$  of  $Z$  is then chosen:

$$Z(\mathbf{J}_n) = (R + jX)(\mathbf{J}_n) = v_n R(\mathbf{J}_n) \quad (2.10)$$

making the substitution  $v_n = 1 + j\omega_n$  and yet,

$$X(\mathbf{J}_n) = \omega_n R(\mathbf{J}_n) \quad (2.11)$$

The operator  $R$  and  $X$  are both symmetrical operator, so all eigenvalue and eigenvector are real theoretically.

When  $\mathbf{J}_n$  is chosen as the base and weight function in MOM algorithm, it can diagonalize the impedance matrix  $Z$ , and the resulting current  $\mathbf{J}$  can be written

as:

$$\mathbf{J} = \sum_n \alpha_n \mathbf{J}_n \quad (2.12)$$

substitute (2.12) to (2.2) and get,

$$\mathbf{J} = \sum_n \frac{V_n^i \mathbf{J}_n}{(1 + j\omega_n)}. \quad (2.13)$$

Here the  $V_n^i$  is called the modal excitation coefficient and is calculated from the inner product:

$$V_n^i = \langle \mathbf{J}_n, \mathbf{E}^i \rangle = \oint \mathbf{J}_n \cdot \mathbf{E}^i ds. \quad (2.14)$$

(2.13) is the basis for the usage of characteristic mode theory, which tells the fact that the complex yet mystery distribution of antenna surface can be decomposed into a sum of linear CMs.

### 2.1.2 Significance of Eigenvalue

Based on the orthogonality between modal current, the following equation can be obtained, [2]

$$P(J_m, J_n) = (1 + j\omega_n) \delta_{mn} \quad (2.15)$$

when  $m = n$ ,  $P(J_m, J_n)$  is the Poynting vector radiated from  $N^{th}$  mode. It is obvious that eigenvalue  $\omega_n$  directly indicates the amount of energy stored by corresponding mode. If  $\omega_n = 0$ , there is no energy stored,  $N^{th}$  mode radiates the maximum energy, while when  $\omega_n > 0$ , this mode stores magnetic energy and when  $\omega_n < 0$ , electric energy is stored. This equation also indicates that the bigger  $\omega_n$  is, the bigger reactive power is and less ability to radiate power. Normally, for a long thin strip, higher order ( $> 4$ ) eigenvalue is more than 10 bigger than lower

order ones. This is why higher CMs with high eigenvalue are usually omitted.

### 2.1.3 Excitation of Characteristic Mode

The equation for modal excitation coefficient( 2.14) indicates how to excite or depress one specific CM. To illustrate this, rewrite it again,

$$V_n^i = \langle \mathbf{J}_n, \mathbf{E}^i \rangle = \oint \mathbf{J}_n \cdot \mathbf{E}^i ds, \quad (2.16)$$

where  $\mathbf{J}_n$  and  $\mathbf{E}^i$  are the  $n_{th}$  modal current and incident EM on the antenna surface, respectively.

When referring to modal excitation, the incident E-field  $\mathbf{E}^i$  here means external excitation distribution on the whole surface. If  $\mathbf{E}^i$  inserted at feed point(s) makes the inner product  $V_n$  maximum, the  $n^{th}$  mode is excited. As long as its eigenvalue is within the eigenvalue limit for radiation,  $n^{th}$  mode can effectively radiate. On the other hand, if inner product  $V_n$  gets minimum, the corresponding mode is depressed. This means that to excited one mode effectively,  $\mathbf{E}^i$  for feeding needs to be placed on location where the modal current gets maximum with respect to the vicinity current direction.

In many cases, the incident wave is actually a voltage source inserted on the surface mesh of the antenna structure, which can be described as an ideal voltage generator connected across a gap along the antenna [5]. The gap field is usually expressed as a delta source in the simplest ways in MOM and CMA computation as

$$\mathbf{E}^i = V_0 \delta(r') \mathbf{e}, \quad (2.17)$$

where the  $V_0$  is the voltage amplitude,  $\delta(r')$  and  $\mathbf{e}$  are Kronecker delta function

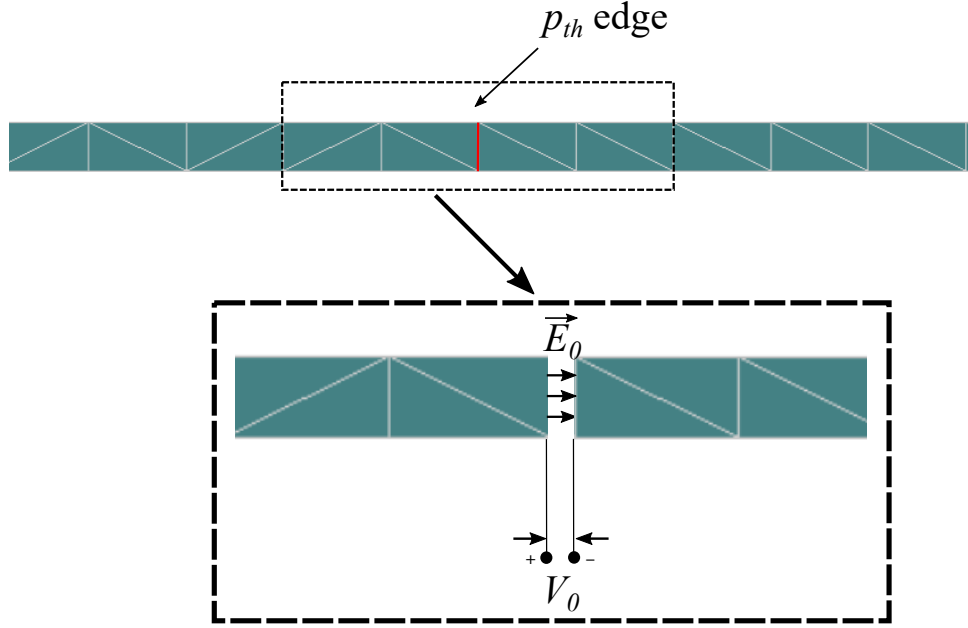


Figure 2.1: Partial view of the feeding on a strip drawn with FEKO.

and the unit vector normal to the feeding surface. As shown in Fig. 2.1, the  $p_{th}$  edge of the total antenna mesh receives a voltage delta source. According to the sifting property of delta function, substitute (2.17) into (2.16) and get

$$V_n^i = V_0 l_p I_n(p), \quad (2.18)$$

where  $l_p$  and  $I_n(p)$  are the triangle length of and the  $n_{th}$  mode's current RWG (Rao-Wilton-Glisson) basis expansion coefficient at  $p_{th}$  mesh edge (the feeding location, or driving edge [5]). Substitute (2.18) into (2.13) and get the simplified excitation formula of characteristic modes

$$\mathbf{J} = \sum_n \frac{V_0 l_p I_n(p) \mathbf{J}_n}{(1 + j\omega_n)}. \quad (2.19)$$



Most of the CMA calculations in previous literature [6–12] are based on (2.19), whenever exterior excitation can be described as a single voltage pulse at the mesh edge of the structure surface.

According to (2.19), there are various ways to excite specific CMs. The most direct way is to put a gap source at the modal current maximum (dipole, bowtie). For patch antenna, the most direct way is directly placing probe at the current maximum. For other planar structure, when the current maximum happens at the edge of a 2-D structure, a slot can be directly inserted at the maximum. The input impedance thus varies with the geometry of the slot. Notably, [13], input impedance for patch is modeled with an equivalent circuit with TCM. This method visualised the input impedance of a probe placed at all possible the geometry of the patch and helped designed for better feeding location.

On the other hand, the feeding structure described by (2.17)–(2.19) is not the only situation when an antenna is excited. If the reciprocity theorem is used, we get the alternative versions of (2.16) [2]

$$\begin{aligned} V_n^i &= \langle \mathbf{E}_n, \mathbf{J}^i \rangle = \iint_s \mathbf{E}_n \cdot \mathbf{J}^i ds, \text{ when being excited by electrical current} \\ V_n^i &= \langle \mathbf{H}_n, \mathbf{M}^i \rangle = \iint_s \mathbf{H}_n \cdot \mathbf{M}^i ds, \text{ when being excited by magnetic current.} \end{aligned} \quad (2.20)$$

(2.20) describes the modal excitation of impressed electrical and magnetic current, respectively. When the excitation composes both  $J^i$  and  $M^i$ , modal excitation is the sum of both formulas in (2.20).

There has been a lot of applications in recent years utilizing a capacitive coupling feeding, e.g., [14–16], and (2.20) finds a way to describe it. In [17], both inductive and capacitive excitation for CMs are introduced. According to the modal exci-

tation theory, inductive coupling element needs to be placed at the edge close to current maximum. If the coupling element is small enough, current in the vicinity caused by this loop would be identical to the modal current. This method is thus called no resonant inductive coupling element (ICE). On the other hand, the capacitive excitation for CMs is to place the coupling element near the modal E-field instead of current maximum. It usually needs to be placed at where the current is weak. The e-field is coupled into the structure. This element is thus called non resonant capacitive coupling element (CCE). For a slot antenna, [6] shows that capacitive feeding can also be used in slot to excite the modal E-field.

## 2.1.4 Q Factor with TCM

### 2.1.4.1 Input Admittance with TCM

From (2.13), the CMs can be considered as a parallel system. The admittance of each CM can be easily derived from (2.13). Suppose that  $E^i$  only happens on one mesh edge of the structure, similar to a delta source. Note it as  $V_a \delta \mathbf{i}$  with amplitude  $V_1$ . The only feed position is noted as  $a$ . Thus the modal excitation coefficient becomes,

$$V_n^i = \langle \mathbf{J}_n, \mathbf{E}^i \rangle = \oint \mathbf{J}_n \cdot \mathbf{E}^i ds = V_a I_n(a) \quad (2.21)$$

$I_n(a)$  is the modal current at feed position  $a$ . substitute it back to (2.13) and yield,

$$\mathbf{J} = \sum_n^N \frac{V_a I_n(a) \mathbf{J}_n(\mathbf{a})}{(1 + j\omega_n)} \quad (2.22)$$

note that for the current amplitude  $I(a)$  at position  $a$  there is  $I(a) = |\mathbf{J}(a)|$ , thus,

$$Y_{aa} = \frac{I_a}{V_a} = \frac{\sum_n \frac{V_a I_n(a) I_n(a)}{(1+j\omega_n)}}{V_a} = \sum_n \frac{J_n(a) I_n(a)}{(1+j\omega_n)} = \sum_n \text{modal self admittance} \quad (2.23)$$

Similarity, mutual admittance between feed portion  $a$  and  $b$  is,

$$Y_{ab} = \sum_n \frac{J_n(a) J_n(b)}{(1+j\omega_n)} = \sum_n \text{modal self admittance} \quad (2.24)$$

#### 2.1.4.2 Q factor calculation

The radiation quality factor  $Q$  is among the most critical and fundamental metrics for antennas, because of its inverse relationship to the antenna bandwidth. The antenna  $Q$  at frequency  $f$  is defined as: [18]

$$Q = \frac{2f \max(W_M, W_E)}{P_A} \quad (2.25)$$

where  $P_A$  is the power accepted by the antenna,  $W_M$  is the stored magnetic energy, and  $W_E$  is the stored electric energy.

Later in [19], the  $Q$  factor was related to the normalized derivative of antenna impedance as, [19]

$$Q_Z \approx \frac{f_o}{2R} \sqrt{\left[ \frac{\partial R^2}{\partial f_0} + \frac{\partial X}{\partial f_0} + \frac{|X|^2}{f_0} \right]} \quad (2.26)$$

with (2.26),  $Q$  factor can be calculated in a characteristic sense. However, due to the derivative in (2.26), these CMs are coupled together and can't be written separably as in (2.12).

On the other hand, with (2.23), the input impedance  $Z_i$  of an antenna dominated with one single CM is,

$$Z_i = R + jX = \frac{1}{Y_i} \approx \frac{1}{Y_1} = \frac{1 + j\omega_1}{I_i^2} = R_1 + jX_1 \quad (2.27)$$

in which  $Y_i$  is the input admittance,  $Y_1$  is the modal admittance for the dominant mode, and  $I_i$  is the current amplitude at port.

By combining (2.26) and (2.27), the Q factor expression for antenna dominated by single CM can be written as: [20]

$$Q = \frac{f}{2} \sqrt{\left(\frac{2I'_i}{I_i}\right) \frac{dI_i}{df}}^2 + \left(\omega'_n - 2\frac{\omega_n I'_{port}}{I_{port}} + \frac{|\omega_n|}{f}\right)^2} \quad (2.28)$$

(2.28) is the modal-expressed Q factor. It can be used to calculate Q factor for a single-CM antenna in CMA discussion. Furthermore, it can also be used to estimate the equivalent sub-circuit of each CM for typical antenna.

When the addressed CM is at its resonance, indicating that  $\omega_1 = 0$ , (2.28) can be simplified to, [20]

$$Q = \frac{\omega}{2} \sqrt{\left(\frac{2I'_{port}}{I_{port}} \frac{dI_i}{df}\right)^2 + \left(\frac{d\omega_1}{df}\right)^2} \quad (2.29)$$

Furthermore, it can still be simplified to an even concise expression when resonating, [20]

$$Q = \frac{\omega}{2} \left| \frac{d\omega_1}{df} \right| \quad (2.30)$$

A number of papers have studied on this. In [21], an approximate calculation for the limit of arbitrary antenna is derived. In [22], a method to minimize Q factor is carried out by introduce a 'tuning mode' for the dominant mode.

In [23], the  $Q_{tot}$  factor is defined as,

$$Q_{tot} = \frac{3}{N^2} \sqrt{\left| MS_n^2 Q_{n,f}^2 - M \sum_{m \neq n}^M MS_m^2 Q_{m,f}^2 \right|} \quad (2.31)$$

where  $N$  is the number of considered CMs.  $M$  is the number of lower CMs that contributing to antenna reactive behavior. And  $MS_n$  is the modal significance for  $n^{th}$  CM,  $Q_n$  is the defined modal  $Q$  factor,

$$MS_n = \frac{1}{1 + j\omega_n} \quad (2.32)$$

$$Q_n = f_{n,res} \frac{\partial \omega}{\partial f} \quad (2.33)$$

the  $f_{n,res}$  denotes the resonate frequency for  $n^{th}$  CM. The formula (2.31) gives clear depiction for the modal behavior, that non-dominant CMs contribute reactive influence onto the total  $Q$ . In [20] and [9], optimization algorithms are used to generate a structure shape with low  $Q$ . With a physical understanding of all the possible resonant modes, appropriate methods can be applied on the antenna structure to enhance its performance. However, TCM did not gain much attention when it was firstly proposed in the early 1971. It was only after the year of 2010 when researchers expanded TCM's widely application and massive potential in antenna design.

### 2.1.5 State-of-art Review on Antenna Research with TCM

In [24], the bandwidth of high frequency electrically small antennas is extended after the feeding platform optimized by TCM. Small loops are added on the surface to excite the CMs of the platform. The impedance bandwidth for each excited CMs on the platform are 0.91%, 1.78%, and 5.12%, respectively. Besides, in [25], TCM based loading method is used to design frequency reconfigurable antenna. With this method, a simple 1.2  $m$  dipole can be tuned from 70 MHz to 300 MHz. In the recent [6], TCM is applied on slotted planar structure and various feed meth-

ods have been discussed. In [26], multiple CMs are excited on a patch through a common feed probe. With optimal feed position, circularly polarized pattern is obtained with better axial ratio (AR) and cross-polarization performance. In [7], an approach to improve the bandwidth of handset antenna is realized when two CMs are merged with single excitation. This is introduced by the metal bezel around the handset chassis. The 6 dB bandwidths for the two ports (monopoles) cover GSM850/900 band and GSM900 band, respectively. A design to get a null-scanning antenna by controlling two CMs is introduced in [27]. An asymmetric and phase-changeable three-port feeding network is used to excite these two CMs. Diodes on the feeding network make it possible to control the phase different between 2 input ports. When the phase difference changes, the total radiation pattern scans up to  $32^\circ$  off broadside direction with a null depth greater than 18 dB. In [28] [29], TCM is used to exploit the design of antenna arrays. In the work, TCM visualizes the current and far-field pattern of an antenna array. The modal information of potential bandwidth is as well provided.

For multiport antennas, coupling is one of the popular topics in TCM applications. In [30], modal admittance is analysed to depict and reduce the out-of-band mutual coupling between two radiation elements. Three examples (dipole, bowtie and monopole on finite ground) verify that the out-of-band influence from other antennas can be reduced by adding lumped loads at positions suggested by TCM. More than 10 dB reduction can be achieved. The paper [31] provides a novel path to get low mutual coupling among antennas on platforms in 2017, with clear physical insight. A formula was given to describe the relationship between the modal excitation coefficients and surface modal charge distribution. Therefore the placements of antennas on the charge-intense areas of platforms were more easily to excite the modes of platforms and vice versa. In [32], TCM is used to examine the coupling of a multiport antenna in a cavity. To suppress the higher order

mode, a metallic block is placed into the cavity so that the coupling is reduced. Recently, [33] introduces an in-band decoupling technique for base station antennas. TCM is used to analyse the coupling among elements in an array. As a result, a metal ring is added to enhance the isolation.

Generally, in mostly research, at the start stage of CMA, a simple structure (e.g. patch, dipole or chassis in handset usage) is firstly analysed by TCM considering the calculating limit of the method of moment(MOM). After having examined the extracted CMs, researchers can make modifications (e.g. current path cut, reactive loading) on the structure to suppress or isolate single CM. After that, they can also utilize various feeding methods to excite single or multiple CM. Sometimes an optimization algorithm can involve in, as in [20] and [9], where both use modal Q factor as objective function to optimize antenna structure. Sometimes, the studied structure can be a three-dimension structure as in [24] and [10]. However, there is little research to study TCM from a relatively complex structure. This is mainly because that the limit of numerical calculation. When there are too many discontinuous parts on the structure, it would be so hard to track CMs in an even narrow band.

## 2.2 Multiport Antenna for MIMO System

### 2.2.1 MIMO System

The MIMO system is obviously one of the most popular applications of multiport antenna. The use of MIMO has emerged as an efficient strategy to increase the

reliability and capacity of wireless systems (e.g. mobile terminals or W-LAN system), while no need for additional power or bandwidth. MIMO has already been introduced in common wireless standards such as IEEE 802.11ac, Worldwide Interoperability for Microwave Access (WiMAX) and Long-Term Evolution (LTE) [34]. The high capacity of MIMO is certificated by its low mutual coupling between antenna elements. To realize this basic requirement, various methods such as a relatively far distance, buffering walls and compensating elements are deployed between antennas. This usually solves the problem. However, with such methods, the size of resulting antenna system enlarges and makes it difficult to accommodate on small platforms.

From (2.2), it is obvious that if the radiation patterns from different antennas in a MIMO system are orthogonal to each other, the system would have an ideal performance. So there is no surprise that TCM is introduced into MIMO antenna design. With the benefit to design a multimode antenna, TCM has the potential to make MIMO antenna smaller with lower coupling between ports at the same time. In addition, as multimode antennas always have a single radiating element. The total structure is then less complex and easier to be fabricated and mounted on terminals.

### **2.2.2 State-of-art Review on MIMO Antenna Research with TCM**

Research and development on the design of multiport antennas with TCM has become increasingly popular in recent days. Multiport antennas designed with TCM are considered ideal candidates for MIMO applications. These antennas are capable of radiating multiple radiation modes through various input ports on



the same antenna structure [35]. The multiport antenna would directly decrease antenna size since it needs only one antenna element. It avoids the spatial requirements of a conventional MIMO array. [36] and [37], the idea of using TCM to design multiport antenna with multiple modes by directly placing feed on antenna is introduced. Since then, MIMO antenna has become an important application for TCM.

As the chassis of a handset device usually makes up most of the radiation at low frequency, how small antenna can efficiently excite modes of chassis leads a multiport antenna problem. In [38], the CMs on a rectangle-shape chassis has been carefully analysed and discussed. Modifications on the platform plate including adding coupling strips and introducing distribution inductor on chassis has been used to get a better impedance matching and bandwidth. To excite the Blended monopoles and planar inverted-F antennas (PIFAs) are placed at the optimized location indicated by TCM to excite specific CMs, as is shown in Fig. 2.2. Similar works has been done in [39], [7], [40], and [41]. In [42], the chassis is slotted and defected according to modal significance to increase the band width of PIFA.

The radiation element for multiport antenna is not restricted to 2-D plate. In [10], a 4-mode MIMO antenna with six ports is realized on the a femto-cell factor structure. A  $220 \times 220 \times 140 \text{ mm}^3$  box is analysed with TCM. Four modes are excited and fed through an internal tunable matching network. This multiport antenna covers the frequency range from 470 MHz to 790 MHz. In 2021, a four-port wide-band cavity-backed antenna with isolating X-shaped block is proposed [32]. TCM is used to analyse the coupling and identify the responsible CMs. An X-shape isolating block is placed in the center of the cavity to increase the isolation.

Besides introducing the interesting inductive and capacitive feeding for TCM

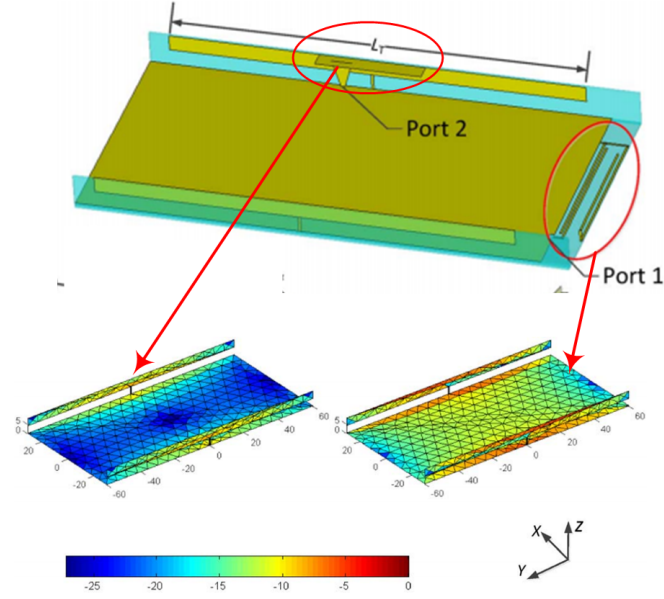


Figure 2.2: A handset chassis with two CMs separately excited by 2 ports. Port 1 is excited by a folded monopole and port 2 is excited by a T-shape strip with the source between its pin and chassis

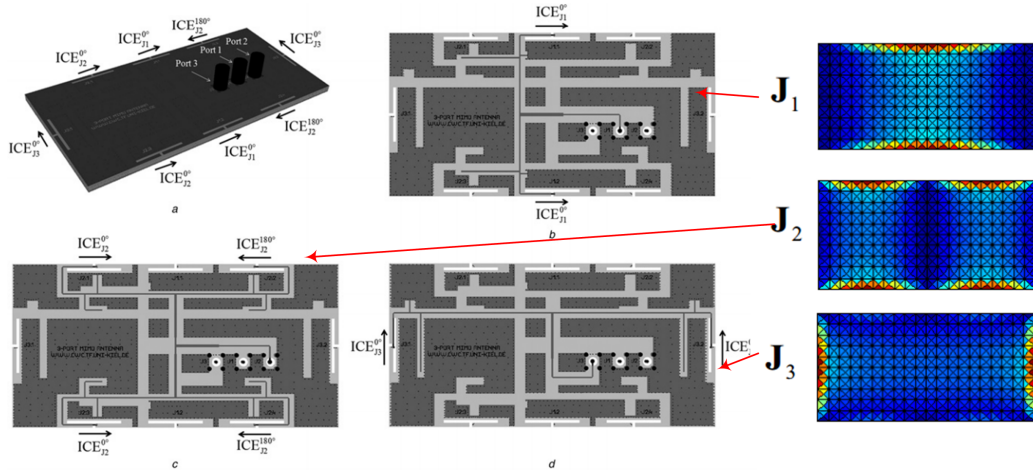


Figure 2.3: A seven-layer structure, three CMs of which are excited through 3 sets of stripline feeding network. The whole feeding network is inside the rectangle box

in [17], R. Martens and D. Manteuffel proposed a three-port antenna system for MIMO usage in [43]. With three sets of compact stripline feeding networks in the center of a seven-layer rectangle plate, three CMs of the box shell are excited with

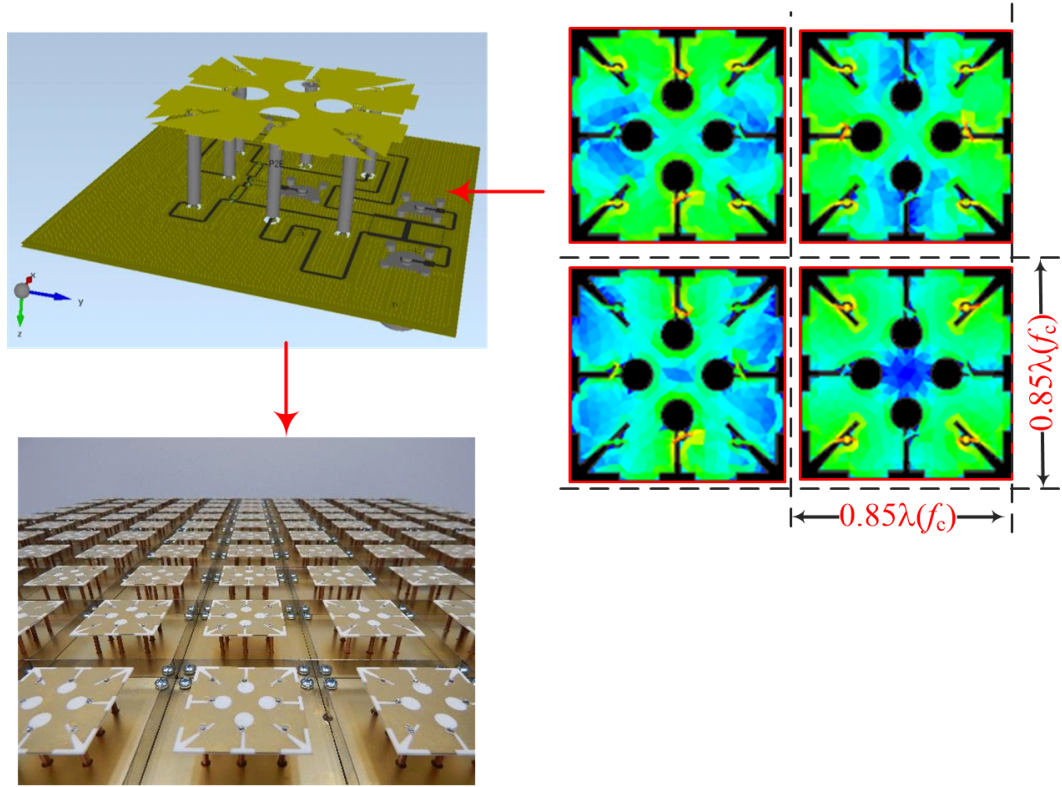


Figure 2.4: The massive MIMO antenna. Four CMs are excited through a multiport antenna. The antenna is fed by a feeding network at its bottom. A massive MIMO array with  $11 \times 11$  is formed with the element

high isolation as in Fig. 2.3. Moreover, in 2016, a compact multimode antenna with four ports is presented in [11], for massive MIMO usage, as in Fig. 2.4. By inserting symmetry slots on a square plate, a feeding network is used to feed them simultaneously. 4 CMs are excited and tuned to the best impedance. The resulting 4 port MIMO antenna is used to fabricate into a  $11 \times 11$  array that has 484 antenna ports. In 2022, an updated version of [11] is presented [44]. A six-port antenna is proposed in this work, with sufficiently decoupled ports over the operating frequency range. All ports on the proposed antenna works at a common band of around 6.25 GHz to 8 GHz. The relative bandwidth is 24.5% and much lower than that in [11], which is limited by the additional port number.

Dealing with multiport antenna indicates that besides maintaining high isolation among ports, all ports need to be well-matched. This brings challenge. To overcome this, some authors use optimization algorithms to design multimode antenna with TCM. In [12], TCM was used to calculate the reactive loading on multiport antenna. A differential evolution algorithm combining TCM optimized antenna structure for a better matching on GSM 900 band while keeping isolation among ports. In [9], genetic algorithm was used for the evolution of antenna structure and yielded a optimized low-Q structure with two ports. Due to the complexity of CM's superposition on Q factor, the author tried to use algorithm to get two-port structure with pure CMs to be excited. Although this paper was more like a theoretical verification than a practical application, it still proved to be a new TCM method for multimode antenna design. There were also other realizations for the optimization TCM antenna design, e.g., [45], an early combination of TCM and multimode antenna. When TCM is used to optimize antennas, goal functions based on modal parameters are calculated firstly, for a smaller Q factor, higher MEC or less reflection. Optimization algorithms are then utilized, to generate a fine structural mesh.

For multiport antennas realized by TCM, which are most likely to be used in massive MIMO for compact structures, previous research usually focus on mobile terminals [7, 38–41]. Other research that focuses on broadening the bandwidth of planar structures [20, 22, 24], is possible to be used on massive MIMO.

The majority of multiport antenna designs face challenges in terms of coupling and impedance bandwidth. In addition to these, another crucial aspect is the method of exciting intended CMs. When the number of ports exceeds two, both bandwidth and isolation of the antenna are at a greater risk.

## 2.3 Dual-polarized Base Station Antenna

### 2.3.1 Base Station Antenna

Along with the extensive increase of global mobile data traffic and developing of modern communication techniques, there has been a rising requirement for base station antenna design. To cover a wide bandwidth and support multiple systems (2G/3G/LTE) and standards, the research on base station now focuses on producing adequate yet stable performances in those bands. Dual polarization technique is also playing an essential role in today's base station applications. A typical  $\pm 45^\circ$  dual-polarized base station utilizes the incoherence of orthogonal electromagnetic waves and multi-path effect in wireless channel and achieves higher system capacity.

The two most common types of base station antennas are patch and dipole antennas. The patch antenna is well-known for its low-profile, light weight, and easy fabrication. However, it has an obvious shortcoming: the achieved impedance bandwidth is naturally narrow. The methods commonly employed to extend the bandwidth often result in high complexity or reduced efficiency.

The other popular yet classic type is dipole antenna. A lot of dipole variations have been proposed to meet the higher and higher requirements. In [46], a dual-polarized base station unit with a crossed dipole operated at  $1.71 \sim 2.69$  GHz. A square loop and a square plate were used as the parasitic radiator and the director, respectively. In 2018, a folded dipole antenna [47] excited by a pair of L-shape crossed balun was proposed. Two pairs of current path on the folded arms were set to increase the stability of HPBW in a range of  $66.5^\circ \pm 5.5^\circ$  at  $1.69 \sim 2.71$  GHz. In [48], a broadband dual-polarized antenna working at  $1.7 \sim 2.7$  GHz was introduced and enhanced. A couple of parasite components were added near the

antenna to improve the HPBW at high frequency.

Although there has been a great number achievements in both theory and application of dual-polarized base station antennas, the related research still remains popular nowadays. The main challenges of dual-polarized antenna design focuses on the followings [49],

- The impedance bandwidth should cover a wide band with low VSWR ( $< 1.5$  usually) at whole operating frequencies. An appropriate wide band impedance matching reduces the pressure caused by reflected waves on the power amplifier.
- Maintain the high isolation ( $S_{21} < -35$  dB usually) between two ports at the wide operating band.
- The antenna should achieve stable radiations at working band. Normally the horizontal HPBW varies in the vicinity of  $65^\circ$  in urban area, and keeps stable at all operating frequencies.

### 2.3.2 State-of-art Review BS Antenna Design with TCM

In [33], TCM is used to analyse the couplings between the antenna elements in a BS array and a metal ring is proposed to improve the isolation. In [50], CMs of a double-layer patch structure is analysed. As a result, a dual-polarized broadband antenna for 5G millimeter wave communication is proposed. The relative bandwidth reaches 43%. In [51] and [52], extra CMs are introduced to improve the bandwidth of BS antennas. Compared to previous methods [48], TCM offers a more intuitive analysis process through the visualization of CMs. In [28] [29] [53],

insights from TCM on BS arrays aid in interpreting the radiation and coupling behavior of arrays. Instead of focusing on the CMs of individual antenna units, the array mode is derived to provide a better understanding.

As mentioned before, TCM specialized on designing multiport antenna with high isolation. It naturally suits the design and enhancement of dual-polarized base station antenna to maintain stable performance at a wide band. However, as a typical base station antenna consists of two components, the antenna and ground plane. It is inconvenient to use the original TCM on the resonance and radiation as it treats both components as a whole body. Thus, a more suitable alternative version of TCM will be presented and utilized in the later chapter.

## 2.4 Summary

In this section, the theoretical background is introduced in detail. This provides a reference for future analysis and design utilizing TCM. The excitation of CMs is crucial for the performance of modal radiation, while the analysis of the Q factor determines the bandwidth of the resulting antenna. Additionally, the application of multiport antennas, such as MIMO systems and dual-polarized base stations, is also discussed.

## References

- [1] R. Garbacz and R. Turpin, “A generalized expansion for radiated and scattered fields,” *IEEE Transactions on Antennas and Propagation*, vol. 19, no. 3, pp. 348–358, May 1971.

- [2] R. Harrington and J. Mautz, “Theory of characteristic modes for conducting bodies,” *IEEE Transactions on Antennas and Propagation*, vol. 19, no. 5, pp. 622–628, Sep. 1971.
- [3] R. Harrington, J. Mautz, and Y. Chang, “Characteristic modes for dielectric and magnetic bodies,” *IEEE Transactions on Antennas and Propagation*, vol. 20, no. 2, pp. 194–198, Mar. 1972.
- [4] R. F. Harrington, *Field computation by moment methods*. Wiley-IEEE Press, 1993.
- [5] S. N. Makarov, *Antenna and EM Modeling with MATLAB*. Hoboken, NJ, USA: Wiley-Interscience, 2002.
- [6] E. Antonino-Daviu, M. Cabedo-Fabrés, M. Sonkki, N. M. Mohamed-Hicho, and M. Ferrando-Bataller, “Design guidelines for the excitation of characteristic modes in slotted planar structures,” *IEEE Transactions on Antennas and Propagation*, vol. 64, no. 12, pp. 5020–5029, 2016.
- [7] C. Deng, Z. Feng, and S. V. Hum, “Mimo mobile handset antenna merging characteristic modes for increased bandwidth,” *IEEE Transactions on Antennas and Propagation*, vol. 64, no. 7, pp. 2660–2667, 2016.
- [8] Q. Wu, W. Su, Z. Li, and D. Su, “Reduction in out-of-band antenna coupling using characteristic mode analysis,” *IEEE Transactions on Antennas and Propagation*, vol. 64, no. 7, pp. 2732–2742, 2016.
- [9] B. Yang and J. J. Adams, “Systematic shape optimization of symmetric mimo antennas using characteristic modes,” *IEEE Transactions on Antennas and Propagation*, vol. 64, no. 7, pp. 2668–2678, Aug. 2016.
- [10] M. Bouezzeddine and W. L. Schroeder, “Design of a wideband, tunable four-port mimo antenna system with high isolation based on the theory of characteristic modes,” *IEEE Transactions on Antennas and Propagation*, vol. 64, no. 7, pp. 2679–2688, Mar. 2016.



- [11] D. Manteuffel and R. Martens, “Compact multimode multielement antenna for indoor uwb massive mimo,” *IEEE Transactions on Antennas and Propagation*, vol. 64, no. 7, pp. 2689–2697, Mar. 2016.
- [12] H. Jaafar, S. Collardey, and A. Sharaiha, “Optimized manipulation of the network characteristic modes for wideband small antenna matching,” *IEEE Transactions on Antennas and Propagation*, vol. 65, no. 11, pp. 5757–5767, 2017.
- [13] B. Yang and J. J. Adams, “Computing and visualizing the input parameters of arbitrary planar antennas via eigenfunctions,” *IEEE Transactions on Antennas and Propagation*, vol. 64, no. 7, pp. 2707–2718, 2016.
- [14] F. Zhu, S. Gao, A. T. Ho, R. A. Abd-Alhameed, C. H. See, T. W. Brown, J. Li, G. Wei, and J. Xu, “Ultra-wideband dual-polarized patch antenna with four capacitively coupled feeds,” *IEEE Transactions on antennas and propagation*, vol. 62, no. 5, pp. 2440–2449, 2014.
- [15] Y. Chen, W. Lin, S. Li, and A. Raza, “A broadband  $\pm 45^\circ$  dual-polarized multidipole antenna fed by capacitive coupling,” *IEEE Transactions on Antennas and Propagation*, vol. 66, no. 5, pp. 2644–2649, 2018.
- [16] Z. Zhou, Z. Wei, Z. Tang, Y. Yin, and J. Ren, “Compact and wideband differentially fed dual-polarized antenna with high common-mode suppression,” *IEEE Access*, vol. 7, pp. 108 818–108 826, 2019.
- [17] R. Martens, E. Safin, and D. Manteuffel, “Inductive and capacitive excitation of the characteristic modes of small terminals,” in *Antennas and Propagation Conference (LAPC), 2011 Loughborough*. IEEE, 2011, pp. 1–4.
- [18] R. F. Harrington, “Effect of antenna size on gain, bandwidth and efficiency,” *Journal of Research of the National Bureau of Standards*, vol. 64, no. 1, 1960.
- [19] A. D. Yaghjian and S. R. Best, “Impedance, bandwidth, and q of antennas,” *IEEE Transactions on Antennas and Propagation*, vol. 53, no. 4, pp. 1298–

- 1324, 2005.
- [20] J. L. Ethier and D. A. McNamara, “Antenna shape synthesis without prior specification of the feedpoint locations,” *IEEE Transactions on Antennas and Propagation*, vol. 62, no. 10, pp. 4919–4934, July 2014.
  - [21] J. Chalas, K. Sertel, and J. L. Volakis, “Computation of the  $q$  limits for arbitrary-shaped antennas using characteristic modes,” in *Antennas and Propagation (APSURSI), 2011 IEEE International Symposium on*. IEEE, 2011, pp. 772–774.
  - [22] M. Capek and L. Jelinek, “Optimal composition of modal currents for minimal quality factor  $q$ ,” *IEEE Transactions on Antennas and Propagation*, vol. 64, no. 12, pp. 5230–5242, 2016.
  - [23] M. H. Rabah, D. Seetharamdoo, and M. Berbineau, “Analysis of miniature metamaterial and magnetodielectric arbitrary-shaped patch antennas using characteristic modes: Evaluation of the  $q$  factor,” *IEEE Transactions on Antennas and Propagation*, vol. 64, no. 7, pp. 2719–2731, May 2016.
  - [24] T.-Y. Shih and N. Behdad, “Bandwidth enhancement of platform-mounted hf antennas using the characteristic mode theory,” *IEEE Transactions on Antennas and Propagation*, vol. 64, no. 7, pp. 2648–2659, 2016.
  - [25] K. A. Obeidat, B. D. Raines, R. G. Rojas, and B. T. Strojny, “Design of frequency reconfigurable antennas using the theory of network characteristic modes,” *IEEE Transactions on Antennas and Propagation*, vol. 58, no. 10, pp. 3106–3113, 2010.
  - [26] Y. Chen and C.-F. Wang, “Characteristic-mode-based improvement of circularly polarized u-slot and e-shaped patch antennas,” *IEEE Antennas and Wireless Propagation Letters*, vol. 11, pp. 1474–1477, 2012.
  - [27] F. A. Dicandia, S. Genovesi, and A. Monorchio, “Null-steering antenna design using phase-shifted characteristic modes,” *IEEE Transactions on Antennas*

- and Propagation*, vol. 64, no. 7, pp. 2698–2706, 2016.
- [28] P. K. Gentner, “On the use of characteristic mode analysis for the design of antenna arrays,” in *2020 14th European Conference on Antennas and Propagation (EuCAP)*, 2020, pp. 1–5.
- [29] Y. Chen, W. Wang, S. Lian, S. Lou, H. Bao, L. Song, and G. Leng, “Far field pattern calculation for antenna array with displacement and rotation of elements using characteristic mode analysis,” in *2022 IEEE International Symposium on Antennas and Propagation and USNC-URSI Radio Science Meeting (AP-S/URSI)*, 2022, pp. 2072–2073.
- [30] Q. Wu, W. Su, Z. Li, and D. Su, “Reduction in out-of-band antenna coupling using characteristic mode analysis,” *IEEE Transactions on Antennas and Propagation*, vol. 64, no. 7, pp. 2732–2742, July 2016.
- [31] D. Su, Z. Yang, and Q. Wu, “Characteristic mode assisted placement of antennas for the isolation enhancement,” *IEEE Antennas and Wireless Propagation Letters*, vol. 17, no. 2, pp. 251–254, 2017.
- [32] J. Molins-Benlliure, E. Antonino-Daviu, M. Cabedo-Fabrs, and M. Ferrando-Bataller, “Four-port wide-band cavity-backed antenna with isolating x-shaped block for sub-6 ghz 5g indoor base stations,” *IEEE Access*, vol. 9, pp. 80 535–80 545, 2021.
- [33] D. Zhang, Y. Chen, and S. Yang, “An in-band decoupling technique for base station antennas,” in *2021 IEEE International Workshop on Electromagnetics: Applications and Student Innovation Competition (iWEM)*, vol. volume1, 2021, pp. 1–3.
- [34] E. Dahlman, S. Parkvall, J. Skold, and P. Beming, *3G evolution: HSPA and LTE for mobile broadband*. Academic press, 2010.
- [35] T. Svantesson, “An antenna solution for mimo channels: the multimode antenna,” in *Conference Record of the 34th Asilomar Conference on Signals,*

- Systems and Computers (Cat. No.00CH37154)*, vol. 2, 2000, pp. 1617–1621.
- [36] E. Antonino-Daviu, M. Cabedo-Fabres, M. Gallo, M. Ferrando-Bataller, and M. Bozzetti, “Design of a multimode mimo antenna using characteristic modes,” in *2009 3rd European Conference on Antennas and Propagation*, pp. 1840–1844.
- [37] A. Araghi and G. Dadashzadeh, “Oriented design of an antenna for mimo applications using theory of characteristic modes,” *IEEE Antennas and Wireless Propagation Letters*, vol. 11, pp. 1040–1043, Aug. 2012.
- [38] H. Li, Z. T. Miers, and B. K. Lau, “Design of orthogonal mimo handset antennas based on characteristic mode manipulation at frequency bands below 1 ghz,” *IEEE Transactions on Antennas and Propagation*, vol. 62, no. 5, pp. 2756–2766, 2014.
- [39] M. Stanley, Y. Huang, H. Wang, S. S. Alja’afreh, Q. Xu, and L. Xing, “Lte mimo antenna using unbroken metallic rim and non resonant cce element,” in *Antennas and Propagation (EuCAP), 2016 10th European Conference on*. IEEE, 2016, pp. 1–4.
- [40] I. Szini, A. Tatomirescu, and G. F. Pedersen, “On small terminal mimo antennas, harmonizing characteristic modes with ground plane geometry,” *IEEE Transactions on Antennas and Propagation*, vol. 63, no. 4, pp. 1487–1497, 2015.
- [41] K. K. Kishor and S. V. Hum, “A pattern reconfigurable chassis-mode mimo antenna,” *IEEE Transactions on Antennas and Propagation*, vol. 62, no. 6, pp. 3290–3298, 2014.
- [42] N. L. Bohannon and J. T. Bernhard, “Design guidelines using characteristic mode theory for improving the bandwidth of pifas,” *IEEE Transactions on Antennas and Propagation*, vol. 63, no. 2, pp. 459–465, 2015.
- [43] R. Martens and D. Manteuffel, “Systematic design method of a mobile multi-

- ple antenna system using the theory of characteristic modes,” *IET Microwaves, Antennas Propagation*, vol. 8, no. 12, pp. 887–893, 2014.
- [44] N. Peitzmeier, T. Hahn, and D. Manteuffel, “Systematic design of multimode antennas for mimo applications by leveraging symmetry,” *IEEE Transactions on Antennas and Propagation*, vol. 70, no. 1, pp. 145–155, 2022.
- [45] J. Ethier and D. McNamara, “Multiband antenna synthesis using characteristic mode indicators as an objective function for optimization,” in *2010 IEEE International Conference on Wireless Information Technology and Systems*. IEEE, 2010, pp. 1–4.
- [46] Y. Liu, H. Yi, F.-W. Wang, and S.-X. Gong, “A novel miniaturized broadband dual-polarized dipole antenna for base station,” *IEEE Antennas and Wireless Propagation Letters*, vol. 12, pp. 1335–1338, 2013.
- [47] H. Sun, C. Ding, and Y. J. Guo, “A wideband base station antenna with reduced beam squint,” in *12th European Conference on Antennas and Propagation (EuCAP 2018)*, 2018, pp. 1–5.
- [48] Y. Cui, L. Wu, and R. Li, “Bandwidth enhancement of a broadband dual-polarized antenna for 2g/3g/4g and imt base stations,” *IEEE Transactions on Antennas and Propagation*, vol. 66, no. 12, pp. 7368–7373, 2018.
- [49] N. Alliance, “Recommendation on base station active antenna system standards,” *NGMN Alliance, Frankfurt, Germany, Tech. Rep*, vol. 1, 2020.
- [50] L. Li, Y. He, L. Zhang, W. Li, and C. Song, “A broadband dual-polarized metasurface antenna for 5g mmwave communication using characteristic mode analysis,” in *2023 IEEE International Symposium on Antennas and Propagation and USNC-URSI Radio Science Meeting (USNC-URSI)*, 2023, pp. 641–642.
- [51] Y. H. Zhu and F. H. Lin, “Metasurface loaded dual-mode wideband dipole antenna using characteristic mode analysis,” in *2022 International Applied*

- Computational Electromagnetics Society Symposium (ACES-China)*, 2022, pp. 1–2.
- [52] T. A. Vu, T. T. Do, D. N. Nguyen, V. X. T. Nguyen, T. T. Truong, D. H. T. Hoang, and M. T. Le, “Broadband dual-polarized antenna element for 5g base station using characteristic mode analysis,” in *2021 IEEE International Symposium on Antennas and Propagation and USNC-URSI Radio Science Meeting (APS/URSI)*, 2021, pp. 985–986.
- [53] P. K. Gentner and M. Pietzka, “Base station antenna array design with characteristic mode analysis,” in *2021 15th European Conference on Antennas and Propagation (EuCAP)*, 2021, pp. 1–5.

## Chapter 3

# Characteristic Analysis on Hexagonal Shapes

### 3.1 Introduction

The idea of applying the theory of characteristic mode (TCM) on multiport antenna design has been introduced since 2007 [1–3]. It was further developed [4–16] in recent years for future wireless communication system. Researchers find TCM works well with multiport antenna designs as it provides an unique physical insight to analyse resonances and radiation. According to the modal orthogonality [17, 18], when several characteristic modes (CMs) of one structure are excited through different ports, the far fields radiated by the ports are orthogonal to each other, which thus results in high port-to-port isolation among those ports.

Due to those advantages, TCM-assisted multiport antenna designs have been carried out on Perfect Electric Conductor (PEC) objects of various two-dimensional shapes [4–9, 11–16], from a simple circular ring, to a triangle plate and to a rect-

angular (square) plate. The physical insight and design procedure introduced by TCM greatly benefited previous work on integrating multiple ports on one antenna. By sharing the same radiation structure among different ports, the design becomes compact.

Generally, TCM analysis in previous designs was subjected to two major limitations: the port number and the common bandwidth. The port number represents how many isolated ports are integrated on one radiation element while the common bandwidth indicates the potential capacity of the MIMO system. However, a considerable number of previous designs are set up with only two ports [6, 7, 14, 15] while those with more ports usually have a narrow common bandwidth for assigned ports [5, 8, 12, 13]. The reason for the first limitation is that the number of ports on an antenna could not be more than that of resonating CMs in the operating band, as long as high port-to-port isolation is required. However, in a certain band the amount of resonating CMs varies according to the size and shape of the antenna, which thus restricts the port number. Moreover, the possible correlation of different CMs' surface current [19] may trouble the port location choice and acts as another negative factor for port number. Additionally, the results of characteristic mode tracking studies [20–22] suggest that CMs with different eigenvalues resonate at different frequencies. Antenna ports utilizing those CMs operate at different impedance bands. Hence, it is likely to result in a multiport antenna with a narrow common bandwidth. Additionally, due to the diversity of modal resonances, the larger realized port number, meaning more CMs involve, the narrower the common bandwidth, and vice versa.

To overcome both limitations, in this chapter, TCM is used to examine the multiport potential of several symmetrical shapes. It is noticed that a symmetrical structure with more degenerate CMs is more suitable to construct wide band



multiport antennas with more than two ports. Thus, a hexagonal shape is chosen and used to build a broadband multiport antenna operating at around  $2.2 \sim 3.4$  GHz with a compact size. The design procedure based on TCM and evolution of the antenna design are presented with details.

## 3.2 Degenerate Characteristic Modes on Symmetrical Plates

In microwave waveguide theory, the modes having the same cut-off frequency but different field configurations are called degenerate modes. In TCM, the term 'degenerate modes', is used to describe similar situation. According to [17], eigenvalue  $\omega_n$  is the result of a generalized eigenvalue problem

$$[X][I]_n = \omega_n[R][I]_n, \quad (3.1)$$

where  $[X]$ ,  $[R]$  are the real and imaginary parts of the impedance matrix  $[Z]$ , respectively.  $[I]_n$  is the column matrix of the coefficients of  $n^{th}$  characteristic currents in MOM computation.

In (3.1), CMs corresponding to the same eigenvalue are called degenerate modes. In a degenerate pair, CMs have the same resonant frequency and similar but different current distributions. [23] proves that degenerate CMs form a set of basis functions for one particular representation and that degenerate CM sets are the consequences of the symmetry of a conducting body. Each degenerate CM in the set corresponds to one particular symmetry operation.

Degenerate CMs always have the same eigenvalue and resonate at the same, or

at least very close frequencies. This indicates that when generating two isolated ports, using a degenerate pair instead of two unrelated CMs in the nearby frequency band, could greatly alleviate the adverse effect on common band from the modal resonance diversity. A degenerate pair provides two CMs candidates available for setting up two different ports with nearly identical operating bands, and avoiding tuning two distinct ones. Thus the modal degeneracy introduces extra freedom for constructing a multiport antenna and make it easy to refine the bandwidth while maintaining relatively large port number with a limited antenna size. For instance, the classic dual-polarized antennas widely used in base stations usually utilize its first degenerate CM pair on the two ports, hence there is no need to deal with two different operating bands and other key properties can be focused. For a multiport antenna with more port number, the degenerate pair would still act well to offset the diversity of modal resonances and generate a wide common band.

In an effort to choose a suitable shape to exploit advantages of degenerate sets on multiport antenna design, Fig. 3.1 (a)-(c) and Fig. 3.2 illustrate the calculated eigenvalues and corresponding current distributions of resonating CMs on several typical shapes. For the sake of simplicity, only two-dimensional shapes are discussed here. Most of them were proposed and discussed in previous publications [5–8, 11, 16, 24]. Considering the variations of resonant frequencies among different degenerate pairs, all the edge lengths are tuned so that their first resonances ( $f_1$ ) occur at the same frequency of 3.15 GHz. The upper frequency limit of the comparison is set as twice as the first resonance to cover enough number of CMs candidates for a multiport antenna. The eigenvalues are calculated and tracked in the observing band by in-house code. Current distributions are drawn by FEKO to present a better understanding of the CMs. Besides, it is worth mentioning that the eigenvalue tracking is plotted in decibel scale for a better view of modal resonances as that in [25]. This is because that the eigenvalue at resonant

frequency generated by numerical computations in MATLAB is always a small number extremely close to zero, which thus becomes a sharp negative minimum in logarithmic value. The resonances are thereby highlighted in decibel scale as shown in Fig. 3.1 and Fig. 3.2. This modified presentation makes it easier to distinguish resonances among a large group of eigenvalue curves, as some low-order CMs have consistent low eigenvalues within a wide range of band and are not easy to find their resonant frequencies if plotted linearly.

In Fig. 3.1 and Fig. 3.2, firstly, it is clear that at the first resonance  $f_1 = 3.15$  GHz, the current distributions of resonating CM(s) of all those shapes are very similar to that of a half-wave dipole. Current on those CMs concentrates at and flows along two of the edges, and acts like a two-element dipole array. The corresponding edge lengths are also approximately half wavelength  $\lambda(f_1)$  at the first resonance. Therefore, we can call those CMs 'dipole-like' Modes. For other resonating modes in the observing band, the current concentrate at and flows along the edges as well.

Fig. 3.1 (a) shows that the triangular plate has only one degenerate 'dipole-like' mode pair resonating at 3.15 GHz with overlapping eigenvalue curves and a single CM, Mode 6 at 5.51 GHz in the observing band. It indicates that the port number of possible multiport antenna based on the triangular plate in the discussed band could not be more than three, such as the two-port antenna in [6].

Rectangular plates are usually used for modelling mobile device chassis. In Fig. 3.1 (b), due to the asymmetry, the rectangular plate has no degenerate CM pairs. There are two different 'dipole-like' CMs resonating at 3.15 GHz and 5.8 GHz corresponding to edge lengths, and a separate CM at 4.8 GHz. Hence, the rectangular plate supports three isolated ports at most in the observing band, or four ports if designed at a much higher frequency [3, 5]. However, to build a proper three-port

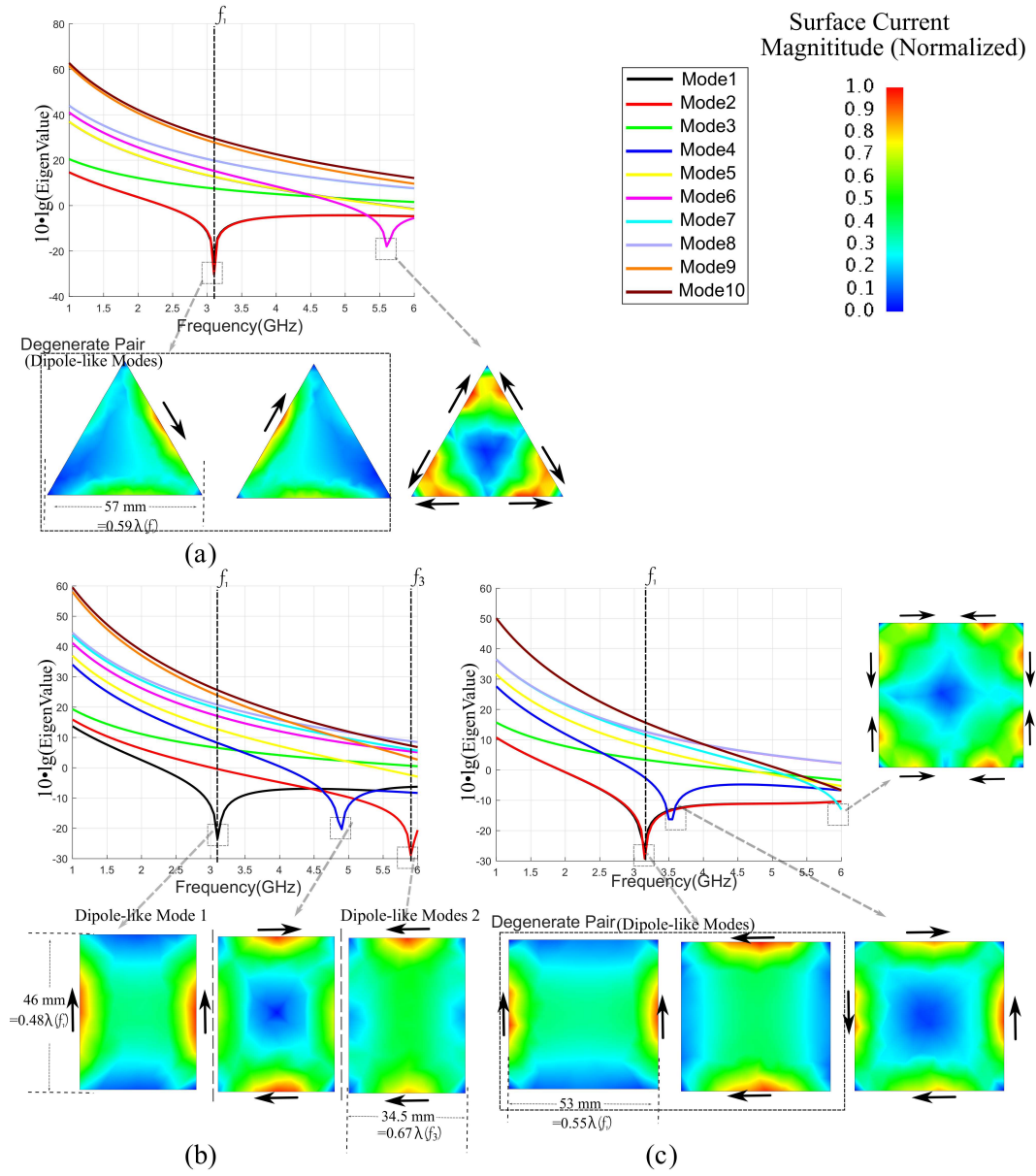


Figure 3.1: Eigenvalue tracked at 1 ~ 6 GHz in decibel scale and modal current distributions at their resonant frequencies of (a) a triangular plate, (b) a rectangular plate, and (c) a square plate. At resonance, eigenvalues that are close to zero turn into sharp minimum.

antenna, the operating band has to raise to around 5 ~ 6 GHz where the three CMs all have small enough eigenvalues to radiate. Additional work has also to be done to tune three separate frequency bands into a common one, which is likely

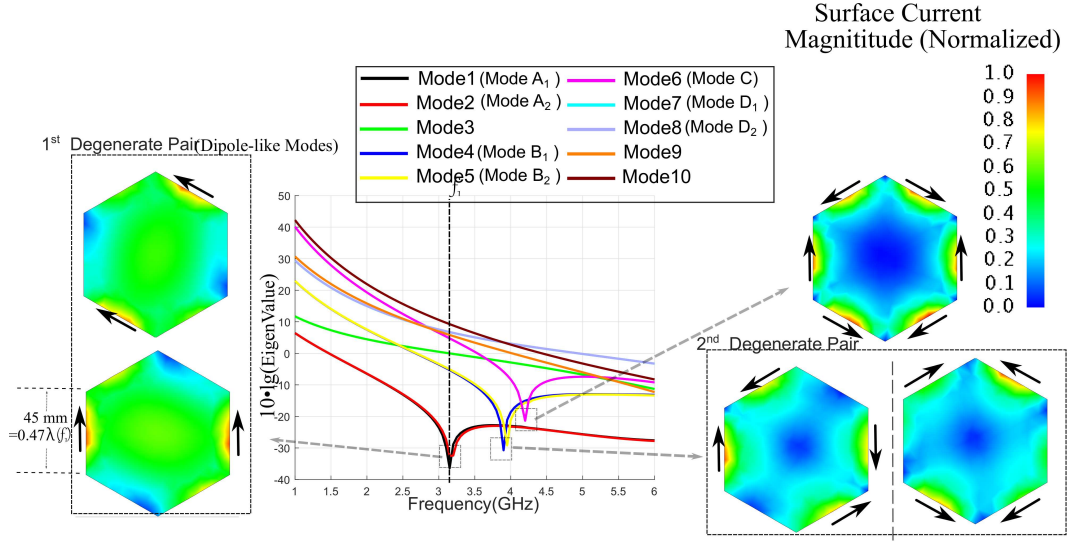


Figure 3.2: Eigenvalue tracking in decibel scale and modal current distributions at their resonant frequencies of a hexagonal plate.

to result in a notably narrow bandwidth, as the three-port antenna in [8, 13]. In fact, most multiport antenna designs based on rectangular plate [7, 14] are built with two ports to concentrate on tuning for a better bandwidth and impedance matching. Other previous examples avoid tuning for a common band and build for multi-band MIMO designs [9, 15], or construct reconfigurable antennas [16]. Compared with the rectangular plate, there are one pair of degenerate 'dipole-like' modes, and two non-degenerate CMs at higher frequencies on a square shape in Fig. 3.1 (c). Therefore, it is enough to construct a compact planar antenna with port number as much as four and desirable common bandwidth as that in [11, 26]. It is also noticed that there is a considerable frequency difference between the fourth resonating CM (around 6 GHz) and others. This difference could deteriorate the final common bandwidth of the four ports and limit the antenna size. [22] suggests that symmetry introduces degeneracy. Given that there is one more symmetry axis on a hexagonal shape than on a square shape, it should have more degenerate CM pairs on the same band. Fig. 3.2 illustrates that on a hexago-

nal plate, there are two degenerate pairs and one separate CM in the observing band. One more degenerate pair indicates two more ready-to-radiate modes to use. Therefore, a hexagonal-shape antenna operating at the same band could support five isolated ports. Besides, the decibel chart also shows clearly that the five resonances are spaced closely in the frequency band in comparison with other listed shapes. Hence, it would take less work to tune each port to maximize the overlapping band. In addition, the operating frequency band do not have to move to a higher frequency to find enough number of available CMs like other shapes, thus utilizing the hexagonal shape could also lead to a compact size antenna.

In summary, TCM has been used to analyse and compare several symmetrical two-dimensional shapes. It is explained in a TCM sense that previous multiport antenna designs based on triangular and asymmetrical rectangular shapes still suffer from the limitations of port number and common bandwidth. Rectangular and hexagonal shapes, on the other hand, have more available CMs for multiport antenna designs. Therefore, a hexagonal plate is chosen in this chapter to build a wide band antenna with a compact size. Two pairs of degenerate modes should not just guarantee four-port setup on the antenna, but also help to realize a wide common bandwidth.

### 3.3 Excitation of Degenerate Modes on Hexagonal Plate

#### 3.3.1 Adding Slots for CM Excitation

In order to excite the CM candidates to construct a multiport antenna, the resonating CMs of the hexagonal plate with their current are looked at again in Fig. 3.2. It shows that the current density of all resonating CMs concentrates at edges. According to [17], the current maxima indicate the feeding location. Thus each CM can be effectively excited by placing voltage sources on corresponding edges.

Following this idea, six straight slots are placed at each edge centre to enable port setup. The slots should also rectify CM currents and concentrate the current at the slot ends. This is done in Fig. 3.3 (a), where the current chart in decibel scale illustrates that at resonant frequencies, the modal current of discussed CMs now flows along both the shape edges and the inserted slots. The current maxima are concentrated at the slot exterior ends. Thus they can be excited effectively by placing external source at the edge centre. Compared with the original hexagon in Fig. 3.2, each CM current of the modified one flows in the same direction on the corresponding edges. The pattern comparison in Fig. 3.4 also verifies that the inserted slots barely affect the modal radiation patterns.

However, if both eigenvalue tracking results in Fig. 3.3 (a) and Fig. 3.2 are studied, it is obviously that first degenerate pair– the 'dipole-like' Modes, though radiate similar far fields after the modification, resonate at a much lower frequency of 2.15 GHz than its original version (3.1 GHz), and so are other modes. In [11],

similar change was observed on the CMs of a square plate and thus the final antenna size was greatly reduced. For the discussed hexagonal plate, firstly, the far field comparison in Fig. 3.4 indicates that the radiation mechanisms of each modified CM do not change. Nevertheless, the current distribution in Fig. 3.3 (a) tells that at the first resonance, due to the added slots, the modified 'dipole-like' modes have current concentrating at and flowing along its two consecutive edges, instead of only one as those in Fig. 3.2. It makes the effective length of the equivalent dipole 78 *mm* rather than the original 45 *mm*. Therefore the shift on modal resonating frequency is a joint result of the resonance of the hexagon edges ( $l_{equivalent} = 78 \text{ mm} = 0.56\lambda(f_1)$ ) and the effect of straight slots ( $l_{slot} = 0.22\lambda(f_1)$ ). It is also noted that blending and extending the interior end of each slot near shape centre could further lower the resonance frequency to a certain extent, but could damage the shape symmetry and deteriorate the isolation among the degenerate pairs.

To give a clear analysis of the following feeding port setup, name the two degenerate CM pairs: Mode 1,2 and 4,5 in Fig. 3.2 and Fig. 3.3 (a) as Mode  $A_1$  and  $A_2$ , Mode  $B_1$  and  $B_2$ . Also the separate Mode 6 is named as Mode  $C$ . The linear representation of corresponding eigenvalues and modal significance are also drawn in Fig. 3.3 (b) and (c) respectively to illustrate more details, in which the modal significance (MS) [27], with corresponding eigenvalue  $\omega_n$ , defined as

$$MS_n = \left| \frac{1}{1 + j\omega_n} \right|, \quad (3.2)$$

represents the intrinsic property of  $n^{th}$  CM independent of any external sources and suggests its bandwidth: CMs with  $MS \geq 1/\sqrt{2}$  are usually referred to as significant modes [27] and are to be considered for excitation.

In Fig. 3.3 (c), MS curves show that the first degenerate pair, Mode  $A_{1,2}$  have a



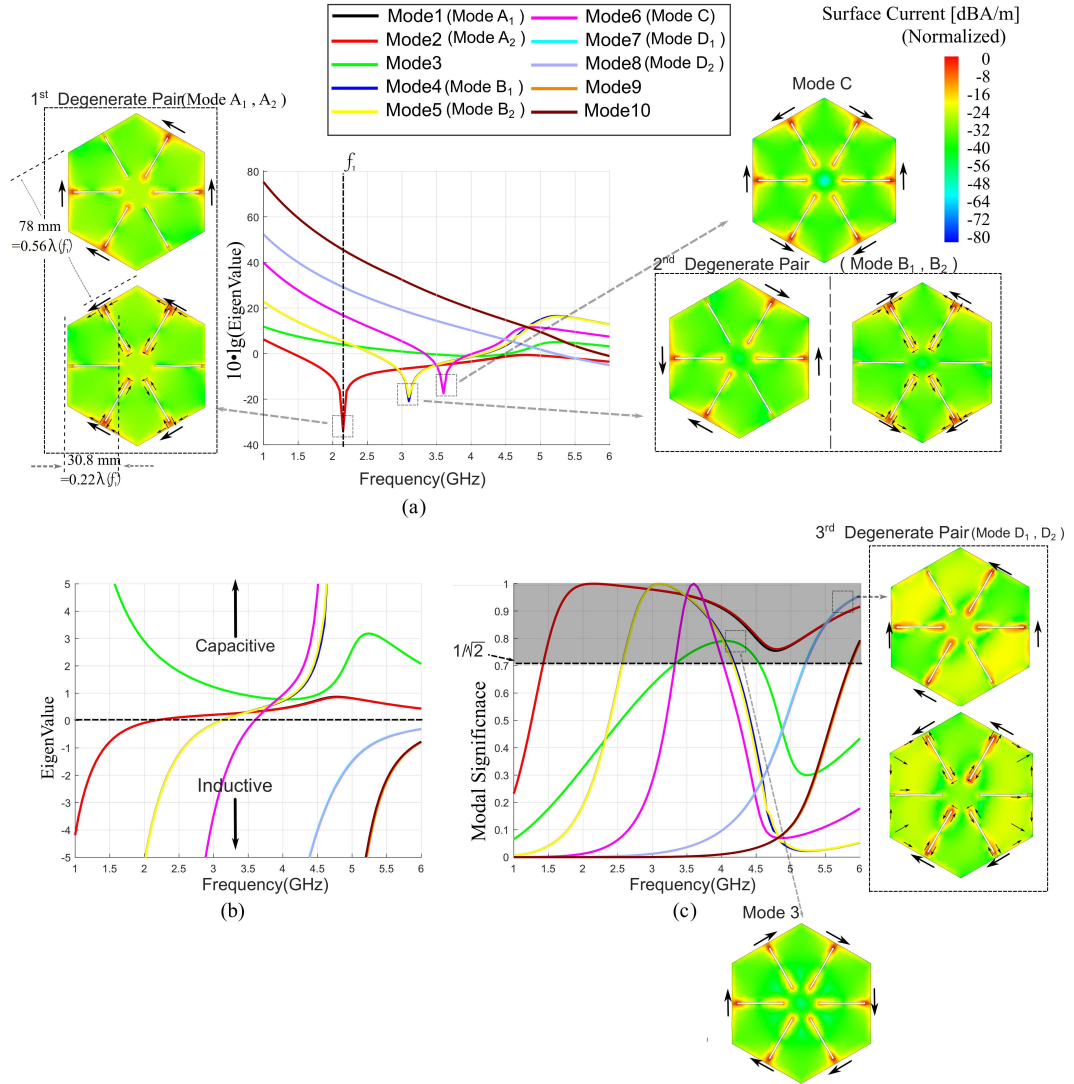


Figure 3.3: (a) Eigenvalue tracking in decibel scale and modal current distributions at their resonant frequencies of the hexagonal plate with inserted slots, (b) eigenvalue tracking in linear representation, (c) MS curves and modal current of Mode 3 and the third degenerate pair.

wide bandwidth starting from 1.5 GHz, while Mode  $B_{1,2}$  are considered significant modes from about 2.6 GHz to 4.2 GHz. Mode C has a narrow bandwidth at relatively higher frequency band. In addition to the five mentioned CMs, Fig. 3.3 (c) also reveals that in the  $MS \geq 1/\sqrt{2}$  area, there are Mode 3 and another two pairs

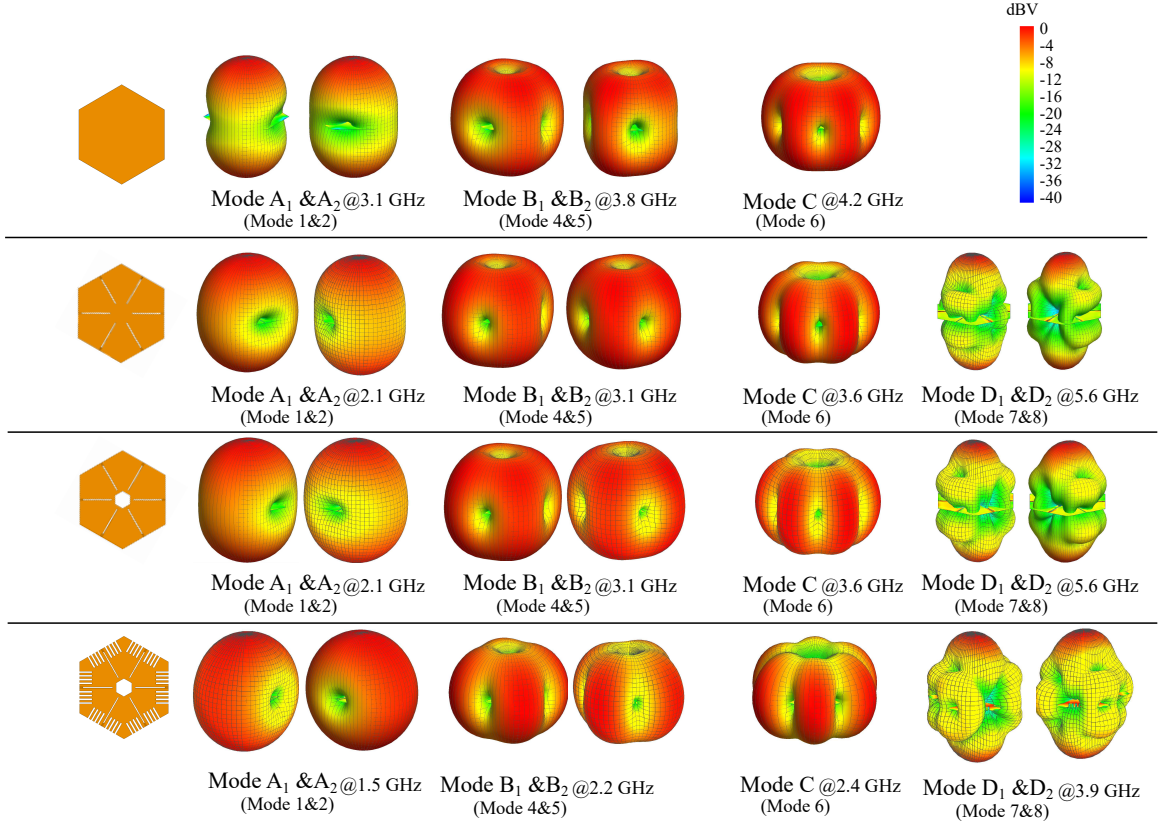


Figure 3.4: The normalized modal radiation patterns of discussed CMs at their resonant frequencies. From top to bottom are the original hexagonal plate, the hexagonal plate with inserted straight slots, the slotted plate with central cut, and the size-reduced slotted plate.

of high-order degenerate modes: Mode 7, 8 and Mode 9, 10 at higher frequency.

Among them, Mode 3 (green curve) does not have a zero eigenvalue and has a narrow bandwidth. In addition, its current distribution in Fig. 3.3 (c) indicates that it needs six sources on all the edges to be excited, thus could hardly function when other discussed CMs are excited by edge ports. Therefore, Mode 3 is ignored in later discussion. The degenerate pair Mode 9, 10 (orange and brown curves) do not enter the  $MS \geq 1/\sqrt{2}$  area until the frequency is higher than 5.7 GHz and are generally less significant than other CMs. Hence, they are also ignored.

Mode 7,8 have significant MS since the frequency increases to 5.2 GHz. Their current distribution in Fig. 3.3 (c) shows that they have identical current direction and maximum at each edge compared with Mode  $A_{1,2}$ . Therefore Mode 7,8 will contribute to the radiation at high frequency as long as Mode  $A_{1,2}$  are excited by edge sources. Another thing to note from the current distribution is that the straight slots involve much more in the resonance of Mode 7,8 than in that of Mode  $A_{1,2}$ , while on Mode 7,8 the current density along edges is weaker than on other CMs. It coincides with the fact that the length of the slots (30.8 mm) is almost half wavelength ( $0.56\lambda(f = 5.2 \text{ GHz})$ ). Slot Mode 7,8 are named as Mode  $D_{1,2}$  for the following discussion.

As discussed above, Mode  $D_{1,2}$  become significant at high frequency in the radiation by ports that excite Mode  $A_{1,2}$ . Thus TCM is used to analyse their mutual contribution under the same feeding configuration. The eigenvalue curves in Fig. 3.3 (b) shows that Mode  $A_{1,2}$  pass the resonance at 2 GHz and stay positive after that. And positive eigenvalues indicate capacitive Mode  $A_{1,2}$  [17]. On the other hand, Mode  $D_{1,2}$  become significant after 5.2 GHz and stay inductive before they resonate at higher frequency. Therefore, it is highly possible that when Mode  $A_1$  ( $A_2$ ) is excited by an external port, there is a resonance at low frequency corresponding with Mode  $A_1$ , and Mode  $D_1$  will only contribute to the radiation when the frequency is higher than about 5 GHz, where the combined excitation of capacitive Mode  $A_1$  and inductive Mode  $D_1$  should create a new resonance.

### 3.3.1.1 Excitation of the Modified CMs

In the previous section, the analysis shows that after inserting the slots, Mode  $A_{1,2}$  and Mode  $B_{1,2}$  still reserve their degenerate properties and a new degenerate

pair Mode  $D_{1,2}$  becomes significant at high frequency. According to [17], to excite those CM pairs, voltage sources should be placed on four of the edges at the modal current maxima. In each degenerate pair, the spatial layouts of feeding edges for two CMs are  $60^\circ$  rotation of each other. Therefore, to ease the feeding network involving, it is natural to let Mode  $A_1$ ,  $B_1$  and  $D_1$  share the same set of feeding ports, while Mode  $A_2$ ,  $B_2$  and  $D_2$  use similar ports set in different angle. In addition, due to the identical current direction at slot ends, the same feeding scheme that excites Mode  $A_{1,2}$  at lower frequency also activates Mode  $D_{1,2}$  at a frequency higher than approximately 5.7 GHz.

As shown in Fig. 3.5, six antenna ports are placed on the hexagonal plate and each CM is assigned with a feed configuration. According to their current distributions, Mode  $A_1$  ( $D_1$ ) and  $B_1$  are excited by the same feeding set of port 1, 2, 4, 5. To feed both CMs simultaneously, there should be in-phase excitation on port 1, 5, and out-of-phase excitation on port 2, 4. This can be easily realized with a  $180^\circ$  hybrid between the external ports and antenna ports. A similar configuration can be applied on Mode  $A_2$  ( $D_2$ ) and  $B_2$  as well. Mode  $C$ , on the other hand, needs to use all the six antenna ports for excitation. Thus, a five-port antenna can be realized by exciting those five CMs through a  $5 \times 6$  feed network theoretically. However, to avoid resulting in a complex feed network, and considering that Mode  $C$ 's narrow bandwidth at high frequency will also hamper the other four CMs from forming a wide common band, in this chapter, only Mode  $A_{1,2}$  ( $D_{1,2}$ ) and Mode  $B_{1,2}$  are chosen and used to design a compact four-port antenna.

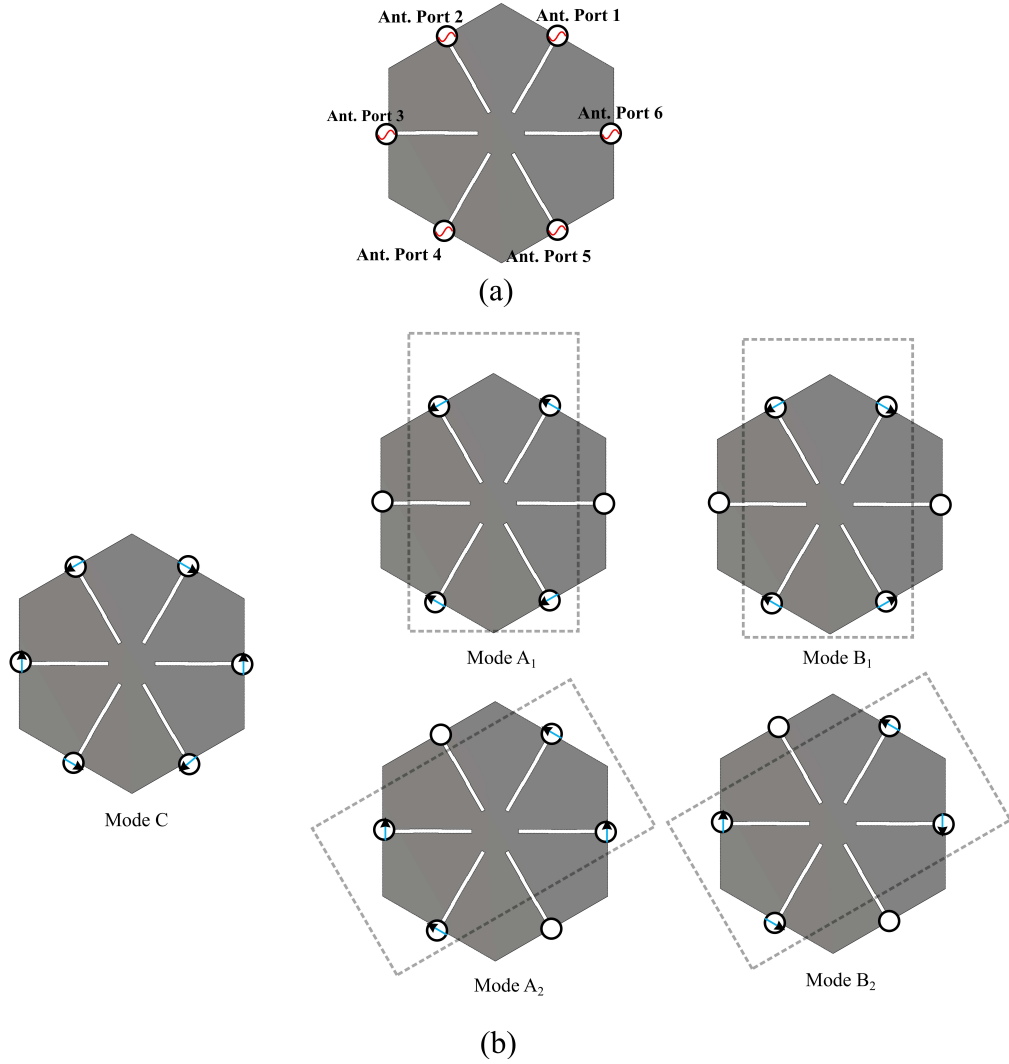


Figure 3.5: (a) Port layout and numbering on the antenna plate, (b) Feed configurations to excite five CMs.

### 3.3.2 Performance of the Hexagonal Antenna

Fig. 3.6 presents the circuit connection in CST's Design Studio, realizing the feed-configurations discussed in previous section. Ideal circuit components  $180^\circ$  hybrid and dividers are used to feed the antenna. The resulting S-parameter is illustrated in Fig. 3.7. It shows that port 3' and 4', exciting the degenerate Mode  $B_1$  and  $B_2$  respectively, have identical self-reflections  $S_{3',3'}$  and  $S_{4',4'}$ . Because of

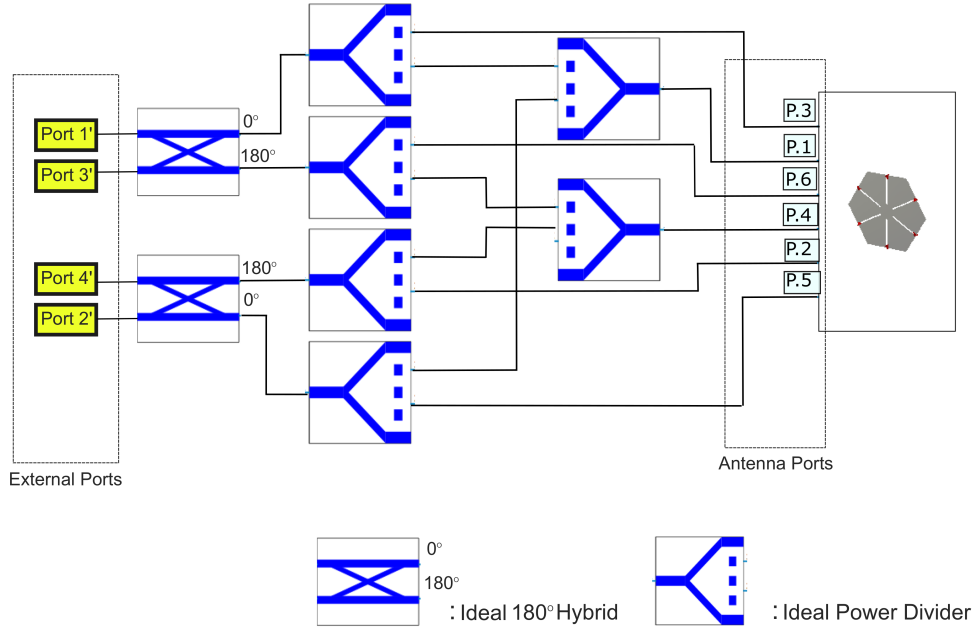


Figure 3.6: The circuit connection to feed the hexagonal antenna in CST's Design Studio.

the modal degeneracy, there is no need to tune port 3' and 4' separately to maximize their overlapping band. Their  $-10$  dB band starts from 2.59 GHz to 4.90 GHz and the coupling  $S_{3',4'}$  is always below  $-20$  dB in the band. It is also notable that  $S_{3',3'}$  and  $S_{4',4'}$  coincide to the Mode  $B_{1,2}$ 's bandwidth in Fig. 3.3 (c).

Similarly, port 1' and 2' excite the degenerate pair Mode  $A_{1,2}$  ( $D_{1,2}$ ), respectively, and have identical  $S_{1',1'}$  and  $S_{2',2'}$  with satisfying 20 dB isolation. It is observed that  $S_{1',1'}$  has two resonances, one occurring at 1.7 GHz and the other at 5.2 GHz. With the reference of Fig. 3.3 (c), it is clear that the first resonance of port 1', 2' corresponds with Mode  $A_{1,2}$ , while the second resonance is a combined result of Mode  $A_{1,2}$  and Mode  $D_{1,2}$ , as discussed in previous section. In general, port 1', 2' have a wide bandwidth inheriting from Mode  $A_{1,2}$  and Mode  $D_{1,2}$  as Fig. 3.3 (c) shows. However, two resonances of  $S_{1',1'}$  are far away in the frequency band, and the impedance matching between two resonances is poor. Thus, the resulting  $-10$  dB band of port 1', 2' is only 3.4 ~ 6.5 GHz.

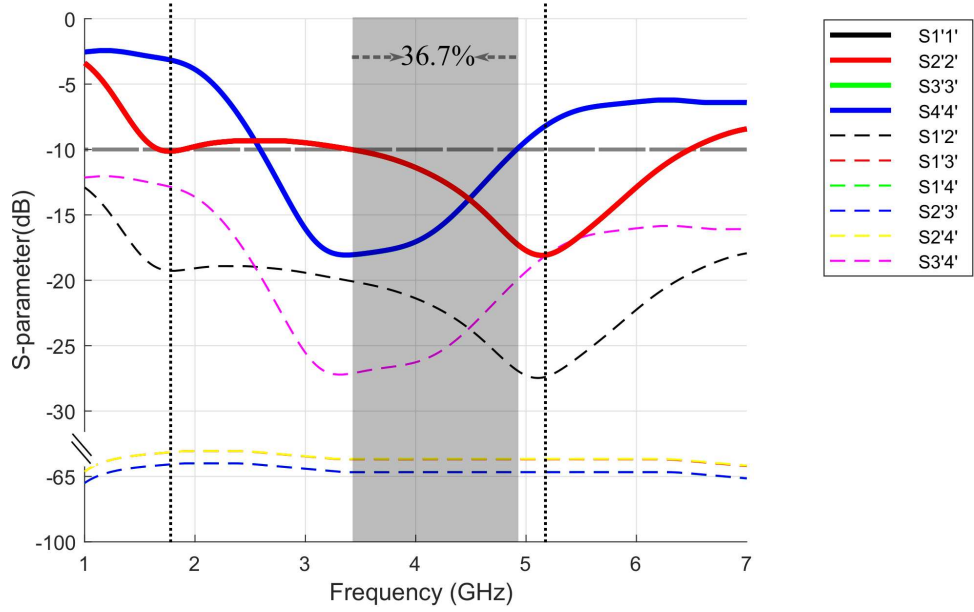


Figure 3.7: Simulated S-parameters of the slotted hexagonal plate in Fig. 3.3. The relative bandwidth of the overlapping band is 36.7%.

The modal degeneracy avoids tuning the common band between  $S_{1',1'}$  and  $S_{2',2'}$ , and that between  $S_{3',3'}$  and  $S_{4',4'}$ . The modal orthogonality also guarantees satisfied isolation among all four ports. However, because of two degenerate pairs' different resonant frequencies, the common band of four ports in Fig. 3.7 reduces to a narrow band from 3.43 GHz to 4.92 GHz. In spite of this, this hexagonal plate with simple slots still meet the expectation at beginning of this chapter, that the hexagonal shape with more resonating degenerate CM pairs would result into a wide band antenna with more than two ports. Compared with the common bandwidth of the triangular plate (11%) in [6], and that of the square plate (34.4%) in [11], the wide relative bandwidth of the hexagonal antenna (36.7%) benefits from modal degeneracy, and could be a good candidates for sub-6 GHz base station antenna.

To take full advantages of the hexagonal shape, next sections will focus on further tuning the different resonances of the hexagonal antenna and realized a wider common bands with a compact size.

### 3.4 Lumped Loading to Tune the Common Band

The narrow common band of the slotted hexagonal antenna is the result of different resonant frequencies of the three degenerate pairs: Mode  $A_{1,2}$ , Mode  $D_{1,2}$  and Mode  $B_{1,2}$ . If any of those modal resonances could be tuned separately without affecting others, the port resonances are possible to be unified at the same frequency and generate a wide common bandwidth with satisfied impedance matching.

Therefore modal current distributions in Fig. 3.3 are studied again. It has been noticed in the last section that the slot CMs,– Mode  $D_{1,2}$  have stronger current flowing along the interior slot ends near the shape centre, compared with the other two CM pairs. To take the advantage of the difference, a small hexagon hole is cut in the center to further localize the current and enable later modification, as shown in Fig. 3.8. The central hole does not cut off the current path, hence the cut hole merely the CMs' resonance behaviours, as can be confirmed by the eigenvalue tracking result in Fig. 3.8 and modal far field comparison in Fig. 3.4.

After the modification, Fig. 3.8 shows that the new Mode  $D_1$  ( $D_2$ )'s current is concentrated and flows around the hole in the centre, in which Mode  $D_1$ 's current flows along the interior ends of slots fed by Antenna port  $\{1, 3, 4, 6\}$ , while Mode  $D_2$  current concentrated at slots fed by Antenna port  $\{1, 2, 4, 5\}$ . Besides, Mode  $D_{1,2}$ 's modal current amplitudes near the central hole are stronger than those of Mode  $A_{1,2}$  and  $B_{1,2}$  in the same area. As [28] suggests that reactive loadings could control the modal resonances, lumped inductors are considered to insert at those locations. They are expected to extend the current path of Mode  $D_{1,2}$  to shift their resonant frequencies while having less effect on Mode  $A_{1,2}$  and  $B_{1,2}$ .

The modal current maxima of Mode  $D_{1,2}$  suggests that inductive loadings at



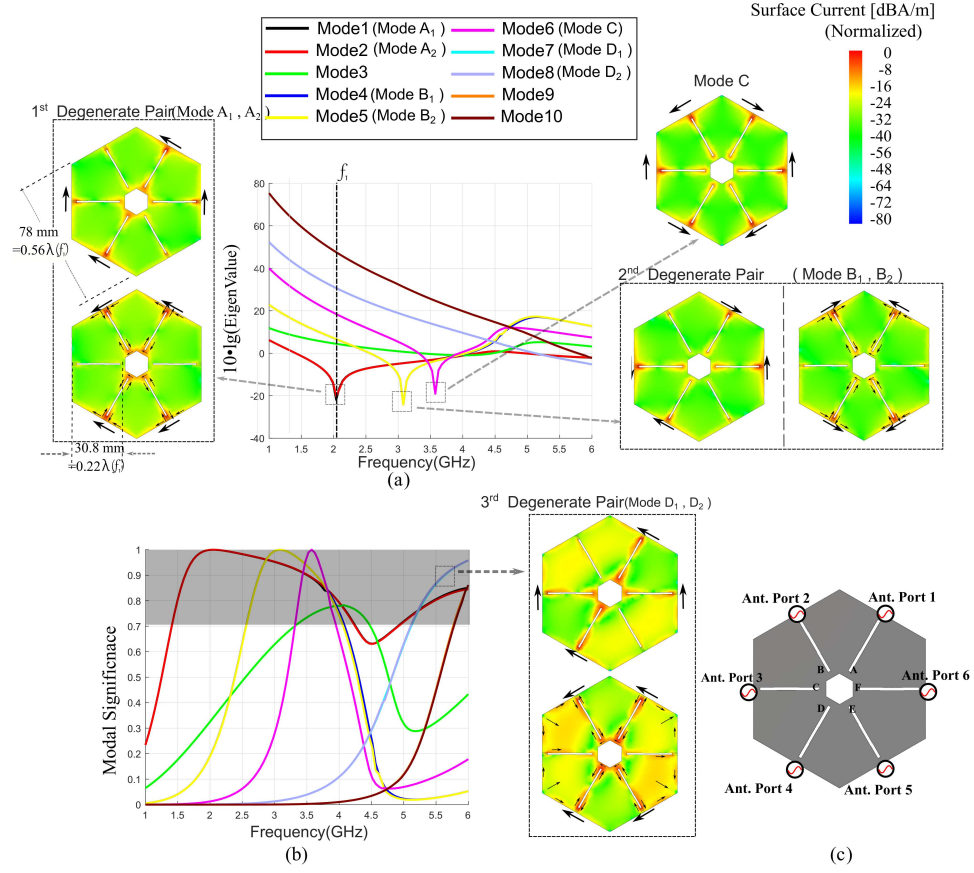


Figure 3.8: (a) Eigenvalue tracking in decibel scale and modal current distributions of the slotted plate with central slot, (b) MS curves and modal current of the third degenerate pair, and (c) the hexagonal plate with edge ports and loading positions  $A \sim F$ .

position  $C, F$  in Fig. 3.8 (c) would tune the resonance of Mode  $D_1$  separately, and inductors at position  $B, E$  tune that of Mode  $D_2$ , while inductive loadings at position  $A, D$  would tune both Mode  $D_{1,2}$ . To avoid destroying the symmetry, Position  $A \sim F$  are all inserted with inductors of the same value, which is presented in Fig. 3.9 (b). The variations of port reflections with inductor value are drawn in Fig. 3.10. In Fig. 3.10, as the inductive loading value increases from 2 nH to 5 nH, the second resonance of  $S_{1',1'}$  shifts to lower frequency, while the first resonance barely move. The result again conforms to the previous modal current analysis, that low-order Mode  $A_{1,2}$  is mainly the resonance of the hexagonal edges rather

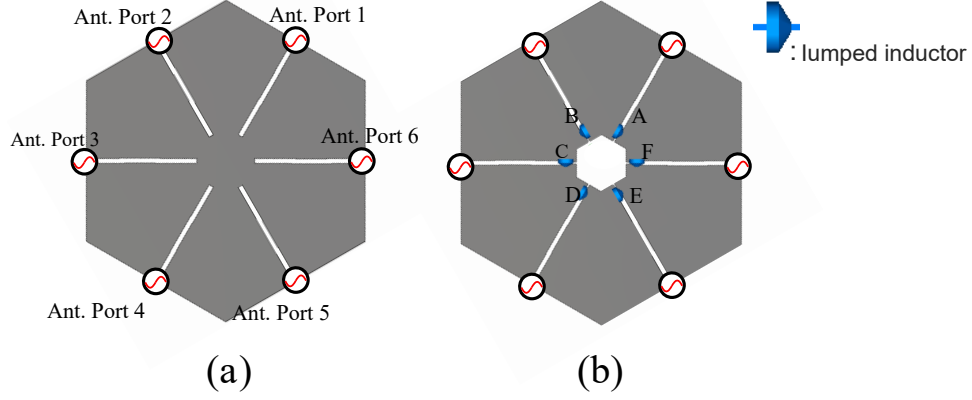


Figure 3.9: Evolution of the hexagonal antenna: (a) the slotted antenna, (b) the slotted antenna with inductive loadings.

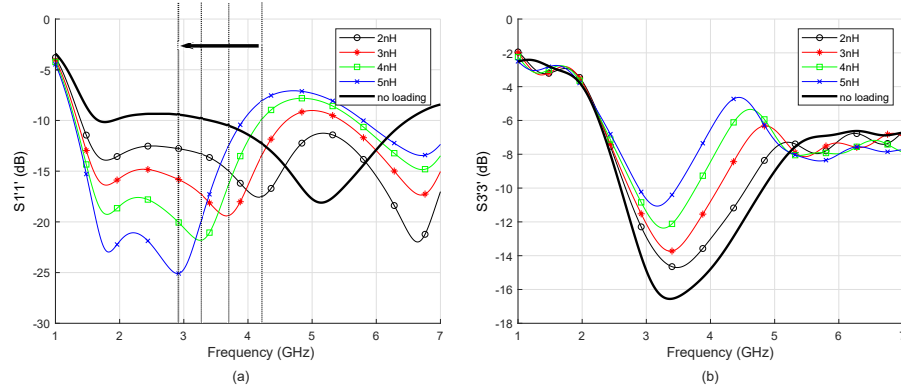


Figure 3.10: The effect of inductive loading value on S-parameter of (a) port 1' and (b) port 3'. It shows that loading controls the second resonance of port 1', while shows lesser influence on port 2'.

than the slots, whereas on high-order Mode  $D_{1,2}$ , slots dominate the resonance. Moreover, the variation of  $S_{3'3'}$  shows that higher value of inductors also leads to poor impedance matching of port 3'. With the consideration of both satisfied impedance matching and wide common bandwidth, the inductor value is tuned to 3.2 nH.

The final S-parameters are drawn in Fig. 3.11. The common band is now from 2.68 GHz to 4.1 GHz (relative bandwidth: 42%), with 20 dB isolation in the

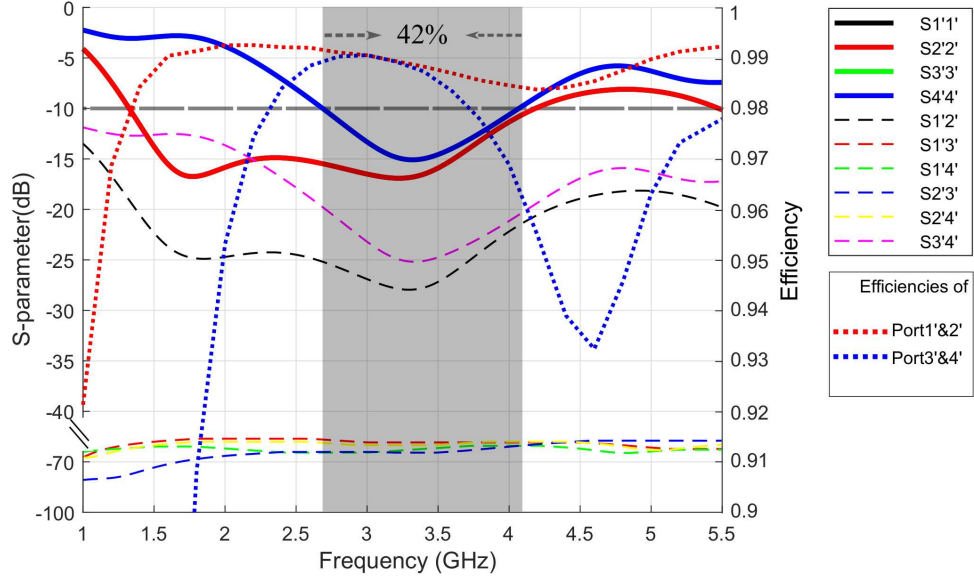


Figure 3.11: Simulated S-parameters and radiation efficiencies of the slotted hexagonal antenna with loading inductors in Fig. 3.9 (b). The relative bandwidth of the overlapping band is 42%. Radiation efficiencies fluctuate within a range of 96% ~ 99% in the common band.

band. The outer dimensions of the hexagonal plate are  $\lambda(f_c) \times 0.88\lambda(f_c)$  at the central frequency  $f_c = 3.40$  GHz. The commercial 0805CS series chip inductor by Coilcraft, Inc. is used to replace the ideal lumped elements. The simulated radiation efficiency of the multiport antenna is also drawn in Fig. 3.11. It is worth mentioning that the simulated efficiency did not include the loss in feeding network, only to verify the loading effect on the antenna. The radiation efficiencies of port  $1' \sim 4'$  in Fig. 3.11 fluctuate within a range of 96% ~ 99% in the operating band.

### 3.5 Size Reduction with Edges Slots

The antenna plate is small enough but there is still room for size reduction. It has been concluded earlier that the edges involve in the resonances of Mode  $A_{1,2}$ ,  $B_{1,2}$  and  $D_{1,2}$ . With the intention of decreasing the antenna size, inductive slots are

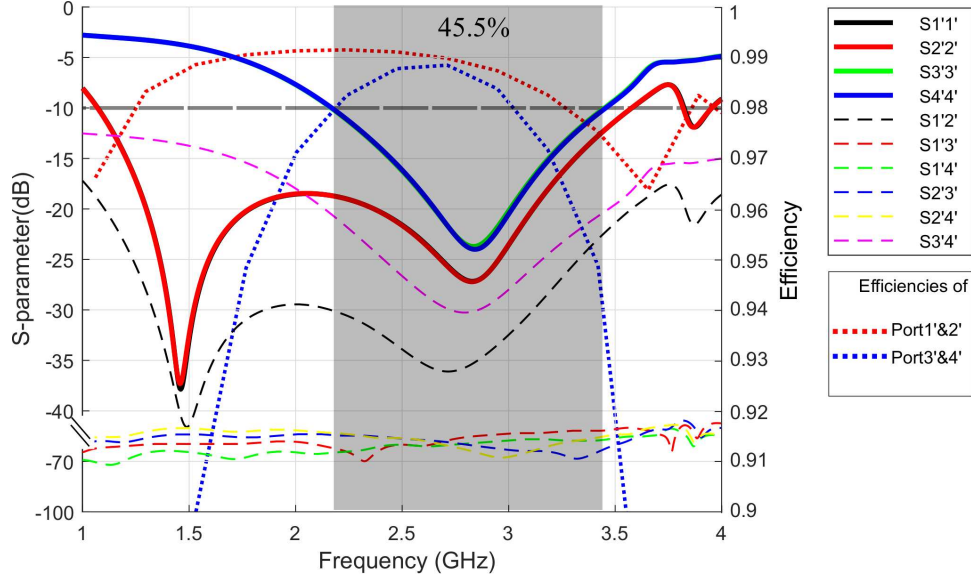


Figure 3.12: Simulated S-parameters and radiation efficiencies of the size-reduced slotted hexagonal antenna with loading inductors in Fig. 3.13 (c). The relative bandwidth of the overlapping band is 45.5%. Radiation efficiencies fluctuate within a range of 94% ~ 99% in the common band.

etched onto the edges to slow down the current, and thus decrease modal resonant frequencies, as that in [29]. The modification on antenna shape is presented in Fig. 3.13 (c). The modal patterns of the modified CMs at resonant frequencies in the comparison in Fig. 3.4 verify that each CM's operating mechanism remains unchanged, while the eigenvalue tracking in Fig. 3.14 demonstrates that the resonances of all the CMs shift to low frequency band by around 500 MHz as expected. After similar procedures and optimization as previous section, the inductor value is set to 9.5 nH. The commercial 0805CS series chip inductor by Coilcraft, Inc is used.

Simulated S-parameter and radiation efficiencies are drawn in Fig. 3.12. The common band starts from 2.17 GHz to 3.45 GHz and relative bandwidth is 45.5%. The central frequency  $f_c$  is 2.81 GHz, making the antenna outer dimension  $0.84\lambda(f_c) \times 0.73\lambda(f_c)$ . Radiation efficiencies fluctuate within a range of 94% ~ 99% in the

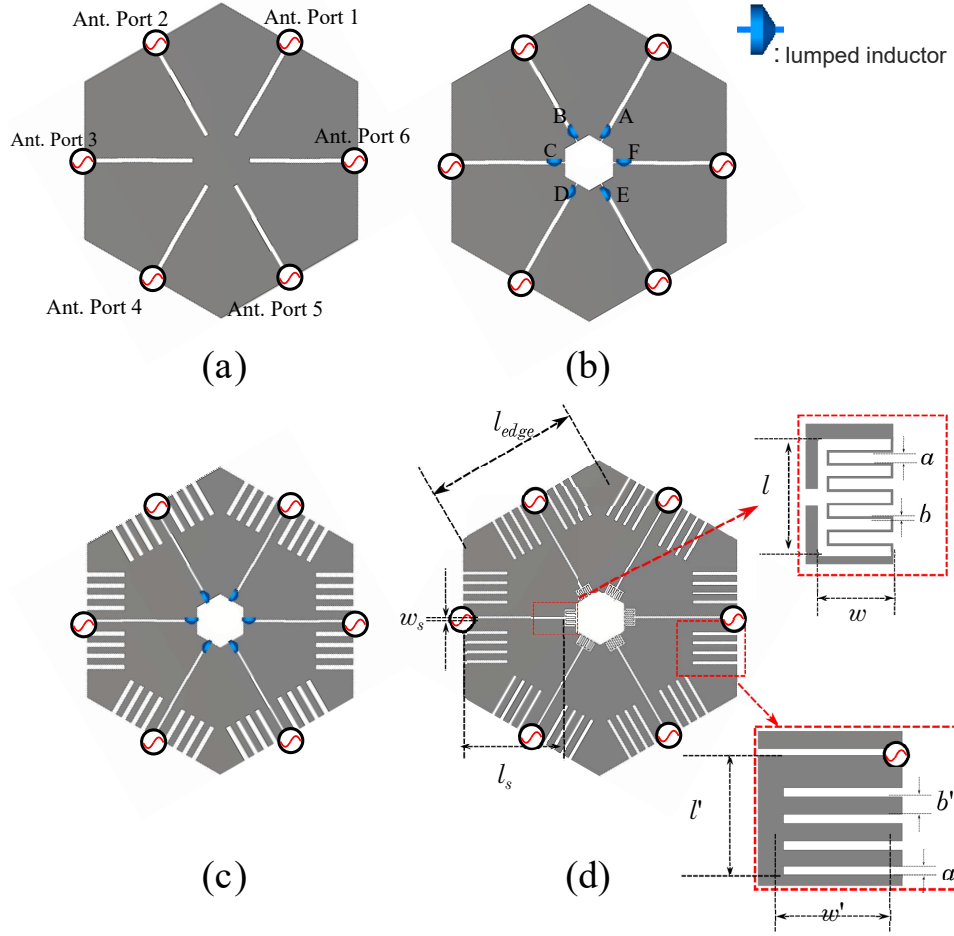


Figure 3.13: Evolution of the hexagonal antenna: (a) the slotted antenna, (b) the slotted antenna with inductive loadings, (c) the slotted antenna with six inductive loadings and edge slots (d) the slotted antenna with distributed loadings and edge slots.

common band, which are generally lower than those in Fig. 3.11. The decline in radiation efficiencies should be a result of higher value of loading inductors. The simulated radiation patterns of port  $1' \sim 4'$  at central frequency 2.8 GHz are drawn in Fig. 3.15 (a). As expected, the port patterns correspond to those modal patterns of the hexagonal plate in the bottom row of Fig. 3.4.

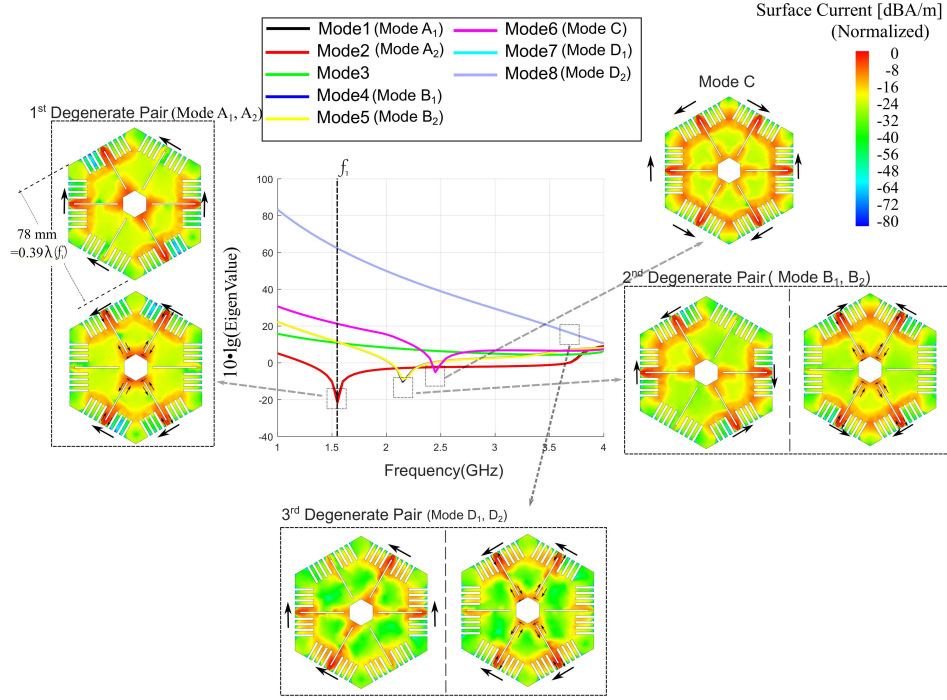


Figure 3.14: Eigenvalue tracking in decibel scale and modal current distributions of the slotted plate with central slot and edge slots. The modal resonant frequencies have moved to a lower frequency compared with those in Fig. 3.8.

### 3.6 Alternative Distribution Loading

To reduce the fabrication complexity and avoid ohmic loss of the lumped inductor of the hexagonal antenna design, a set of meandering line is used to generate distributed inductor for replacement. In [30], it is derived that the total inductance  $L$  of a meandering line is the sum of the inductance  $L_m$  of the meandering part, and the inductance  $L_l$  of the equivalent straight conductor

$$\begin{aligned}
 L &= L_m + L_l \\
 &= \frac{\mu}{\pi} \frac{l}{2} \left( \log \frac{4l}{b} - 1 \right) + Nw \log \frac{2l}{Nb} \left\{ 1 + \frac{1}{3} \left( \beta \frac{w}{2} \right)^2 \right\}
 \end{aligned} \tag{3.3}$$

where  $\mu$  and  $\beta$  are permeability and phase constant, respectively.  $w$  and  $l$  is the

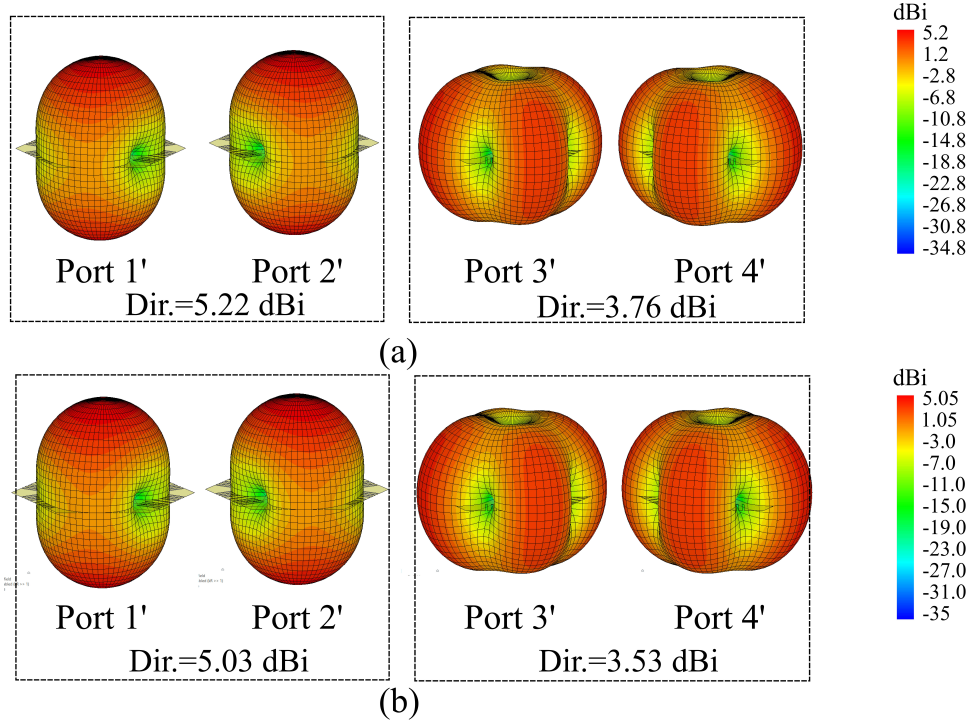


Figure 3.15: Simulated total directivity w.r.t. Ports 1' ~ 4' of the (a) slotted hexagonal antenna with lumped inductors, and (b) slotted hexagonal antenna with distributed inductors at central frequency 2.8 GHz.

overall width and length of the meandering line.  $N$  is the number of meandering turns.  $a$  and  $b$  are the line pitch and width, respectively.

The hexagonal antenna design with distributed inductor is illustrated in Fig. 3.13 (d), with all dimension details listed in Tables. 3-A. Equation (3.3) was used to calculate and optimize the inductive value of the meandering line. The calculated value of distributed inductor at 2.8 GHz is around 9.37 nH, close to the 9.5 nH lumped loading of the previous design.

Fig. 3.16 presents the S-parameters and radiation efficiencies of the final design. The  $-10$  dB common band is  $2.21 \sim 3.40$  GHz (42%). The outer dimension at the central frequency is now  $0.84\lambda(f_c) \times 0.73\lambda(f_c)$ . By replacing the lumped elements,



Table 3-A: Design parameters for the modified antenna in Fig. 3.13(mm)

$a$	$b$	$l$	$w$
0.48	0.09	6.00	3.50
$a'$	$b'$	$l'$	$w'$
0.96	1.80	13.47	12.75
$l_{edge}$	$l_s$	$w_s$	
45	28.90	0.71	

the meandering line loading leads to overall better efficiencies than the previous designs. Simulated radiation efficiencies in Fig. 3.16 varies within 98.5%  $\sim$  99.5% in the operating band. Finally, the radiation patterns of the four ports at central frequency 2.8 GHz are drawn in Fig. 3.15 (b). It shows that the port radiation patterns barely change after the distributed inductor is utilized. In addition, those total patterns correspond to the modal patterns in Fig. 3.4.

A comparison of the proposed hexagonal antennas with previous designs is presented in Table. 3-B. All the selected competitors are assigned with four ports. Most of them [3, 4, 11, 12] are designed with the guidance of TCM. Compared with previous work, the hexagonal shape has shown its advantages on supporting a multiport antenna with wider common bandwidth while maintaining high port-to-port isolation. With appropriate loadings, the four ports of proposed hexagonal antennas (lumped/distributed loading) operate with wide common bandwidths of 45.5% and 42%, respectively, with compact sizes. The presented antennas could be competitive wideband candidates for sub-6 GHz base station.

Additionally, when constructing a multimode multi-element antenna array [11] for Massive MIMO base stations, the characteristics of the hexagonal shape enable



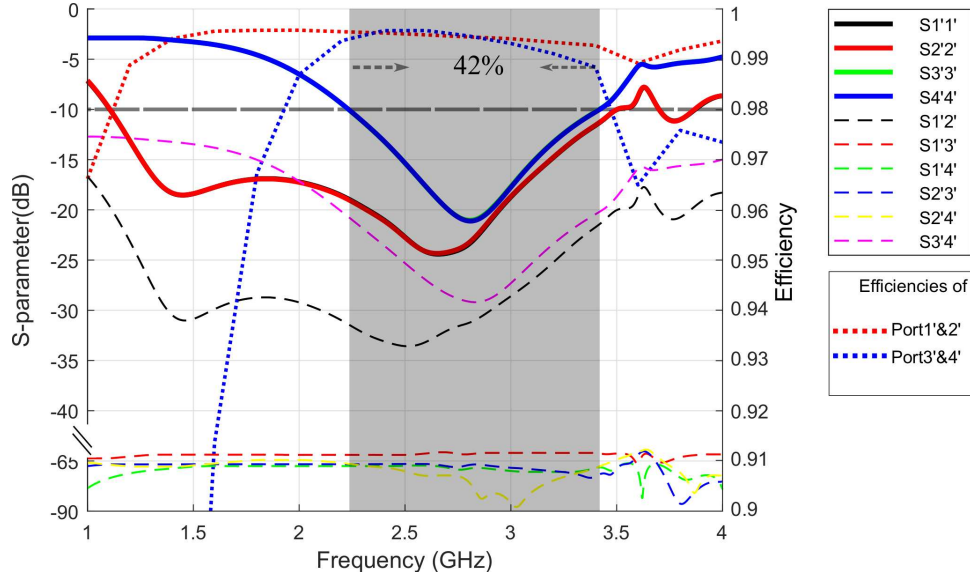


Figure 3.16: Simulated S-parameters and radiation efficiencies of the size-reduced slotted hexagonal antenna with distributed inductors in Fig. 3.13 (d). The relative bandwidth of the overlapping band is 45.5%. Radiation efficiencies fluctuate within a range of 94% ~ 99% in the common band.

the proposed antenna being laid out into a tight honeycomb structure, resulting in an even more compact overall size. And given that the hexagonal antenna design with distributed loading has saved much cost on fabrication, the proposed four-port antenna could also serve as a wide-band antenna element for Massive MIMO array.

### 3.7 Summary

With the aim of designing a multiport antenna with a wide common bandwidth, this chapter examines the CMs of several symmetrical shapes with regards to multiport antenna designs with better performance. A hexagonal plate is chosen as its two degenerate CM pairs guarantee the number of isolated ports and are close in modal resonant frequencies. Straight slots are added onto the plate and four feeding

Table 3-B: Comparison of several four-port antennas

Antennas Types	Rectangular ant. in [3]	Ring ant. in [4]	Square ant. in [26]
Feed Network Needed?	Yes	Yes	No
Frequency Band	around 2.3 ~ 2.5 GHz	around 3.2 ~ 5 GHz (−6 dB reference)	1.85 ~ 2.95 GHz
Relative Bandwidth	8.4%	43.55% (−6 dB reference)	45.8%
Outer Dimension at $f_c$	$0.8\lambda(f_c) \times 0.32\lambda(f_c)$	$0.42\lambda(f_c) \times 0.42\lambda(f_c)$	$1.12\lambda(f_c) \times 0.96\lambda(f_c)$
Reference coupling	< −12 dB	< −15 dB	< −15 dB
Antennas Types	Square ant. in [11]	Circular patch ant. in [12]	Original hex. ant. W/O loadings
Feed Network Needed?	Yes	No	Yes
Frequency Band	6 ~ 8.5 GHz	2.5 ~ 2.72 GHz	3.43 ~ 4.92 GHz
Relative Bandwidth	34%	8.4%	36.7%
Outer Dimension at $f_c$	$0.85\lambda(f_c) \times 0.85\lambda(f_c)$	$0.52\lambda(f_c) \times 0.52\lambda(f_c)$	$0.9\lambda(f_c) \times 0.78\lambda(f_c)$
Reference coupling	< −20 dB	< −18 dB	< −20 dB
Antennas Types	Proposed hex. ant. W/ lumped loading	Proposed hex. ant. W/ distributed loadings	
Feed Network Needed?	Yes	Yes	
Frequency Band	2.17 ~ 3.45 GHz	2.21 ~ 3.40 GHz	
Relative Bandwidth	45.5%	42%	
Outer Dimension at $f_c$	$0.84\lambda(f_c) \times 0.73\lambda(f_c)$	$0.84\lambda(f_c) \times 0.73\lambda(f_c)$	
Reference coupling	< −20 dB	< −20 dB	

configurations are provided to excite the degenerate CM pairs simultaneously. In order to converge the different resonant frequencies, six inductors are added onto the end of inserted slots and tune for a wide common bandwidth. Furthermore, inductive slots are cut on the plate edges and lower the operating bands. Finally, a four-port antenna with 45% relative bandwidth and compact size has been obtained and proposed. Alternatively, a similar hexagonal antenna with 41% bandwidth is presented by replacing the lumped elements with a group of meandering line to avoid ohm loss of the chip inductor. Compared with previous designs, the hexagonal antennas has proven their advantages on common bandwidth and port number.

## References

- [1] S. K. Chaudhury, W. L. Schroeder, and H. Chaloupka, “Mimo antenna system based on orthogonality of the characteristic modes of a mobile device,” in *2007 2nd International ITG Conference on Antennas*. IEEE, 2007, pp. 58–62.
- [2] M. Cabedo, M. Gallo, E. Antonino, M. Ferrando, and M. Bozzetti, “Modal analysis of a mimo antenna for sensor networks,” in *2008 IEEE Antennas and Propagation Society International Symposium*. IEEE, 2008, pp. 1–4.
- [3] S. K. Chaudhury, H. J. Chaloupka, A. Ziroff, S. Ag, C. T. Ps, and D. Munich, “Novel MIMO Antennas for Mobile Terminal,” in *Proceedings of the 38th European Microwave Conference*, 2008, pp. 1751–1754.
- [4] E. Antonino-Daviu, M. Cabedo-Fabres, M. Gallo, M. Ferrando-Bataller, and M. Bozzetti, “Design of a multimode mimo antenna using characteristic modes,” in *2009 3rd European Conference on Antennas and Propagation*, pp. 1840–1844.
- [5] S. K. Chaudhury, H. J. Chaloupka, and A. Ziroff, “Multiport antenna systems for mimo and diversity,” in *Proceeding of the 4th European Conference on Antennas and Propagation*, 2010, pp. 1–5.
- [6] A. Araghi and G. Dadashzadeh, “Oriented design of an antenna for mimo applications using theory of characteristic modes,” *IEEE Antennas and Wireless Propagation Letters*, vol. 11, pp. 1040–1043, Aug. 2012.
- [7] H. Li, Z. T. Miers, and B. K. Lau, “Design of orthogonal mimo handset antennas based on characteristic mode manipulation at frequency bands below 1 ghz,” *IEEE Transactions on Antennas and Propagation*, vol. 62, no. 5, pp. 2756–2766, 2014.
- [8] R. Martens and D. Manteuffel, “Systematic design method of a mobile multiple antenna system using the theory of characteristic modes,” *IET Microwaves*,

- Antennas Propagation*, vol. 8, no. 12, pp. 887–893, 2014.
- [9] D. Poopalaratnam, K. K. Kishor, S. M. Ieee, and S. V. Hum, “Multi-feed Chassis-mode Antenna with Dual-band MIMO operation,” in *2014 IEEE Antennas and Propagation Society International Symposium (APSURSI)*, 2014, pp. 1427–1428.
- [10] M. Bouezzeddine and W. L. Schroeder, “Design of a wideband, tunable four-port mimo antenna system with high isolation based on the theory of characteristic modes,” *IEEE Transactions on Antennas and Propagation*, vol. 64, no. 7, pp. 2679–2688, Mar. 2016.
- [11] D. Manteuffel and R. Martens, “Compact multimode multielement antenna for indoor uwb massive mimo,” *IEEE Transactions on Antennas and Propagation*, vol. 64, no. 7, pp. 2689–2697, Mar. 2016.
- [12] D. Yang, H. Zeng, R. Chen, J. Qu, Y. Wen, and S. Liu, “Four port compact multimode patch antenna system for vehicular application,” *2016 IEEE International Workshop on Electromagnetics, iWEM 2016 - Proceeding*, pp. 21–23, 2016.
- [13] D.-W. Kim and S. Nam, “Systematic Design of a Multiport MIMO Antenna with Bilateral Symmetry Based on Characteristic Mode Analysis,” *Transactions on Antennas and Propagation*, vol. 66, no. 3, pp. 1076–1085, 2017.
- [14] K. Li, Z.-G. Ban, Y. Shi, and L. Li, “Design of Wideband MIMO Handset Antennas Using Characteristic Modes,” in *2017 Sixth Asia-Pacific Conference on Antennas and Propagation (APCAP)*. IEEE, 2017, pp. 1–3.
- [15] K. K. Kishor, S. Member, and S. V. Hum, “Multiport Multiband Chassismode Antenna Design Using Characteristic Modes,” *IEEE Antennas and Wireless Propagation Letters*, vol. 16, pp. 609–612, 2017.
- [16] E. Antonino-Daviu, F. Ferrero, and M. Ferrando-Bataller, “Multimode antenna for GPS applications,” *2020 International Workshop on Antenna Technology*,

- iWAT 2020*, pp. 7–9, 2020.
- [17] R. Harrington and J. Mautz, “Theory of characteristic modes for conducting bodies,” *IEEE Transactions on Antennas and Propagation*, vol. 19, no. 5, pp. 622–628, Sep. 1971.
- [18] R. Harrington, J. Mautz, and Y. Chang, “Characteristic modes for dielectric and magnetic bodies,” *IEEE Transactions on Antennas and Propagation*, vol. 20, no. 2, pp. 194–198, Mar. 1972.
- [19] N. Peitzmeier and D. Manteuffel, “Selective excitation of characteristic modes on an electrically large antenna for MIMO applications,” in *12th European Conference on Antennas and Propagation (EuCAP 2018)*, vol. 2018, 2018, pp. 1–5.
- [20] B. D. Raines and R. G. Rojas, “Wideband tracking of characteristic modes,” in *Proceedings of the 5th European Conference on Antennas and Propagation (EUCAP)*. IEEE, 2011, pp. 1978–1981.
- [21] Z. Miers and B. K. Lau, “Wideband characteristic mode tracking utilizing far-field patterns,” *IEEE Antennas and Wireless Propagation Letters*, vol. 14, pp. 1658–1661, 2015.
- [22] M. Masek, M. Capek, and L. Jelinek, “Modal Tracking Based on Group Theory,” *IEEE Transactions on Antennas and Propagation*, vol. 68, no. 2, pp. 927–937, 2020.
- [23] J. B. Knorr, “Consequences of Symmetry in the Computation of Characteristic Modes for Conducting Bodies,” *IEEE Transactions on Antennas and Propagation*, vol. 21, no. 6, pp. 899–902, 1973.
- [24] H. Jaafar, S. Collardey, and A. Sharaiha, “Optimized manipulation of the network characteristic modes for wideband small antenna matching,” *IEEE Transactions on Antennas and Propagation*, vol. 65, no. 11, pp. 5757–5767, 2017.

- [25] Q. Wu, W. Su, Z. Li, and D. Su, “Reduction in out-of-band antenna coupling using characteristic mode analysis,” *IEEE Transactions on Antennas and Propagation*, vol. 64, no. 7, pp. 2732–2742, July 2016.
- [26] A. Moradikordalivand, T. A. Rahman, and M. Khalily, “Common Elements Wideband MIMO Antenna System for WiFi / LTE Access-Point Applications,” *IEEE Antennas and Wireless Propagation Letters*, vol. 13, pp. 1601–1604, 2014.
- [27] Y. Chen and C.-F. Wang, *Characteristic modes: Theory and applications in antenna and engineering*. John Wiley & Sons, 2015.
- [28] R. F. Harrington, “Control of Radar Scattering by Reactive Loading,” *IEEE Transaction Antennas Propagation*, vol. 1972, no. 4, pp. 446–454, 1972.
- [29] J. Sarrazin, Y. Mahé, S. Avrillon, and S. Toutain, “A new multimode antenna for mimo systems using a mode frequency convergence concept,” *IEEE Transactions on Antennas and Propagation*, vol. 59, no. 12, pp. 4481–4489, Aug. 2011.
- [30] T. Endo, Y. Sunahara, S. Satoh, and T. Katagi, “Resonant Frequency and Radiation Efficiency of Meander Line Antennas,” *Electronics and Communications in Japan (Part II: Electronics)*, vol. 83, no. 12, pp. 52–58, 2000.

## Chapter 4

# Radiation Energy and Mutual Coupling Evaluation

### 4.1 Introduction

In the last chapter, a wideband multiport antenna with the help of TCM has been designed. It shows that by providing distinct insights into operating mechanisms of antennas, TCM significantly benefits the design of multiport antennas [1–3]. Since their corresponding modal far-field patterns are orthogonal to each other by nature, exciting those characteristic modes (CMs) through specific feeding methods results in high port-to-port isolation. Thus, The ports of the TCM-motivated MIMO antenna design are naturally highly isolated.

Although TCM has inspired a large number of multiport antenna designs, its strong advantage is not only to design a new one, but also in its ability to analyse an existing one. One of its most desirable features is the unique analytical perspective on arbitrary antennas. TCM offers a way to linearly decompose antennas' operating

state, including the radiation pattern, current distribution, and port admittance. In [4], the Q factor of an antenna is interpreted in a linear format and decomposed into a series of modal Q factors. In [5], the antenna impedance and radiation are equivalent to parallel circuits according to the characteristic modes. In [6], CMA has been used to reduce the out-of-band coupling, as the evaluation of mutual coupling was introduced as a modal admittance (MA). Moreover, it was shown that the modal mutual coupling can be calculated between CMs and it can be used to identify certain CMs to suppress.

However, the proposed work in [6] only discussed a two-element system and did not address the design of multiport antennas. Additionally, while many existing MIMO researches [1, 3, 7] included feeding networks, the effect of feeding network on coupling research was not included. Overall, there is a lack of a sufficiently clear method in TCM that can accommodate a higher number of ports

In this chapter, a new method to evaluate the CM radiation and coupling is presented. Supported by theoretical analyses and derivations, the proposed method can be adopted to analyse multiport antenna systems with feeding networks. Theoretical derivations of this method are proposed in this chapter, in comparison with the previous CMA-coupling method [6]. Further validation and applications of this method will be demonstrated in the next chapter. All calculation of CMs in this chapter are performed in the MATLAB environment, utilizing an impedance matrix generated from FEKO.

## 4.2 Mutual Coupling Evaluation in the CMA Sense

In this section, the relationship between mutual coupling and each CM will be derived. As already listed, for a conducting (or complex) body with incident



electromagnetic wave on its surface, the surface current and scattering field can be decomposed into several characteristic modes,

$$\mathbf{J} = \sum_{n=1}^{\infty} \frac{V_n^i \mathbf{J}_n}{1 + j\omega_n} = \sum_{n=1}^{\infty} \frac{\langle \mathbf{J}_n, \mathbf{E}^i \rangle}{1 + j\omega_n} \mathbf{J}_n \quad (4.1)$$

and its electronic-field version:

$$\mathbf{E} = \sum_{n=1}^{\infty} \frac{V_n^i \mathbf{E}_n}{1 + j\omega_n} = \sum_{n=1}^{\infty} \frac{\langle \mathbf{J}_n, \mathbf{E}^i \rangle}{1 + j\omega_n} \mathbf{E}_n \quad (4.2)$$

where  $\omega_n$ ,  $\mathbf{J}_n$  and  $\mathbf{E}_n$  are eigenvalue, modal current and modal field for the  $n_{th}$  mode, respectively.  $V_n^i$  denotes modal excitation coefficient, which is the inner product of two vectors: surface current  $\mathbf{J}_n$  and incident excitation  $\mathbf{E}^i$ . It needs to be mentioned that, the eigenvalue, one of the most simple yet crucial property of characteristic mode, plays an important role as indicating the radiating ability of each mode. For arbitrary Mode  $m$  and  $n$ , there is [8],

$$\omega_n \delta_{mn} = \omega \oint_S (\mu H_m \cdot H_n^* - \epsilon E_m \cdot E_n^*) d\Omega \quad (4.3)$$

where the  $\delta_{mn}$  is Kronecker delta =  $\begin{cases} 1, & m = n \\ 0, & m \neq n \end{cases}$ .  $\mu$  and  $\epsilon$  are the permittivity and permeability of free space, respectively. According to (4.3), when  $m = n$ , the sign of eigenvalue  $\omega_n$  determines which kind of energy this mode stores: when  $\omega_n > 0$ , Mode  $n$  stores magnetic energy, while when  $\omega_n < 0$ , Mode  $n$  stores electric energy. (4.3) also indicates that the smaller  $\omega_n$  is, the more energy it could radiate.

When a unit incident excitation occurs at the  $p_{th}$  mesh edge, it can be expressed as [6], [9],

$$\mathbf{E}^i = \mathbf{e}_p \delta(\mathbf{r}') \quad (4.4)$$

where  $\mathbf{e}_p$  is a unit vector normal to the  $p_{th}$  edge and  $\mathbf{r}'$  is a radius vector. The modal excitation coefficient  $V_n^i$  is obtained from [6],

$$V_n^i = V_1 I_n(p) l_p \quad (4.5)$$

where  $V_1$  is the magnitude of the input excitation.  $I_n(p)$  is the  $p_{th}$  current coefficient for the  $n_{th}$  modal current and  $l_p$  is the corresponding edge length.

Furthermore, the radiation power  $P_{rad}$  of the output wave at infinite is,

$$P_{rad} = \frac{1}{\eta} \oint\!\!\!\oint_{S_\infty} \mathbf{E} \cdot \mathbf{E}^* d\Omega. \quad (4.6)$$

Apply simplified modal coefficients given by (4.5), the decomposition of E-field in (4.2) and their orthogonality:

$$\frac{1}{\eta} \oint\!\!\!\oint_{S_\infty} \mathbf{E}_m \cdot \mathbf{E}_n^* d\Omega = \delta_{mn} \quad (4.7)$$

to (4.6) and get,

$$\begin{aligned} P_{rad} &= \frac{1}{\eta} \oint\!\!\!\oint_{S_\infty} \sum_{n=1}^{\infty} \frac{V_n^i \mathbf{E}_n}{1 + j\omega_n} \cdot \left( \sum_{m=1}^{\infty} \frac{V_m^i \mathbf{E}_m}{1 + j\omega_m} \right)^* d\Omega \\ &= \frac{1}{\eta} \oint\!\!\!\oint_{S_\infty} \sum_{n=1}^{\infty} \frac{V_n^i \mathbf{E}_n}{1 + j\omega_n} \cdot \sum_{m=1}^{\infty} \frac{V_m^i \mathbf{E}_m^*}{1 - j\omega_m} d\Omega \\ &= \frac{1}{\eta} \sum_{n=1}^{\infty} \frac{(V_1 I_n(p) l_p)^2}{1 + \omega_n^2} \oint\!\!\!\oint_{S_\infty} \mathbf{E}_n \cdot \mathbf{E}_n^* d\Omega \\ &= \sum_{n=1}^{\infty} \frac{(V_1 I_n(p) l_p)^2}{1 + \omega_n^2} \\ &\approx \sum_{n=1}^N \frac{(V_1 I_n(p) l_p)^2}{1 + \omega_n^2} = \sum_{n=1}^N |\alpha_n|^2 \end{aligned} \quad (4.8)$$

where  $\eta$  is the space wave impedance and  $\alpha_n^2$  is modal weighting coefficient (MWC)

for the  $n_{th}$  mode with specified excitation.

When the similar approach is applied on a  $2 \times 2$  antenna array system to measure its mutual coupling, substituted with (4.2), (4.5), (4.6), the Envelope Correlation Coefficient (ECC) is derived as,

$$\begin{aligned}
 \rho_{ECC} &= \frac{\oint_S E_1 \cdot E_2^* d\Omega}{\sqrt{\oint_S E_1 \cdot E_1^* d\Omega \oint_S E_2 \cdot E_2^* d\Omega}} \\
 &= \frac{1}{\eta \sqrt{P_{rad1} P_{rad2}}} \oint_{S_\infty} \sum_{n=1}^{\infty} \frac{V_n^{1i} \mathbf{E}_n}{1 + j\omega_n} \left( \sum_{m=1}^{\infty} \frac{V_m^{2i} \mathbf{E}_m}{1 + j\omega_m} \right)^* d\Omega \\
 &= \frac{\sum_{n=1}^{\infty} (V_1 V_2 I_n(p) I_n(q) l_p l_q)}{(1 + \omega_n^2) \sqrt{P_{rad1} P_{rad2}}} \quad (4.9) \\
 &= \sum_{n=1}^{\infty} \left( \frac{1}{\sqrt{1 + \omega_n^2}} \frac{V_1 I_n(p) l_p}{\sqrt{P_{rad1}}} \right) \left( \frac{1}{\sqrt{1 + \omega_n^2}} \frac{V_2 I_n(q) l_q}{\sqrt{P_{rad2}}} \right) \\
 &\approx \sum_{n=1}^N M_{1n} M_{2n}
 \end{aligned}$$

where  $\left( \frac{1}{\sqrt{1 + \omega_n^2}} \frac{V_i I_n(p) l_p}{\sqrt{P_{radi}}} \right)$  is shorted as  $M_{in}$  and will be explained later.

Also, (4.8) can be normalized as,

$$1 = \sum_{n=1}^N \frac{(V_1 I_n(p) l_p)^2}{(P_{rad1})(1 + \omega_n^2)} = \sum_{n=1}^{\infty} M_{1n}^2 \quad (4.10)$$

The above derivation holds on the assumption that antenna port 1 lays on the  $p_{th}$  non-boundary mesh edge only and port 2 on the  $q_{th}$  edge.

$M_{1n}$  or  $M_{2n}$  can easily be calculated through CMA methods. (4.10) shows the energy contribution of each mode in far-field radiation while (4.9) illustrates how those modes coupling with each other in far-field. Thus, we name  $M_{1n}$  as the  $n_{th}$  **Modal Energy Occupied Coefficient** (MEOC) for port 1.

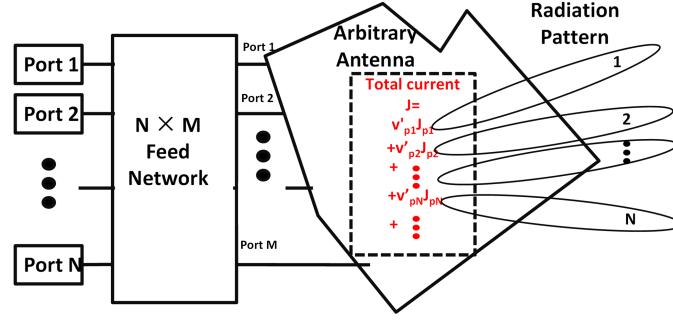


Figure 4.1: Schematic view of multiport antenna radiation.

### 4.3 MEOC for Multimode MIMO System

A general multimode antenna system should be constructed as shown in Fig. 4.1.  $N$  ports are used to feed the antenna through a  $N \times M$  ( $N \leq M$ ) feeding network and each port excites a particular radiation pattern. At low frequency, where only a few CMs have resonating potentials, high isolation is achieved once each port excites a single CM with no interference from other ports. However, the number of ports is limited as there are only a few dominant CMs at low frequency. As the frequency rises, the increasing number of CMs makes it possible to realize more input ports. Nevertheless, the case becomes complex, as each port is likely to excite multiple CMs with different characterises at the same time. Although the requirement seems strict, TCM can still be used to analyse the resonance and coupling in a sense of CMs.

In [6], the modal self- and mutual- admittance (MSA, MMA) are obtained as,

$$\begin{aligned}
 Y_{11} &= \sum_{n=1}^{\infty} MSA = \sum_{n=1}^{\infty} \frac{(I_n(p)l_p)^2}{1 + j\omega_n} \\
 Y_{21} &= \sum_{n=1}^{\infty} MMA = \sum_{n=1}^{\infty} \frac{I_n(p)I_n(q)l_pl_q}{1 + j\omega_n}
 \end{aligned} \tag{4.11}$$

Modal admittance relate to MEOC as,

$$\begin{aligned} M_{1n}^2 &= \frac{V_1^2}{2P_{rad1}}(MSA + MSA^*) \\ M_{1n}M_{2n} &= \frac{V_1V_2}{2\sqrt{(P_{rad1}P_{rad2})}}(MMA + MMA^*) \end{aligned} \quad (4.12)$$

Thus, a coupling matrix relates to the admittance matrix as,

$$\begin{aligned} & \mathbf{real} \begin{bmatrix} Y_{11} & \cdots & Y_{1N} \\ Y_{21} & \cdots & Y_{2N} \\ \vdots & \cdots & \vdots \\ Y_{N1} & \cdots & Y_{NN} \end{bmatrix} \\ &= \mathbf{p}I_{N \times N} \begin{bmatrix} \sum M_{1n}M_{1n} & \cdots & \sum M_{1n}M_{Nn} \\ \sum M_{2n}M_{1n} & \cdots & \sum M_{2n}M_{Nn} \\ \vdots & \cdots & \vdots \\ \sum M_{Nn}M_{1n} & \cdots & \sum M_{Nn}M_{Nn} \end{bmatrix} (\mathbf{p}I_{N \times N})^H \\ &= \sum_{n=1}^{\infty} \left( \mathbf{p}I_{N \times N} \begin{bmatrix} M_{1n}M_{1n} & \cdots & M_{1n}M_{Nn} \\ M_{2n}M_{1n} & \cdots & M_{2n}M_{Nn} \\ \vdots & \cdots & \vdots \\ M_{Nn}M_{1n} & \cdots & M_{Nn}M_{Nn} \end{bmatrix} (\mathbf{p}I_{N \times N})^H \right) \\ &= \sum_{n=1}^{\infty} \left( \mathbf{p}I_{N \times N} [\widetilde{M_{N \times N}}] (\mathbf{p}I_{N \times N})^H \right) \end{aligned} \quad (4.13)$$

where  $\mathbf{p} = [\frac{\sqrt{P_{rad1}}}{V_1}, \frac{\sqrt{P_{rad2}}}{V_2}, \dots, \frac{\sqrt{P_{radN}}}{V_N}]$  is the vector to normalize MEOC according to radiation energy from each port.  $I_{N \times N}$  is a  $N \times N$  unit matrix.  $[\widetilde{M_{N \times N}}]$  is the matrix assignment of MEOC.  $N$  represents the number of MIMO dimension.

(4.13) enables the utilization of typical linear matrix transformation for MEOC. It would be easy to get the following transformation:

if:

$$[Y_{new}] = T[Y_0]T^H$$

then:

(4.14)

$$\begin{aligned} & [\widetilde{M_{N \times N, new}}] \\ &= \{[\mathbf{p}_{new}I]^{-1}T[\mathbf{p}I]\}[\widetilde{M_{N \times N, 0}}]\{[\mathbf{p}_{new}I]^{-1}T[\mathbf{p}I]\}^H \end{aligned}$$

in which  $[T]$  is a  $M \times N$  transformation matrix representing effects from the feeding structure, and  $[Y_{new}]$ ,  $[\widetilde{M_{N \times N, new}}]$  are the results after transformation. The diagonal elements of  $[\widetilde{M_{N \times N, new}}]$  describe the energy occupancy of external ports according to CMs, while non-diagonal element describes how each port couples together in far-field.

Since the normalization vector  $\mathbf{p}$  varies with the input voltage amplitude, it is not easy to obtain in the calculation of (4.13) and (4.14). Moreover, we noticed that the (4.10) makes every diagonal element of the sum  $\sum[\widetilde{M_{N \times N}}]$  unity. With the help of (4.10), each  $M_{in}$  can be normalized to the right value.

It should be noticed that the advantage of  $[\widetilde{M_{N \times N, new}}]$  holds on the condition of far-field when modal fields are orthogonal. When it comes to the near field or port-to-port coupling, reactive behaviour of modes cannot be omitted, thus each mode couple with each other and makes the situation complex.

## 4.4 Numerical Examples

### 4.4.1 Coupling Analysis on a Twin-dipole System

A twin-dipole system was discussed in [6] to study and reduce the out-of-band coupling or, Electromagnetic Interference (EMI) from lower frequency antenna to higher frequency antenna with the help of CMA's modal admittance. The analysis is carried out in this section again using the proposed MEOC method to compare it with the previous work.

As shown in Fig. 4.2, One dipole (Ant. 1) resonates at  $f_1 = 140$  MHz and the other one (Ant. 2)  $f_2 = 280$  MHz. Two dipoles are separated by  $75\text{ cm}$  ( $0.7\lambda_2$ ) to make sure the interfere from Ant. 1 is transmitted to Ant. 2 through far field radiation.

#### 4.4.1.1 MEOC Analysis on the Twin-dipole system

With the help of (4.9), the MEOC analysis of the system at  $f_2$  is calculated and shown in Fig. 4.3. The order of CMs is determined by the absolute values of their corresponding eigenvalues in ascending order at 280 MHz. The red and blue bars in this chart represent the MEOC of Ant. 1 and Ant. 2, respectively, while the overlapping grey bars denotes the modal significance (MS). As the radiating energy is strongly concentrated at antenna's lower modes, the figure is plotted in decibel ordinate. Therefore, each mode's contribution on the system's coupling, i.e.,  $M_1 M_2$  in (4.9), is now the sum of both MEOC, i.e.,  $M_1(dB) + M_2(dB)$ . The modal coupling in Fig. 4.3 is then the sum of both bar lengths.

The energy among each CMs is firstly studied. As is shown in Fig. 4.3, while

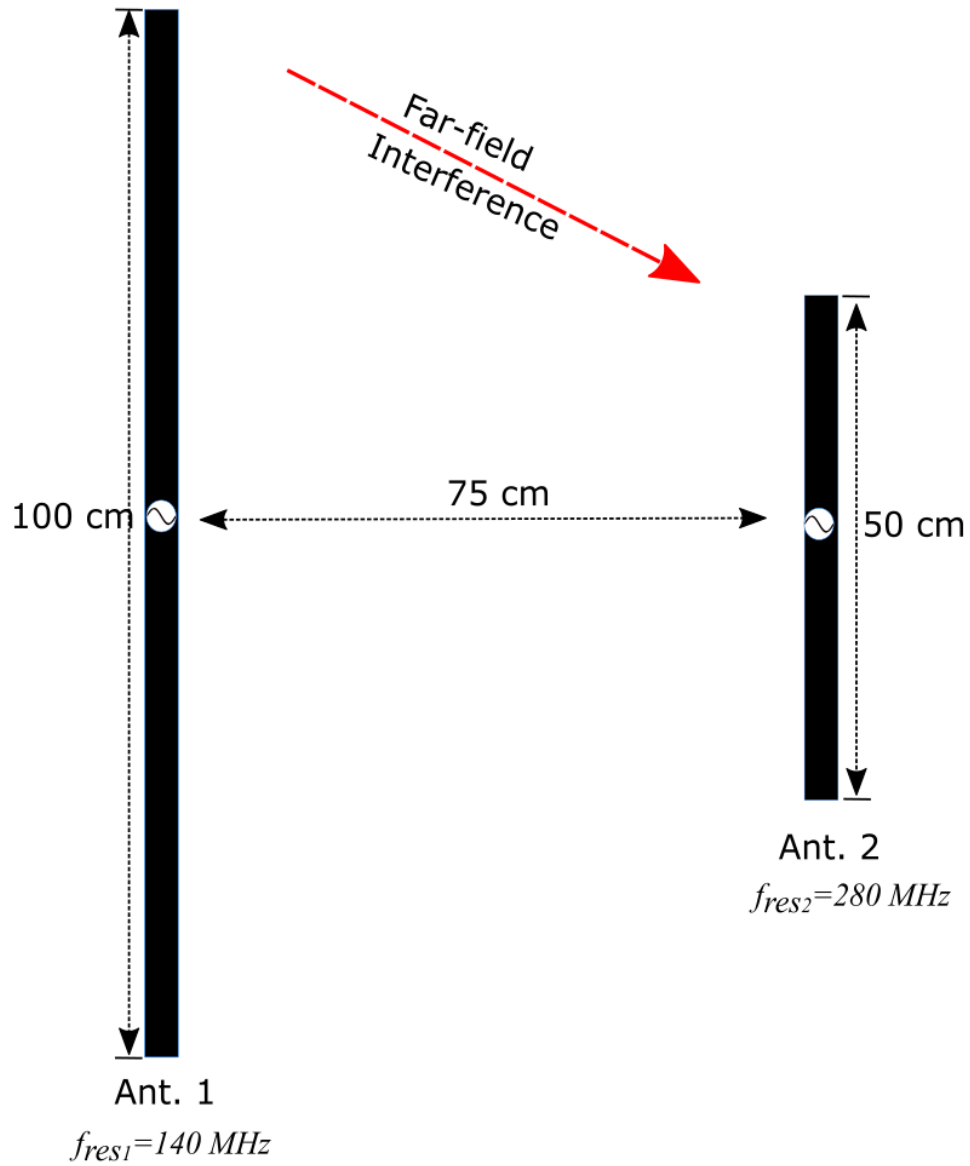


Figure 4.2: Two dipoles with different length are placed in space with a distance of 75 cm. The operating frequency is Ant. 2's resonance (280 MHz)

the length of each bar represents the energy distribution, the majority energy radiated by Ant. 2 is radiated from Mode 1 of the system, while most energy radiated by Ant. 1 is emitted from Mode 2. Ant. 1 also radiates a much smaller amount of energy from Mode 4 than from Mode 2 (more than -15 dB). As for the other



high-order modes (e.g., Mode 7 ~ 13), their contributions on both radiation and coupling are too small to be negligible. Mode 1 and 2 are called 'functional mode' of Ant. 2 and Ant. 1, respectively.

Notice that in the decibel ordinate, the modal coupling is represented by the sum of the length of both bars. It is obvious that Mode 1, 2 and Mode 4 are responsible for most of the coupling. Therefore, manipulating these three CMs could easily reduce the coupling. There is also a noticeable coupling on the higher order Mode 10. However, considering the length sum, the coupling on Mode 10 is much smaller than that on the other three CMs. Modifications to reduce coupling on Mode 10 could be useful, but would be less effective.

Though Mode 1, 2 are the main sources of mutual coupling, any changes to them easily influence the performance of the system. Mode 4, despite its relatively smaller amount MEOC, is enough to cause considerable interference on Ant. 2. As Mode 4 is not the functional mode of both Ant. 1 and Ant. 2 and affects little on the radiation performance, it can be chosen as the "Target Mode" and suppressed, in order to reduce the total coupling between Ant. 1 and Ant. 2.

Therefore, MEOC analysis visualizes and locates the CM to be suppressed. According to the current or field distribution of the "Target Mode", various means can be used to suppress it and reduce coupling [6, 10, 11]. Considering that the main focus of this chapter is to evaluate rather than suppress the coupling, the following emphasis will be on comparing the advantages of the evaluation methods used in this chapter with other approaches. The suppression method will not be discussed in this chapter.

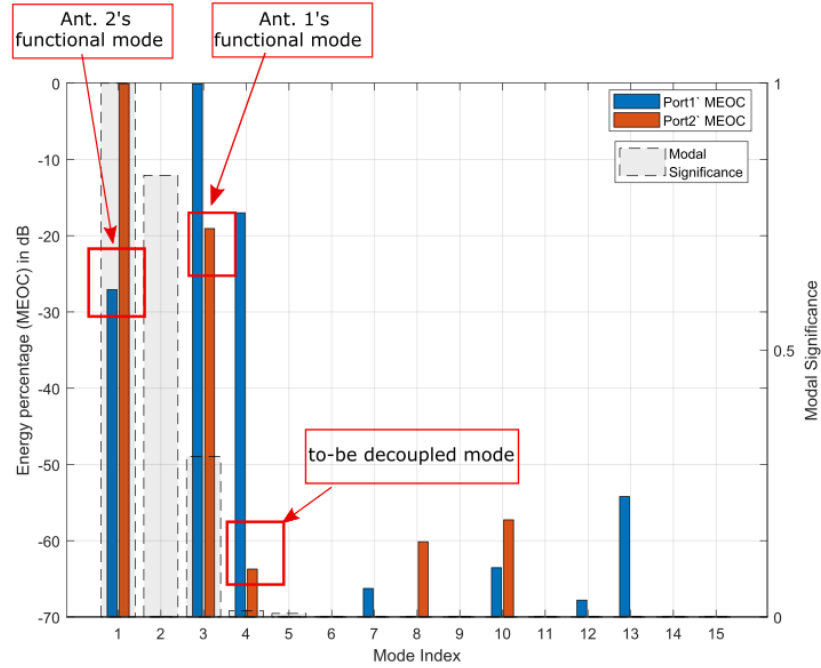


Figure 4.3: MEOC analysis and modal significance of the twin-dipole at 280 MHz. The order and naming rules of CMs is determined by the absolute values of their corresponding eigenvalues in ascending order at 280 MHz. The figure is plotted in decibel scale. It is shown that radiation by Ant. 1 is dominated by Mode 2 and 4. For Ant. 2, the dominant modes is Mode 1.

#### 4.4.1.2 Comparison between the MEOC analysis and MA Analysis [6]

On the other hand, according to the coupling analysis in [6], the MAs of both ports are listed in a three-row table as shown in Table 4-A. A similar analysis process is carried out. According to the values of all three rows in Table 4-A, Mode 1, 2 and 4 are considered to have the greatest contribution to the coupling. Mode 4 is chosen for its lesser effect on the performance. It is then suppressed to improve the isolation in the twin dipole system.

Compared with the proposed MEOC method, the MA analysis method in [6]

Table 4-A: The real part of modal admittance (MA) of the first 6 modes of the twin-dipole system [6]

	Mode1	Mode2	Mode3	Mode4	Mode5	Mode6
Y11	7.2E-7	1.96E-12	1.23E-3	1.62E-3	1.99E-6	1.05E-7
Y12	7.7E-5	4.51E-12	4.46E-4	1.89E-4	2.91E-5	1.5E-9
Y22	8.01E-3	1.31E-11	1.76E-4	2.21E-5	3.96E-4	1.96E-11

is inconvenient in several ways. All three rows in Table 4-A need to be considered simultaneously for larger MAs, which is obviously not direct or clear compared with the proposed MEOC method shown in Fig. 4.2. Furthermore, when the frequency increases and higher order CMs are significant, it is challenging to analyse more than ten CMs simultaneously using the MA analysis method, whether the MAs are compared in a three-row table or plotted in figures. For example, the higher order mode 10 in Fig. 4.2, which can be easily observed by MEOC analysis, is easily overlooked in MA analysis method. Moreover, in order to avoid comparing on complex value, the imaginary part of MAs in Table 4-A is omitted, and the distribution of radiation energy among CMs is not directly illustrated and remains hidden. Therefore, to locate all the CMs that dominate the radiation in MA method, additional parameters such as MWC need to be calculated. However, this is not necessary when MEOC, which also represents the radiation as shown in (4.10), is computed at the beginning.

In summary, the method of MEOC proposed a direct and clear way to interpret the coupling and radiation of antennas in the CMA sense. In the next section, the discuss will go further and focus on a four-port problem. The transformation of the feeding network (4.14) will also be included.

## 4.4.2 Coupling Analysis on a Four-port Square Plate

In this section, another example is discussed to further validate the use of MEOC. Different from the one-dimensional dipole example in last section, the square shape, which has been discussed in the previous chapter, will be transformed into an antenna with four ports and discussed as an example for MEOC analysis. Furthermore, as multiple CMs are excited on the antenna by a feeding network, (4.14) will be used to calculate MEOC in this section.

### 4.4.2.1 A Wide-band Open-end Slot

Firstly, to enable later excitation of CMs, an open-end slot [12], [13] is first introduced here. As shown in Fig. 4.4, the total length of the slot is 30 mm, and the first step is 21.6 mm. This stepped slot is fed at the edge and it works at 3 ~ 6 GHz. Its wide-band performance benefits from the stepped slot width. The central frequency 4.5 GHz is chosen for the following analysis.

Unlike the straight slot in Chapter 3, the stepped slot could result in a wider impedance bandwidth for multiport antenna design. However, more CMs could be involved in the radiation, making the analysis challenging due to its wideband feature.

### 4.4.2.2 MEOC Analysis for a Square Plate

The open-end slots will be used in this section to construct a square antenna. The length of the square is 78 mm (about  $1.1\lambda_{4.5GHz}$ ). The ends of four open-end slots are inserted on every outline edge of a square plate and act as antenna port 1 ~ 4. Port 1 ~ 4 are fed through a feeding network by input port 1' ~ 4' according to the

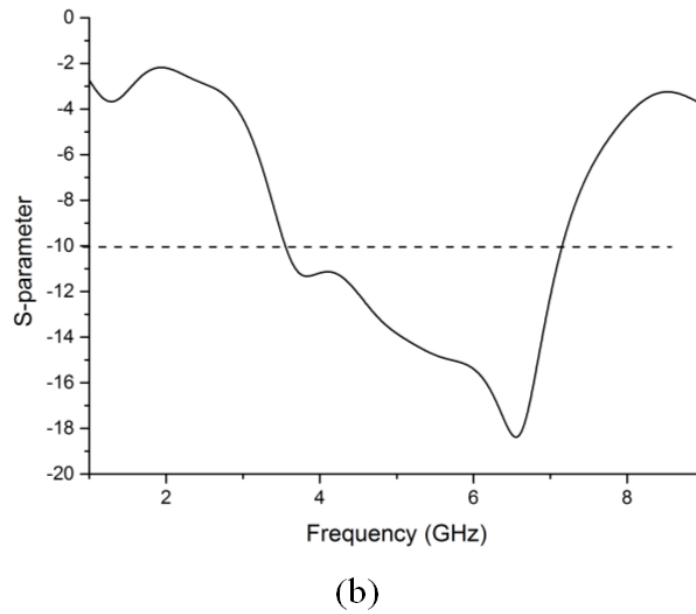
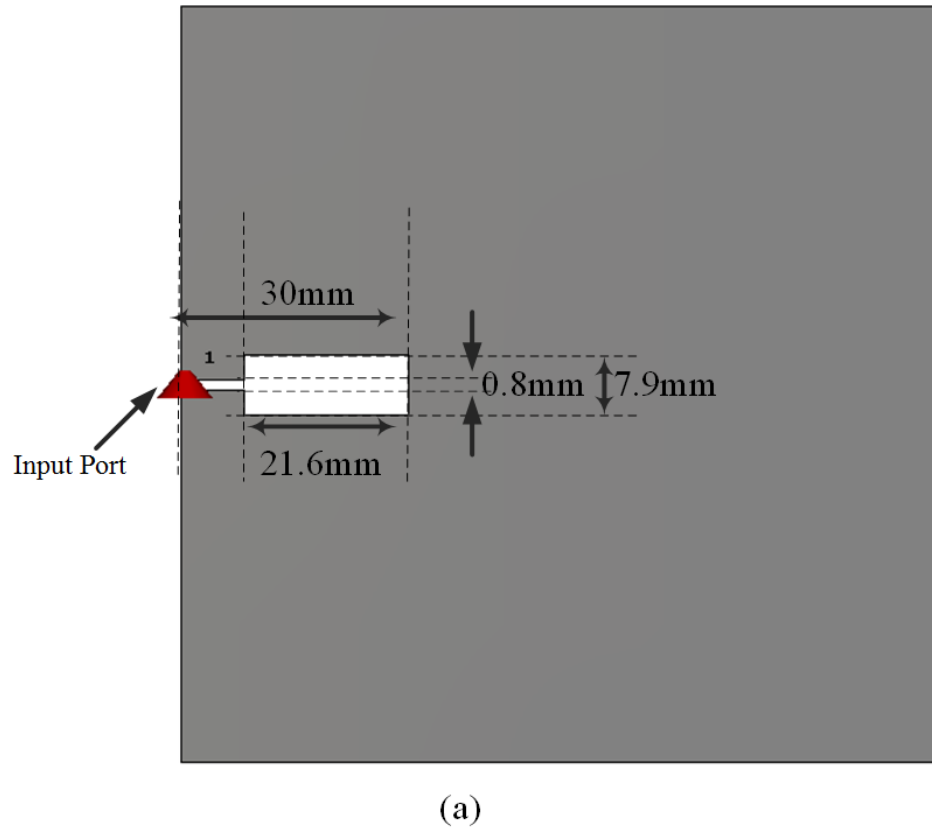


Figure 4.4: The stepped slot structure. (a) the structure of the slot (b) the S-parameter of this slot. The length of slot is 30 mm. This slot is fed at its end and works at 3 ~ 6.5 GHz.

illustration in the left side of Fig. 4.5. Port  $1' \sim 4'$  represent four different feeding schemes including two sets of odd and even modes, which can easily be realized with two  $180^\circ$  hybrids. The combination of antenna port 1, 2 and a  $180^\circ$  hybrid are usually used as the simplest decoupling feeding network on the symmetric-located antenna ports 1 and 2 [7]. So it is the same with port 3, 4.

For antenna port 1 and 2, their symmetric input admittance matrix  $[Y]$  can be diagonalized by decoupling matrix  $V_2$ , i.e., [14]

$$\begin{bmatrix} Y'_{11} & Y'_{12} \\ Y'_{21} & Y'_{22} \end{bmatrix} = V_2 \begin{bmatrix} Y_{11} + Y_{12} & \\ & Y_{22} - Y_{21} \end{bmatrix} (V_2)^H \quad (4.15)$$

$$V_2 = \frac{1}{\sqrt{2}} \begin{bmatrix} 1 & 1 \\ 1 & -1 \end{bmatrix}$$

where  $[Y']$  is the admittance matrix on the input port  $1', 2'$  after decoupling. With the benefit of (4.13), the relationship between input ports  $1' \sim 4'$  to antenna ports  $1 \sim 4$  should be,

$$[Y'] = T[Y]T^H$$

$$[\widetilde{M}] = \{[\mathbf{p}'I]^{-1}T[\mathbf{p}I]\}[\widetilde{M}]\{[\mathbf{p}'I]^{-1}T[\mathbf{p}I]\}^H$$

where,

$$T = \begin{bmatrix} I_{2 \times 2} & \\ & V_2 \end{bmatrix} \begin{bmatrix} V_2 & \\ & I_{2 \times 2} \end{bmatrix}, \quad (4.16)$$

$$V_2 = \frac{1}{\sqrt{2}} \begin{bmatrix} 1 & 1 \\ 1 & -1 \end{bmatrix}.$$

With the help of (4.16), MEOC analysis at 4.5 GHz is shown in the right side of Fig. 4.5. The order of CMs is determined by the absolute values of their corre-

sponding eigenvalues in ascending order. When MEOC is utilized in the analysis, how strong each port couples on each mode can be visualized clearly. Even before giving the S-parameter, the MEOC analysis predicts that odd feed port 2' and 4' are very likely to be coupled. Moreover, it shows that Mode 10, 11, 12, and 16 are responsible for the coupling. As the MEOC tells how much one mode participates in the total radiation of a certain port, the figure also gives a detailed modal energy distribution presentation on all ports. Different from the previous MA method [6], MEOC visualizes all those information in the diagram.

This information will be used later for analysis and construction of a broadband multiport antenna in the next chapter.

#### 4.4.2.3 Comparison between the MEOC analysis and MA Analysis [6]

On the other hand, MAs of all ports are listed in Table 4-B. Considering the same number of CMs as MEOC analysis in Fig. 4.5, the data in the table appears to be too much complex to compare. The number of data is more than twice that of MEOC. Unlike the MEOC analysis, whether two ports are strongly coupled or not cannot be easily read from the admittance comparison. The coupling analysis is difficult to carry out, either. Moreover, because there is no normalization in the admittance analysis, the modal energy distribution of each port cannot be read clearly.

In this modal admittance comparison, for each mode, there are six Modal Mutual Admittance (MMA) and four Modal Self Admittance (MSA) that need to be considered. In fact, for a N-port antenna, there are N MMAs and  $\frac{(N)(N-1)}{2}$  MSAs to deal with for every mode simultaneously, while only N for the MEOC method.

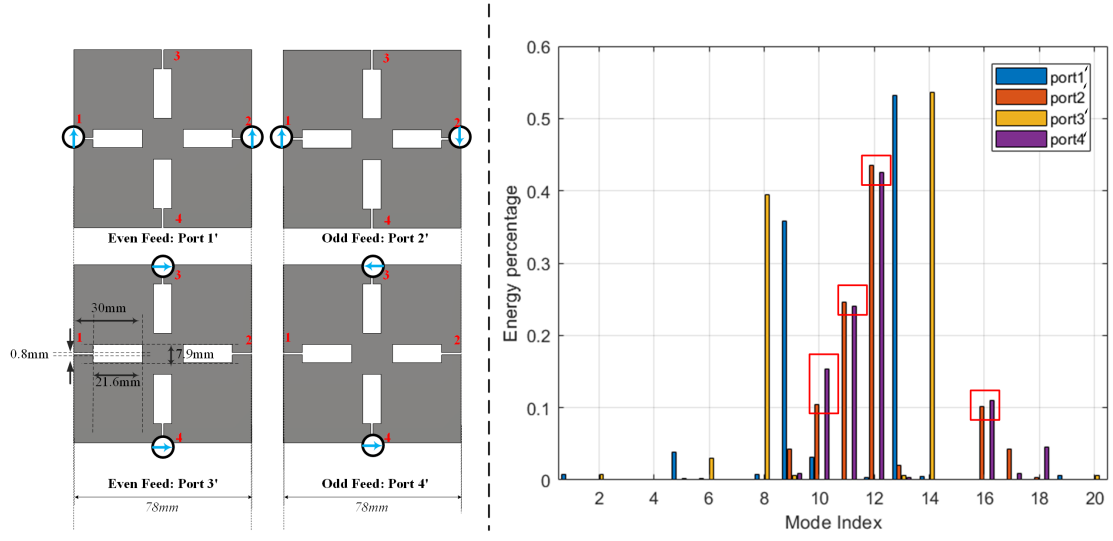


Figure 4.5: Left: Four feed schemes through four different ports  $1' \sim 4'$  for rectangular plates. The antenna ports are located at the end of each slot, which are named as port 1  $\sim$  4. Right: MEOC comparison among the four input ports at 4.5 GHz. The order of CMs is determined by the absolute values of their corresponding eigenvalues in ascending order. The comparison clearly shows that port 2 and 4 are strongly coupled and that they mainly coupled at Mode 10, 11, 12, and 16.

The reason why MEOC greatly simplifies the coupling analysis is that MEOC decomposes the coupled energy on each MMA to single modal energy on related ports, with the normalization of MSA. For example, in the square antenna case, the  $MMA_{1,4}$  is divided into two MEOC:  $M_1$  and  $M_4$ . The comparison on MSA is also omitted in MEOC method as MEOC hides the port impedance and focuses on field coupling.

To sum up, in the CMA for multiport antennas, the comparison of Fig. 4.5 and Table 4-B proves that using MEOC instead of the MA method is much easier, clearer, and more convenient.



## 4.5 Summary

In this chapter, a new method is introduced to evaluate the modal coupling and radiation of multiport antenna. Further derivation has been presented to enable the method to be adopted in the linear transformation of a feeding network. With examples of twin-dipole system and a four-port square antenna, the method is compared to previous work. The proposed method demonstrates its advantages by decomposing the mutual energy occupancy state of each mode, providing a clearer and simpler view of the radiation and mutual coupling of multiport antennas, especially with a higher port number.

In the next chapter, this method will further be exploited for its application. The analysis of the square antenna in this chapter will continue, and a high isolation multiport antenna will be designed and proposed.

## References

- [1] D. Manteuffel and R. Martens, “Compact multimode multielement antenna for indoor uwb massive mimo,” *IEEE Transactions on Antennas and Propagation*, vol. 64, no. 7, pp. 2689–2697, Mar. 2016.
- [2] D. Yang, H. Zeng, R. Chen, J. Qu, Y. Wen, and S. Liu, “Four port compact multimode patch antenna system for vehicular application,” in *2016 IEEE International Workshop on Electromagnetics: Applications and Student Innovation Competition (iWEM)*, pp. 1–3.
- [3] M. Bouezzeddine and W. L. Schroeder, “Design of a wideband, tunable four-port mimo antenna system with high isolation based on the theory of characteristic modes,” *IEEE Transactions on Antennas and Propagation*, vol. 64,

- no. 7, pp. 2679–2688, Mar. 2016.
- [4] M. H. Rabah, D. Seetharamdoo, and M. Berbineau, “Analysis of miniature metamaterial and magnetodielectric arbitrary-shaped patch antennas using characteristic modes: Evaluation of the  $q$  factor,” *IEEE Transactions on Antennas and Propagation*, vol. 64, no. 7, pp. 2719–2731, May 2016.
- [5] J. J. Adams and J. T. Bernhard, “Broadband equivalent circuit models for antenna impedances and fields using characteristic modes,” *IEEE Transactions on Antennas and Propagation*, vol. 61, no. 8, pp. 3985–3994, May 2013.
- [6] Q. Wu, W. Su, Z. Li, and D. Su, “Reduction in out-of-band antenna coupling using characteristic mode analysis,” *IEEE Transactions on Antennas and Propagation*, vol. 64, no. 7, pp. 2732–2742, July 2016.
- [7] B. Yang and J. J. Adams, “Systematic shape optimization of symmetric mimo antennas using characteristic modes,” *IEEE Transactions on Antennas and Propagation*, vol. 64, no. 7, pp. 2668–2678, Aug. 2016.
- [8] R. Harrington and J. Mautz, “Theory of characteristic modes for conducting bodies,” *IEEE Transactions on Antennas and Propagation*, vol. 19, no. 5, pp. 622–628, Sep. 1971.
- [9] S. N. Makarov, *Antenna and EM Modeling with MATLAB*. Hoboken, NJ, USA: Wiley-Interscience, 2002.
- [10] J. Molins-Benlliure, E. Antonino-Daviu, M. Cabedo-Fabrs, and M. Ferrando-Bataller, “Four-port wide-band cavity-backed antenna with isolating x-shaped block for sub-6 ghz 5g indoor base stations,” *IEEE Access*, vol. 9, pp. 80 535–80 545, 2021.
- [11] D. Zhang, Y. Chen, and S. Yang, “An in-band decoupling technique for base station antennas,” in *2021 IEEE International Workshop on Electromagnetics: Applications and Student Innovation Competition (iWEM)*, vol. volume1, 2021, pp. 1–3.

- [12] R. Kumar, R. K. Khokle, and R. R. Krishna, “A horizontally polarized rectangular stepped slot antenna for ultra wide bandwidth with boresight radiation patterns,” *IEEE Transactions on Antennas and Propagation*, vol. 62, no. 7, pp. 3501–3510, 2014.
- [13] W. Zhu, T. Yu, and N. Weimin, “Design of a high-gain wideband microstrip antenna with a stepped slot structure,” in *2013 Proceeding of the International Symposium on Antennas Propagation*, vol. 1, pp. 115–117.
- [14] S. K. Chaudhury, H. J. Chaloupka, and A. Ziroff, “Multiport antenna systems for mimo and diversity,” in *Proceeding of the 4th European Conference on Antennas and Propagation*, 2010, pp. 1–5.

Table 4-B: The real part of modal admittance of the first 20 modes of the square antenna

	Mode1	Mode2	Mode3	Mode4	Mode5
Y11	8.85E-05	9.64E-06	5.80E-10	8.78E-09	0.000412
Y12	1.73E-06	8.95E-08	-4.38E-09	-1.09E-08	-4.25E-05
Y13	3.42E-05	-2.88E-05	-4.65E-09	1.15E-08	-8.42E-05
Y14	-6.16E-07	6.74E-08	6.01E-10	-4.81E-09	-4.92E-06
Y22	3.40E-08	8.30E-10	3.31E-08	1.37E-08	4.39E-06
Y23	6.70E-07	-2.67E-07	3.51E-08	-1.44E-08	8.68E-06
<b>Y24</b>	-1.21E-08	6.25E-10	-4.53E-09	6.00E-09	5.07E-07
Y33	1.32E-05	8.60E-05	3.73E-08	1.52E-08	1.72E-05
Y34	-2.38E-07	-2.01E-07	-4.82E-09	-6.32E-09	1.00E-06
Y44	4.29E-09	4.71E-10	6.22E-10	2.64E-09	5.86E-08
	Mode6	Mode7	Mode8	Mode9	Mode10
Y11	1.57E-05	3.06E-08	8.88E-05	0.003893	0.000339
Y12	-3.42E-06	2.89E-07	-6.83E-06	0.000755	-0.00071
Y13	6.15E-07	-1.23E-07	2.40E-06	-0.00066	0.000779
Y22	7.46E-07	2.73E-06	5.25E-07	0.000146	0.001497
Y23	-1.57E-05	-4.61E-08	4.70E-05	1.04E-04	-0.00014
<b>Y24</b>	-1.34E-07	-1.16E-06	-1.84E-07	-0.00013	-0.00164
Y33	1.32E-05	7.79E-10	0.004209	7.35E-05	1.35E-05
Y34	-2.38E-07	1.96E-08	-1.65E-05	-9.02E-05	0.000156
Y44	4.29E-09	4.91E-07	6.46E-08	0.000111	0.001789
	Mode11	Mode12	Mode13	Mode14	Mode15
Y11	1.60E-06	3.23E-05	0.005784	5.85E-05	1.67E-06
Y12	-6.93E-05	-0.00042	0.0002	2.42E-06	2.31E-07
Y13	3.75E-07	3.71E-06	-5.93E-04	0.000579	-4.11E-07
Y14	-6.70E-05	-0.0004	0.000501	1.47E-05	-9.62E-08
Y22	0.003008	0.005437	6.92E-06	1.00E-07	3.19E-08
Y23	-1.63E-05	-4.81E-05	-2.05E-05	2.40E-05	-5.69E-08
<b>Y24</b>	0.002907	0.005201	1.73E-05	6.10E-07	-1.33E-08
Y33	8.81E-08	4.25E-07	6.08E-05	0.005735	1.01E-07
Y34	-1.57E-05	-4.60E-05	-5.14E-05	0.000146	2.37E-08
Y44	0.002809	0.004976	4.34E-05	3.71E-06	5.55E-09
	Mode16	Mode17	Mode18	Mode19	Mode20
Y11	1.98E-06	7.87E-07	4.24E-07	6.57E-05	9.54E-09
Y12	4.89E-05	2.02E-05	4.32E-06	-1.51E-06	-4.38E-09
Y13	5.56E-07	1.25E-07	1.11E-07	-7.62E-07	7.83E-07
Y14	-5.06E-05	9.33E-06	-1.50E-05	-9.33E-07	3.98E-09
Y22	0.001212	0.000519	4.40E-05	3.46E-08	2.01E-09
Y23	1.38E-05	3.20E-06	1.13E-06	1.75E-08	-3.59E-07
<b>Y24</b>	-0.00125	0.00024	-1.53E-04	2.14E-08	-1.83E-09
Y33	1.56E-07	1.98E-08	2.91E-08	8.85E-09	6.42E-05
Y34	-1.42E-05	1.48E-06	-3.93E-06	1.08E-08	3.27E-07
Y44	0.001296	1.11E-04	0.000532	1.33E-08	1.66E-09

## Chapter 5

# MEOC Application on the Design of Multiport Antenna

### 5.1 Introduction

In the last chapter, the main focus of the research is to compare the proposed MEOC method with existing parameters on multiport antenna application. In this chapter, the analysis of the four-port square antenna from the previous chapter will continue, and the usage of MEOC will be further explored. As a result, a four-port antenna with a broader band than previous work will be presented. Working at a broadband of  $3 \sim 6$  GHz, each port of antenna excites more than one CM, yet high isolation among all ports is realized. It is worth mentioning that this work differs from other TCM studies [1–5], where the antennas are initially designed with the guidance of TCM by exciting fewer independent CMs. The research in this chapter expands the study of MEOC in multiport antennas to a more general scenario, especially when antennas are predetermined due to production demand.

## 5.2 Application Example with MEOC

### 5.2.1 MEOC Analysis for a Square Plate

In the discussion of the square antenna in the last chapter, it was predicted that input port 2' and 4' of the four-port antenna are very likely to be coupled. A closer look for the CMs on radiation will be given below.

Firstly, MEOC analysis based on (4.16) in previous chapter at 4.5 GHz is redrawn in Fig. 5.2. The order of CMs is determined by the absolute values of their corresponding eigenvalues in ascending order.

It is mentioned that in [6], at medium frequency ( $\lambda < \text{antenna size}$ ), higher order CMs have a better chance for radiating than at low frequency ( $\lambda \geq 2 \times \text{antenna size}$ ). Fig. 5.2 reflects a similar result and shows that at 4.5 GHz ( $\lambda = 0.85 \times \text{antenna size}$ ), higher order mode, Mode 12 for example, involves much more in the radiation than lower order mode, e.q., Mode 1  $\sim$  4.

In last chapter, it has been discussed that input port 1' and 3' independently excite different modes and have few common modes with other ports. Hence, high isolation between the two ports and others is predicted. This can be verified by the scattering parameter in Fig. 5.4 (a) (solid lines). Fig. 5.2 indicates that when input port 1' and 3' are fed simultaneously, they are barely coupled at any mode. This is the MEOC-based depiction for the commonly high isolation of orthogonal-polarization antennas. On the other hand, in Fig. 5.2, the far-fields radiated by port 2' and 4' are mainly composed of their common Mode 10, 11 and 12, which take up more than 90% of all the total radiate energy. It indicates high coupling between port 2' and 4', which matches well to the simulation results in Fig. 5.4

(a) (solid lines). Moreover, on these coupling modes, port 2' and 4' consume equal electromagnetic energy.

In order to improve isolation among port 2' and 4', the symmetric energy distribution of port 2' and 4' needs be to separated. With least influence on the performance of port 1' and 3', the shape of the square plate is modified to a hexagonal plate with same length, which changes the excitation of port 3' and 4' with two more ports, as shown Fig. 5.1 (b). Excitation of port 1' and 2' stays the same.

The matrix transformation for the hexagonal plate is similar to that of the rectangular plate. The relationship between input ports 1' ~ 4' and antenna ports 1 ~ 6 is,

$$\begin{aligned} [Y'] &= T[Y]T^H \\ [\widetilde{M}'] &= \{[\mathbf{p}'I]^{-1}T[\mathbf{p}I]\}[\widetilde{M}]\{[\mathbf{p}'I]^{-1}T[\mathbf{p}I]\}^H \end{aligned} \quad (5.1)$$

where,

$$\begin{aligned} T &= \begin{bmatrix} I_{2 \times 2} & \\ & V_2 \end{bmatrix} \begin{bmatrix} I_{2 \times 2} & \\ & D_{2 \times 4} \end{bmatrix} \begin{bmatrix} V_2 & \\ & I_{4 \times 4} \end{bmatrix}, \\ D_{2 \times 4} &= \frac{1}{\sqrt{2}} \begin{bmatrix} 1 & 1 & & \\ & & & \\ & & 1 & 1 \\ & & & \end{bmatrix}, \\ V_2 &= \frac{1}{\sqrt{2}} \begin{bmatrix} 1 & 1 \\ 1 & -1 \end{bmatrix}. \end{aligned} \quad (5.2)$$

The MEOC research for the new shape at 4.5 GHz is shown in Fig. 5.3 (a). In Fig. 5.3 (a), each port excites individual modes after the modification, which results in low coupling over the entire operating frequency band as provided in Fig. 5.4 (a). On the other hand, it is observed from Fig 5.4 (b) that every port except port 3' is well-matched over 3 ~ 6 GHz. Therefore, the next step is to tune

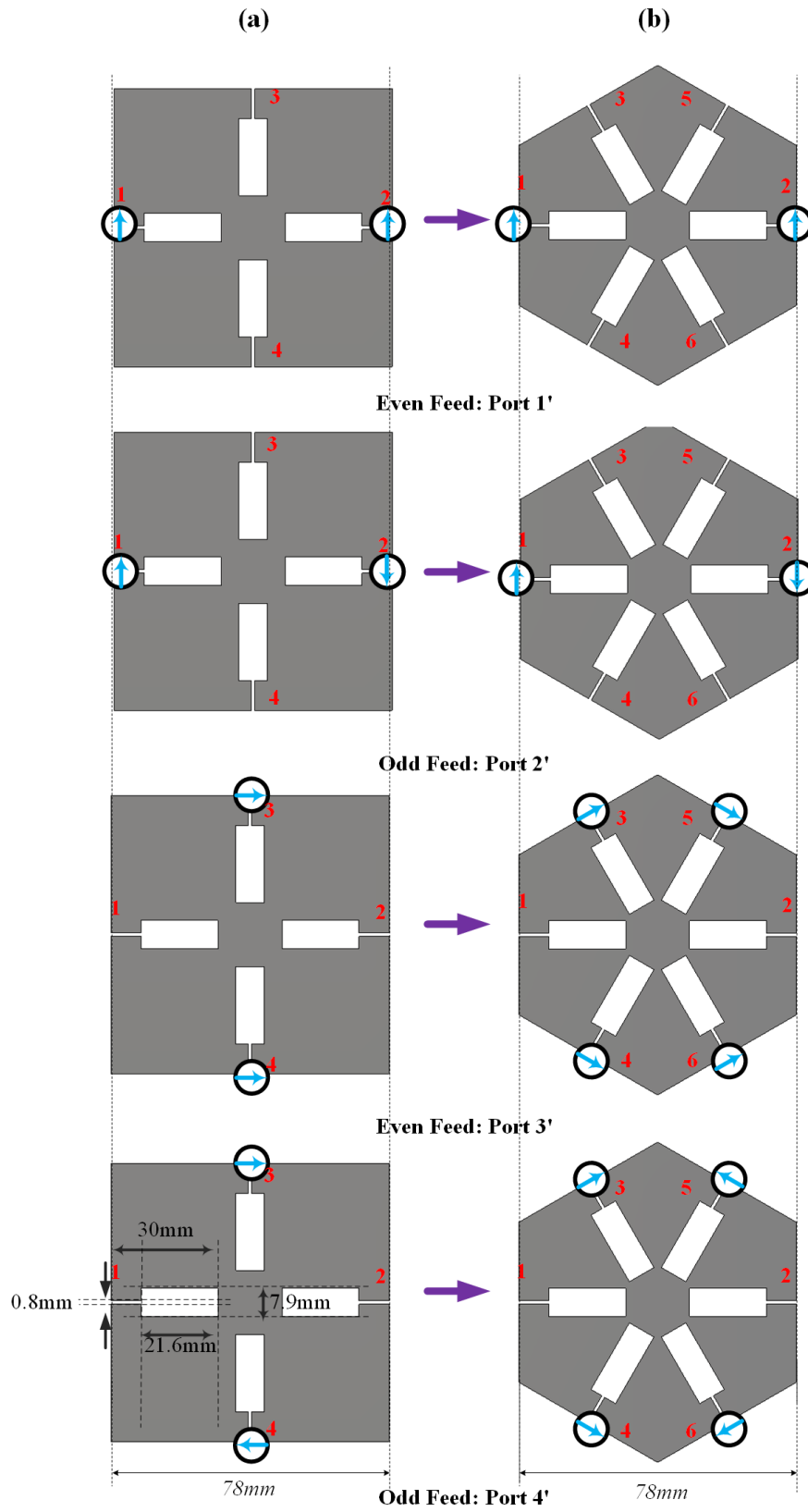


Figure 5.1: Four feed schemes through four different ports  $1' \sim 4'$  for rectangular plate and hexagonal plate. The antenna ports are located at the end of each slot, which are named as port  $1 \sim 4$  (rectangle) or port  $1 \sim 6$  (hexagon).



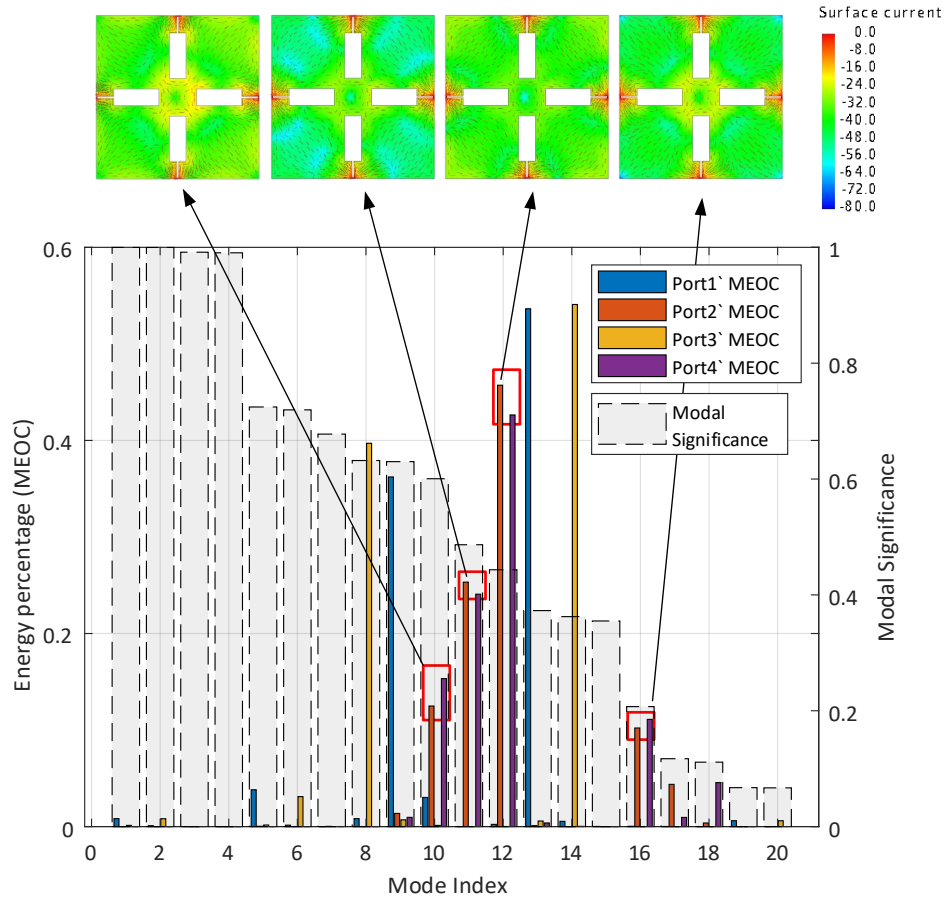


Figure 5.2: MEOC analysis of rectangular plate at 4.5 GHz. The order and naming rules of CMs is determined by the absolute values of their corresponding eigenvalues in ascending order. It is shown that radiation by port 1' is dominated by Mode 4, 9 and 13. For port 2', the dominant modes are Mode 9 ~ 12 and 16, 17. For port 3', they are 6, 8 and 14. And finally, for port 4', they are 10 ~ 12 and 16, 18. The surface current for the shared dominant modes of port 2 and 4 are also illustrated.

port 3' for a better impedance matching.

### 5.2.2 Impedance Matching for Hexagonal Plate

From Fig. 5.3 (a), it is noticed that the dominant modes that excited by port 3' are Mode 3, 4 and 7. Their corresponding surface current (dB) and far-field

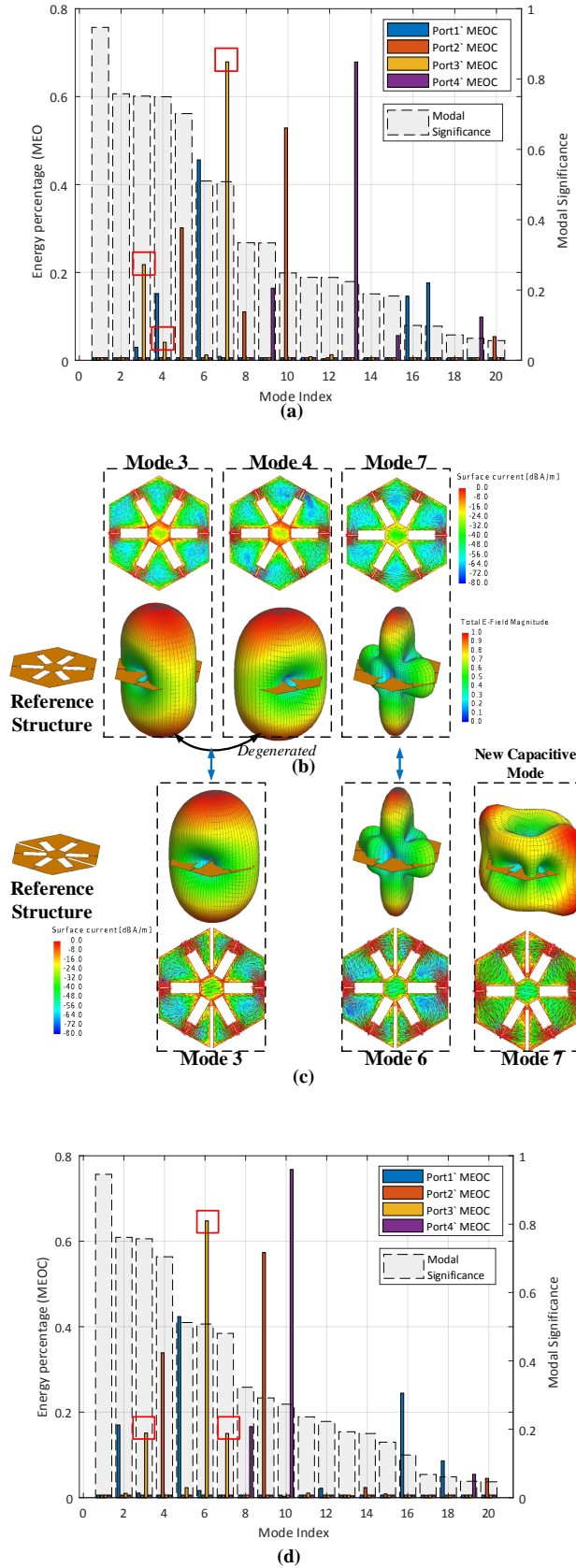


Figure 5.3: MEOC for hexagonal plate w/ and w/o extra slots. (a) MEOC and MS for the original plate at 4.5 GHz (b) dominant modes for port 3', (c) dominant modes after adding slots, (d) MEOC and MSs for the modified plate. The size for the extra slot is 32 mm and width 3 mm.

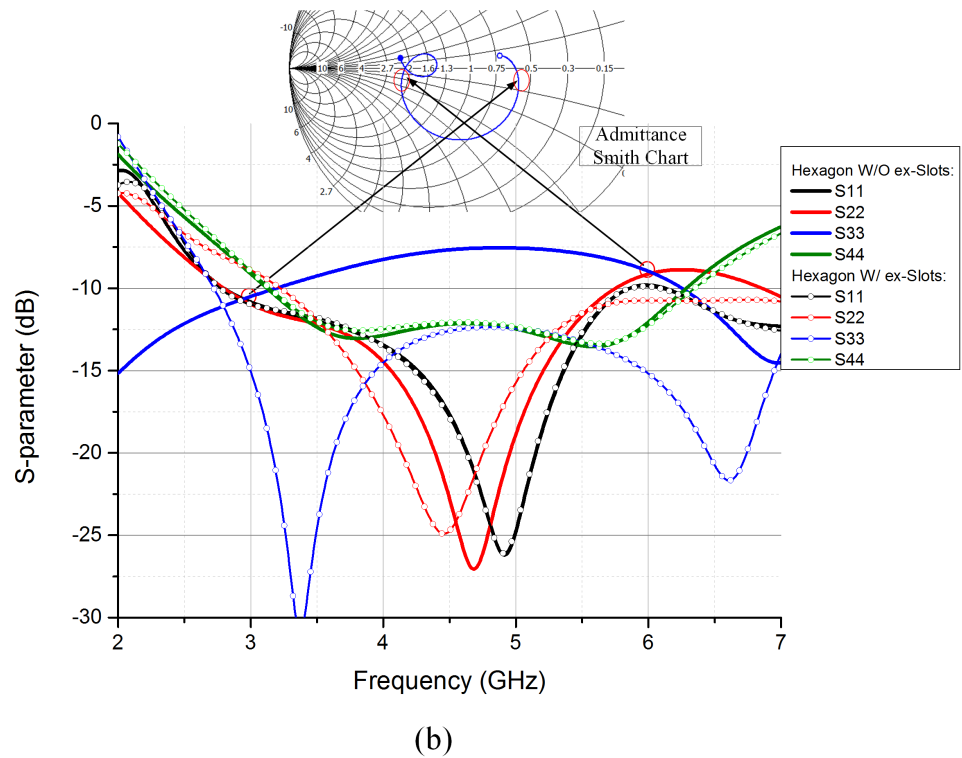
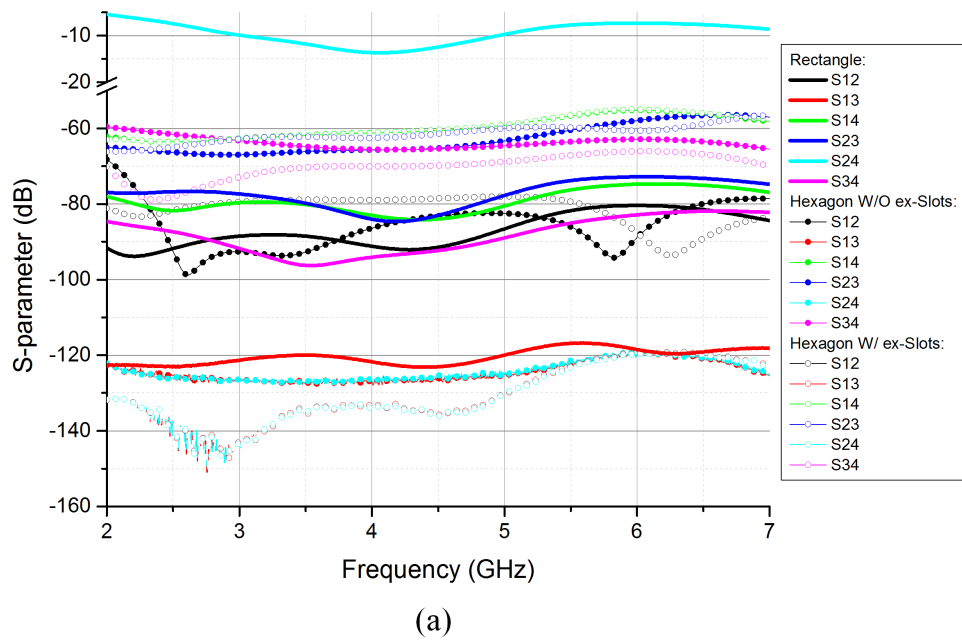


Figure 5.4: Reflection and transmitting coefficients of three mentioned structure (rectangular plate, hexagonal plate and hexagonal plate with extra slots). (a) Coupling among four ports for three structures. (b) Self reflection coefficients for all ports on hexagonal plates.

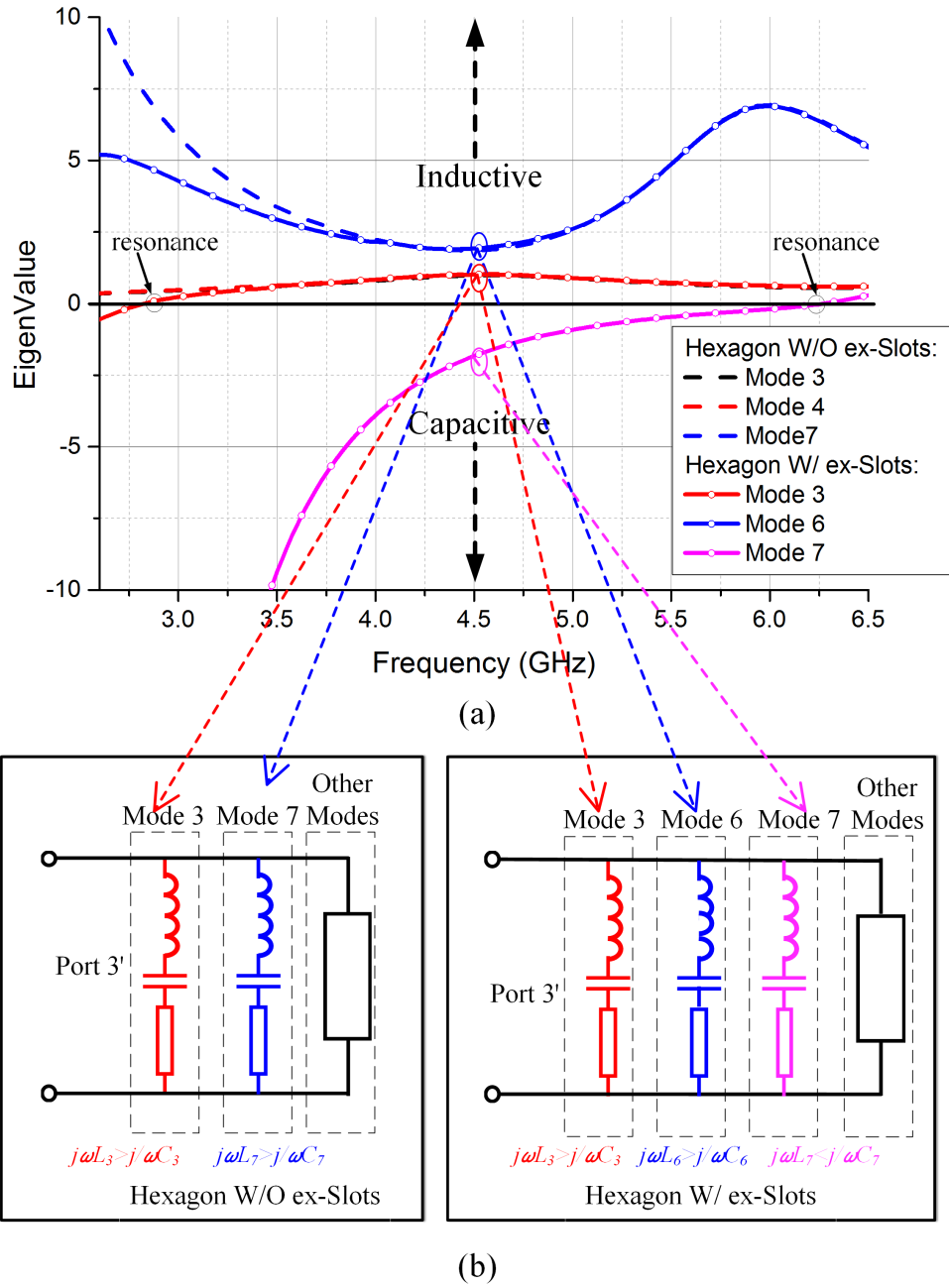


Figure 5.5: Comparison of dominant modes between two hexagonal plates with (W/) or without (W/O) extra slots. (a) the eigenvalue of port 3's dominant modes at 2.6 ~ 6.5 GHz of two hexagonal plates (b) the equivalent circuit for two hexagonal plates with reference to port 3'.

are illustrated in Fig. 5.3 (b). It is shown that Mode 3 and 4 are degenerated modes, which occurs due to the structure symmetry and they behave in a similar

manner over frequency band. The wide-band tracking of their eigenvalues in Fig 5.5 (dashed lines) also proves that. In Fig. 5.3 (b), radiations of Mode 3 and 4 are similar to a wide dipole at high frequency. Mode 7 radiates a pattern with its main lobe and side lobes in the diagonal plane. The wide-band tracking of these modes's eigenvalues in Fig 5.5 (dashed lines) reveals that in the operating frequency band  $3 \sim 6$  GHz, Mode 3 and 4 have already passed their resonance frequencies and both of them have positive eigenvalues, which, according to (4.3), indicates that they store magnetic energy over the operating frequency band. In addition, Mode 7 does not resonate at all around the operating frequency and it also has a positive eigenvalue. Therefore, all the dominant modes store a large amount of magnetic energy within the frequency band, which makes the impedance matching at port 3' difficult to be implemented. This fact conforms to the inductive behaviour of port 3' illustrated in the admittance smith chart in Fig. 5.4 (b).

Hence, a capacitive component is added to the structure to improve the matching of port 3'. Therefore, two slots are cut along the long diagonal of the hexagonal plate, as shown in Fig. 5.3 (c). These slots introduce one new capacitive Mode 7 dominating port 3', which has far-field main lobes symmetric in the diagonal plane, as illustrated in Fig. 5.3 (c) and (d). Besides, there are no degenerated modes dominating port 3' but only one Mode 3 radiating a 'dipole-like' pattern after modification. This is because that the new slots restrict the number of hexagon's symmetry axis at diagonal to only 1, which makes only one mode in the degenerated pair reactive with reference to port 3'. The original Mode 7 now shifts to Mode 6. Its far-field pattern barely changes at 4.5 GHz, as the new slots are located at the current weak area of the original Mode 7.

The eigenvalue tracking for new dominant modes is shown in Fig. 5.5 (a) (solid lines with bubbles). It tells that the new Mode 7 resonates at 6.3 GHz and behaves

inductively at  $3 \sim 6$  GHz. Eigenvalues of new Mode 3 and 6 barely change compared to those of the previous structure and have positive values in the operating band. Mode 3 is a 'dipole-like' mode, adding slots is equivalent to shorten the electrical length of the wide dipole. Therefore its resonance frequency rises to 2.8 GHz.

Mode 3 and 4 of the original hexagon and Mode 3 of the modified one have passed their resonance frequencies and behave inductively with positive eigenvalue. In a schematic view, Mode 3 and 4 can be equivalent to a first-order series RLC sub-circuit in which  $j\omega L > j/(\omega C)$  in the frequency band. Mode 7 of the original hexagon and Mode 6 of the modified one does not resonate at all in the band and have high positive values. Therefore, they are also equivalent to a sub-circuit in which  $j\omega L > j/(\omega C)$ . As for the new Mode 7 after adding slots, which resonates at 6.3 GHz and has negative eigenvalues in the band, it is equivalent to a sub-circuit whose  $j\omega L < j/(\omega C)$ .

Equivalent circuits above are then assigned into paralleled circuit form as shown in Fig. 5.5 (b) with their corresponding parameters at 4.5 GHz are listed in Table 5-A. Values of the circuit components are obtained from:

$$\begin{aligned}
 & R_n \sqrt{\frac{L_n}{C}} \\
 = & Q = \frac{\omega}{2} \sqrt{\left(\frac{2I'_{port}}{I_{port}}\right)^2 + \left(\omega'_n - 2\frac{\omega_n I'_{port}}{I_{port}} + \frac{|\omega_n|}{\omega}\right)^2}, [6] \\
 & R_n + j\omega L_n - j\frac{1}{\omega C_n} = MSA_n = \frac{I_{port}^2}{1 + j\omega_n}
 \end{aligned} \tag{5.3}$$

where  $R, L, C$  are the equivalent circuit components.  $Q$  is the Quality factor.  $I'_{port}$  and  $\omega'_n$  are derivatives of port current and eigenvalue at 4.5 GHz. As the equivalent circuit is not the main topic of the work, other details for the calculation will

Table 5-A: Parameters for the equivalent circuits in Fig. 5.5 (b) (4.5 GHz)

Parameter (W/O ex-Slots)	$R_3$	$\omega L_3$	$1/(\omega C_3)$	$R_7$	$\omega L_7$	$1/(\omega C_3)$
Value ( $\Omega$ )	448.6	4359.4	3965.7	65.8	537.4	425.9
Parameter (W/ ex-Slots)	$R_3$	$\omega L_3$	$1/(\omega C_3)$	$R_6$	$\omega L_6$	$1/(\omega C_6)$
Value ( $\Omega$ )	527.6	8901.0	8445.8	55.3	576.2	482.4
Parameter (W/ ex-Slots)	$R_7$	$\omega L_7$	$1/(\omega C_7)$			
Value ( $\Omega$ )	213.6	693.9	1083.8			

not discussed further. Those resistors in each sub-circuit represent those modes dominate the radiation. For other modes which do not have much contribution in the radiation, their equivalent resistances are large enough to be omitted in the parallel circuit. Thus their reactance to frequency can be over-all equivalent as a pure reactance.

Before adding slots on the hexagon, because of the inductive behavior of Mode 3, 4 and 7, the imaginary part of port 3' input admittance is too large to be matched. After cutting slots, Mode 7 appears and acts as a strong capacitive mode in the band. It compensates the imaginary part of the input admittance and helps match the impedance. The resonant frequency of the new capacitive Mode 7 (resonating at 6.3 GHz) and the original Mode 3 (resonating at 2.85 GHz) create two resonates, as shown in Fig. 5.4 (b) (blue lines).

Fig. 5.5 indicates such a fact that along with the frequency increase, although one mode has already passed its resonance, or it has yet to resonant, it still has much chance to radiate, e.g., the Mode 3 and 7 in the final structure. Actually, the eigenvalue of one mode could fluctuate in a low value range before or after passing its resonate frequency, and it still makes this mode possible to participate much in radiation. Nevertheless, if one mode does not resonate at all in the frequency

band, it does not mean that it has no contribution to the radiation. Take the Mode 6 (Fig. 5.5, blue line) of the hexagonal plate with extra-slot as an example. It does not resonate at all in or out of the band, yet still plays an important role in the radiation. In general, eigenvalue alone does not determine the radiation ability of one mode with respect to the port. MEOC, on the other hand, describe not only how much one mode participates in the radiation, but also how it contributes to the mutual coupling.

## 5.3 Antenna Realization and Measurement

### 5.3.1 Feeding Network Design

In order to feed the hexagonal antenna, a feeding network is required to fulfill the desired feeding scheme. The feeding network needs to be planar, low-lossy and easy to combine with balun structures. As a result, a set of 5-layer feeding network is designed as shown in Fig. 5.6 with corresponding parameters listed in Table 5-B. This feeding network serves as a  $4 \times 6$  transformation matrix between feeding ports and hexagon ports. The design is based on a *Rogers RO4003* PCB board with  $\epsilon_r = 3.38$  and thickness = 0.813 mm.

Port 1 and port 2 are sum ( $\Sigma$ ) and difference ( $\Delta$ ) ports in a  $180^\circ$  hybrid, respectively. This  $180^\circ$  hybrid origins from the coupler in [7], which consists of three conductor layers with two layers of dielectrics. Two input ports are on different sides of the ground. Bottom and top microstrip couple each other via an elliptical-shaped slot in the ground. This microstrip-slot-microstrip transition leads to an Ultra-Wide-Band (UWB) transmission characteristic. To compensate another  $90^\circ$  degree difference, the UWB phase shift in [8] is utilized to complete



Table 5-B: Parameters for feeding network in Fig. 5.6

Parameter	$l_1$	$l_2$	$l_3$	$w_1$	$w_2$	$w_3$	$w_0$
Value (mm)	5.2	8.2	9.4	0.7	0.93	1.4	1.8
Parameter	$D_1$	$D_2$	$D_3$	$w_s$	$l_s$	$l_{s1}$	$l_{s2}$
Value (mm)	5.1	3.32	5.4	3.3	21	14.2	12.9
Parameter	$l_{s3}$	$l_m$	$w_m$	L	$R_1$	$R_2$	$R_3$
Value (mm)	7	8.9	3.18	150	98	123.9	341

the  $180^\circ$  hybrid and maintain a constant phase shift over wide band. The phase shifter makes use of a T-shaped open end stub load, exhibiting a better bandwidth than conventional  $90^\circ$  phase shifter. The detailed theoretical analysis for the  $180^\circ$  hybrid is skipped for the consideration of concision. The reflection performance and transmitting phase difference can be seen in Fig. 5.7 and Fig. 5.8. It is verified in Fig. 5.8 that the phase difference for all ports is stabilized at  $0^\circ \pm 20^\circ$  (for  $\Sigma$  ports) or  $180^\circ \pm 20^\circ$  (for  $\Delta$  ports) at  $2.5 \sim 6.5$  GHz. Similar hybrid has also been constructed for port 3 and 4, excepting for that a pair of three-section Wilkinson dividers cascades at each end of the  $180^\circ$  hybrid to feed equally and maintain isolation.

It should be noticed that the original hybrid in [7] has its input and output ports on different sides of the ground plane. In this work, in order to adapt and solid to the Balun structure on the top of feeding network, two via holes are used to make sure the end strip of the whole feeding network is on the topside of ground.

### 5.3.2 Final Combination

The final combination of the whole structure is shown in Fig. 5.11. From bottom to top, there are three main components, a five-layer feeding network board, six

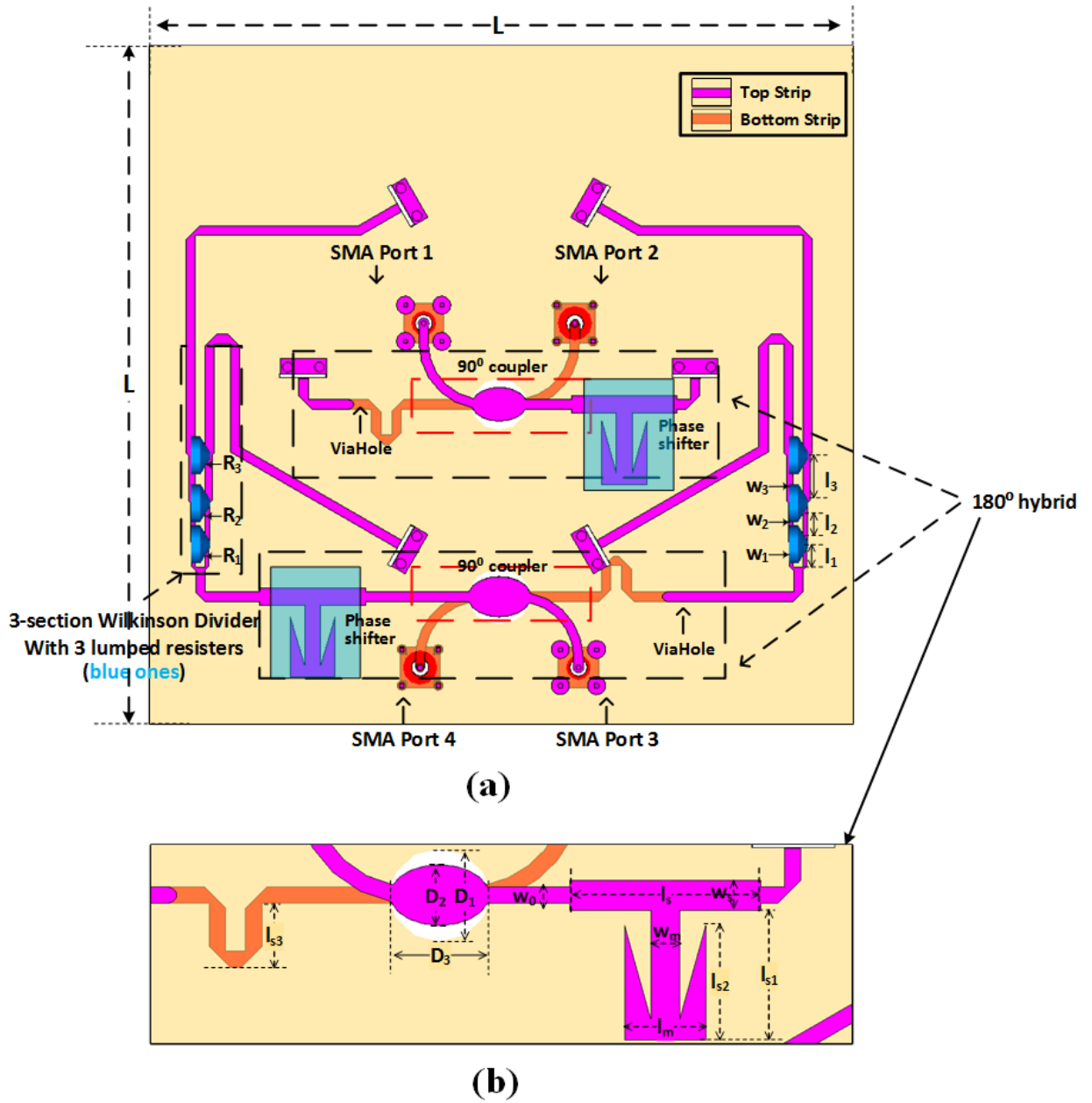


Figure 5.6: The feeding network with its performance. (a) The top view of feeding network. (b) The detail of the 180° hybrid. The feeding network has four input ports with SMA connector. Its ends connect to six Balun structures which are vertical to ground. The corresponding parameters are listed in Table 5-B.

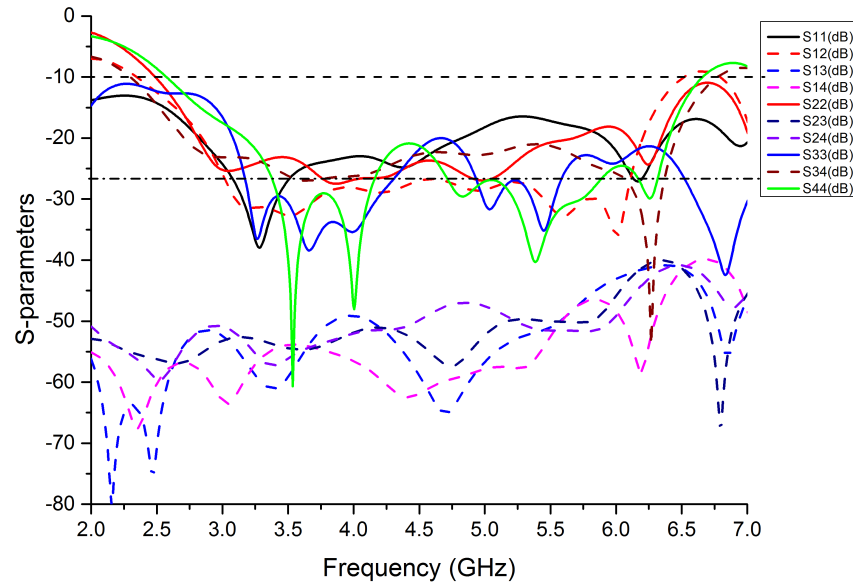


Figure 5.7: Simulation performance of the feeding network

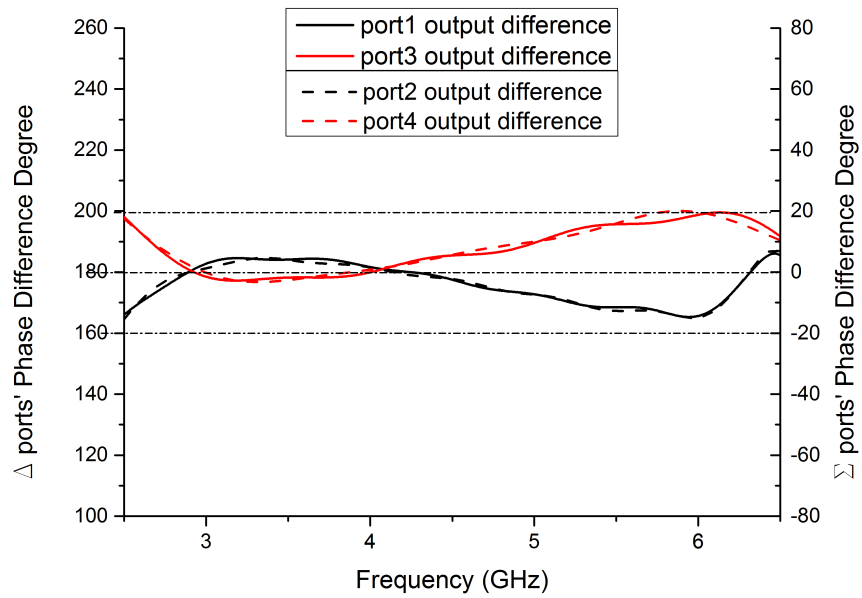


Figure 5.8: Phase responses of the feeding network

tapered balun structures in the vertical position, and the antenna board on the top. The feeding network is fed through four SMA connectors on the bottom side

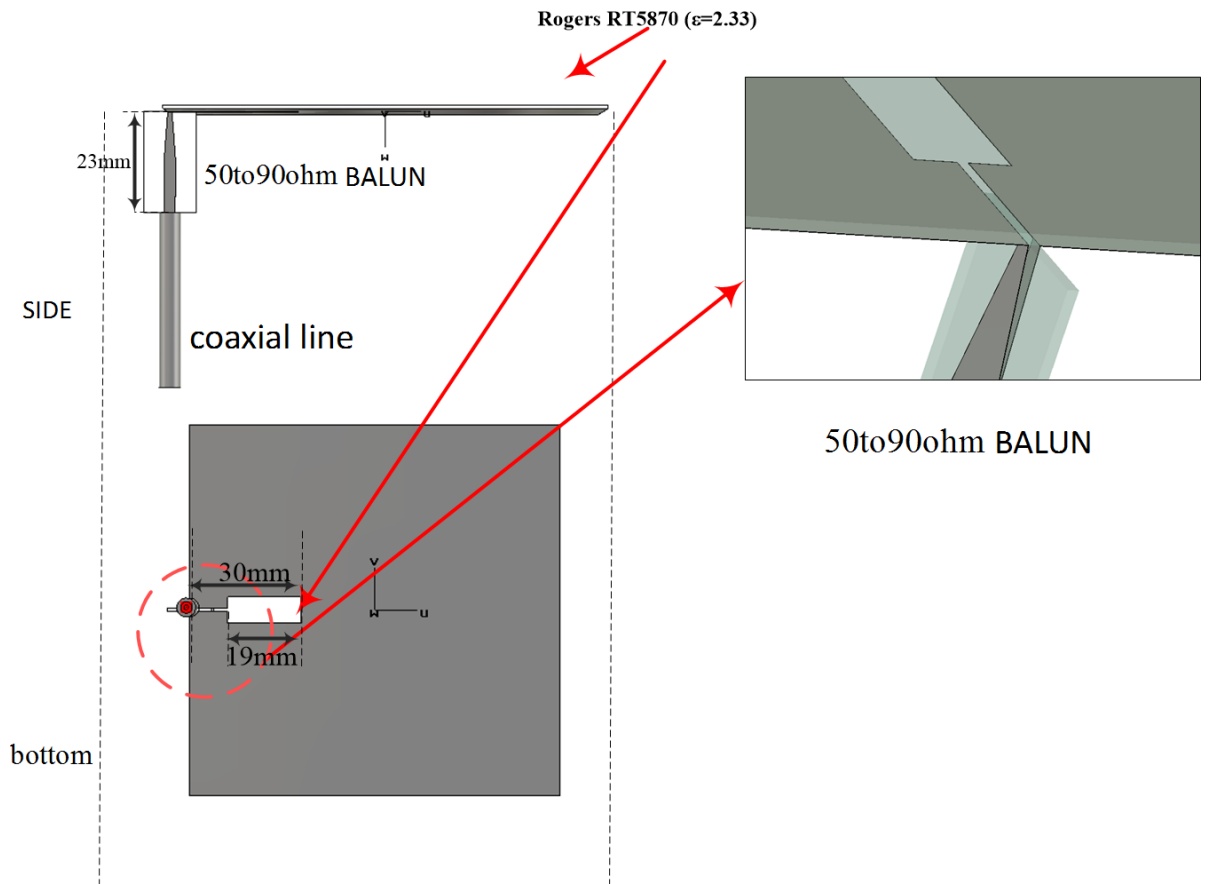


Figure 5.9: The Balun design and its configuration. It transforms the impedance from the antenna slots to the standard 50  $\Omega$ .

of the feeding network board. This board is a five-layer structure, with microstrip traces on both sides (Layer 1 and Layer 2) and ground (Layer 3) in the center layer. Details of the feeding network can be found in previous section. Six Balun structures connect the feeding network and the antenna board. The details for the Balun and its connection to antenna and feeding network is shown in Fig. 5.9. The Balun structure is a one-layer microstrip designed with *Rogers RT5870* Laminates with  $\epsilon_r = 2.33$  and thickness = 0.508 mm. The taper structure on Balun transform the high impedance (90  $\Omega$ ) on the end of the antenna slots to the feeding network ports, which are normalized to 50  $\Omega$ . The Balun structure behave as a smooth impedance converter and provide balanced feed to the antenna. A simulation

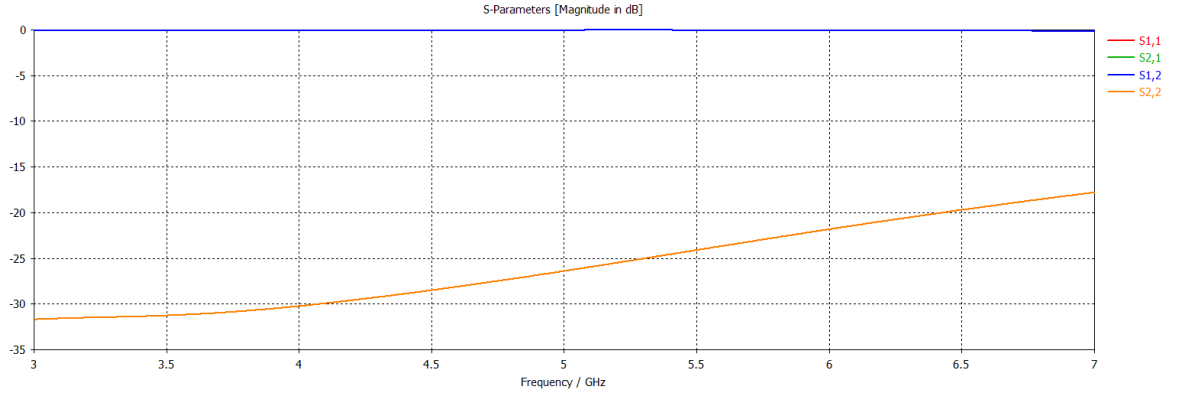


Figure 5.10: The final combination of antenna, balun and feeding network. (a) exploded view of the design (b) perspective view and back view. The antenna is fed through four SMA connectors on the bottom side of the ground.  $h1 = 0.813 \text{ mm}$ ,  $h2 = 0.518 \text{ mm}$  and  $H = 23 \text{ mm}$

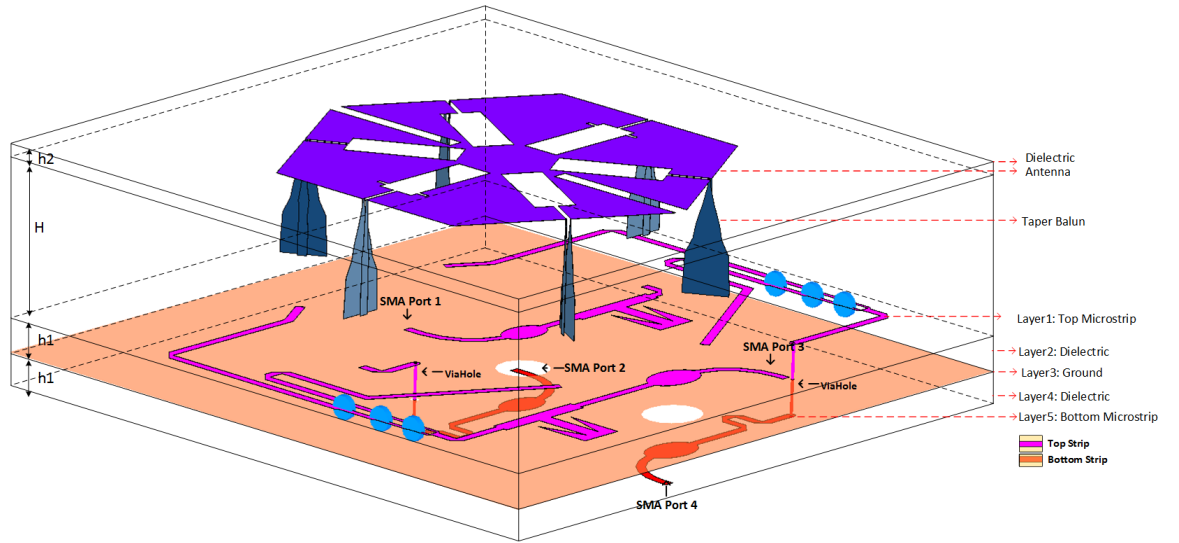


Figure 5.11: The simulation inserting loss of the related Balun structure. For the two-port system, the result is satisfying.

result of the inserting loss to validate the design is drawn in Fig. 5.10. The balun structures support the entire design like pillars.

Both the balun structure and feeding network utilize *Rogers RO4003* PCB board with  $\epsilon_r = 3.38$  and thickness =  $0.813 \text{ mm}$ . The antenna board uses

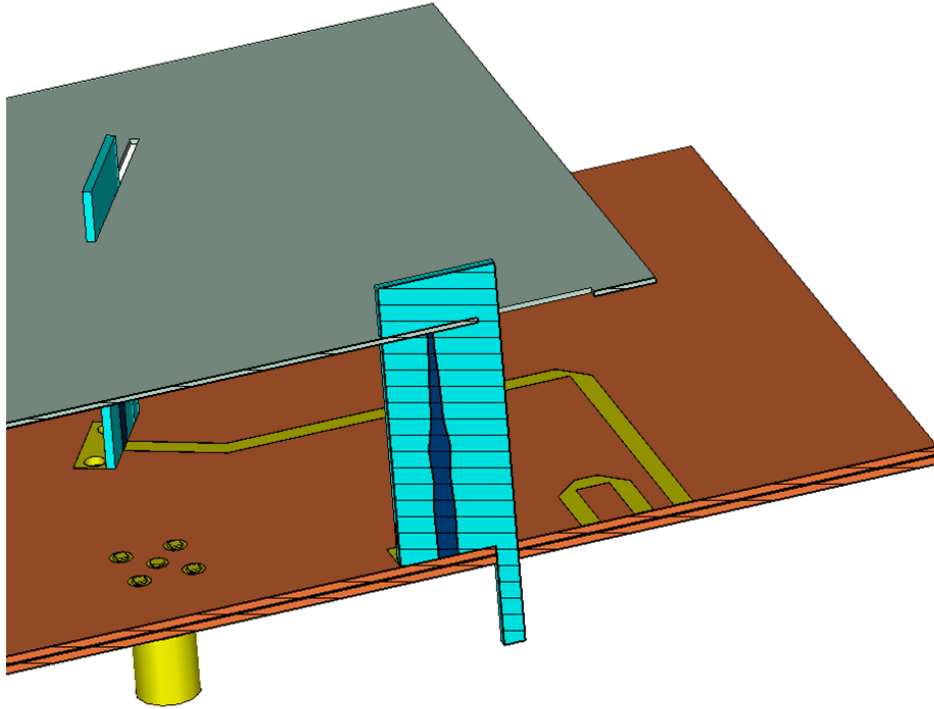


Figure 5.12: The transversal cut of the combination of antenna, Balun and feeding network layers. The substrate of the Balun is extended, creating slots of the same width as the antenna plate, allowing the new substrate slots to interlock with the antenna plates. This design makes the whole structure fixed stable.

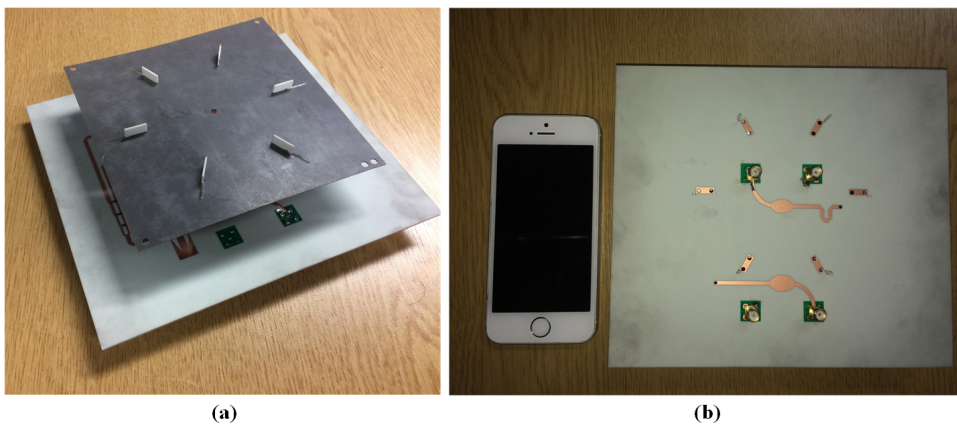


Figure 5.13: The prototype of proposed antenna (a) Perspective view. (b) Back view.

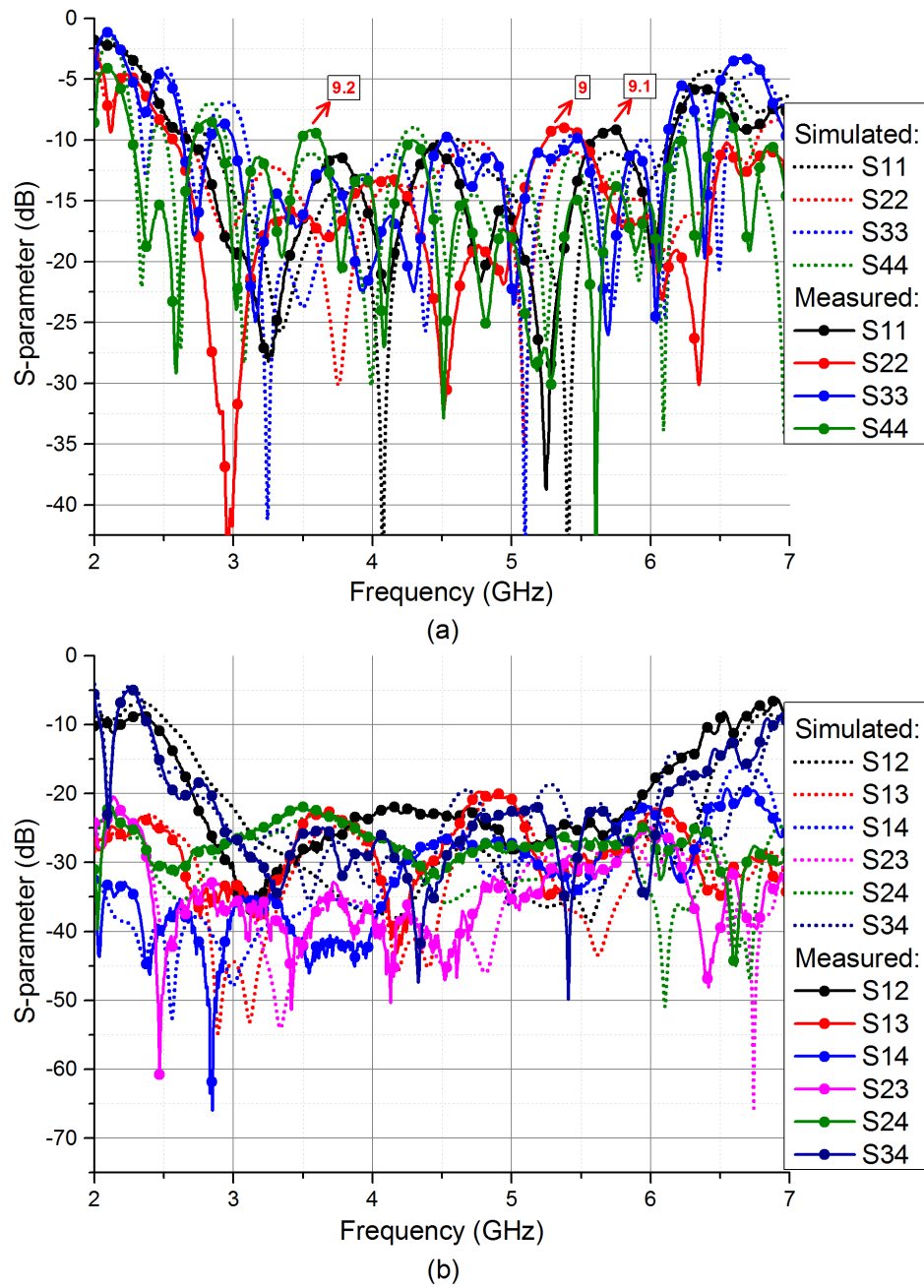


Figure 5.14: The scattering parameters of the antenna. It works well at 3~6 GHz, with coupling ( $S_{21}$ ) lower than -20 dB. (a) port reflection (b) isolation among ports.

*RogersRT5870* Laminates with  $\epsilon_r = 2.33$  and thickness = 0.508 mm.

### 5.3.3 Simulated and Measured Results

As described in the last section, all parts of the proposed antenna is fabricated and combined, as shown in Fig. 5.11. To make sure each component being well-fixed in the right position, slots have been cut in the substrates of antenna and feeding network boards separately, and corresponding shape is added on the Balun's substrate to make these three parts clinching together. The transversal cut of the combining section is shown in the Fig. 5.12. This minor modification will not influence the final performance as all those new slots are only cut in the substrate away from conductor. This design makes interlock among three layers and gives structural stability to the whole antenna, which is shown in Fig. 5.13.

The prototype is then measured with a four-port network analyser and in a microwave chamber. The corresponding scattering parameters are illustrated in Fig. 5.14. As shown in Fig. 5.14, reflection coefficients of all channels are below  $-10$  dB across  $3 \sim 6$  GHz, except for a few discrete frequencies having a maximum  $-9$  dB value in measurement. The proposed structure achieves a fractional impedance bandwidth of 66.7%. Both the simulated and measured port-to-port isolation are better than  $-20$  dB over the entire frequency band. The measurement results match well with simulations, though there are slight frequency shifts on some ports, which is likely to be caused by the soldering errors of the SMA connectors. In Fig. 5.15 and Fig. 5.16, the simulated and measured radiation patterns and realized gains of all ports are also compared. Effects of cables and unavoidable scattering in the chamber could be the source of minor discrepancies between measurement and simulation results, and gains of all ports are higher than 6 dBi.



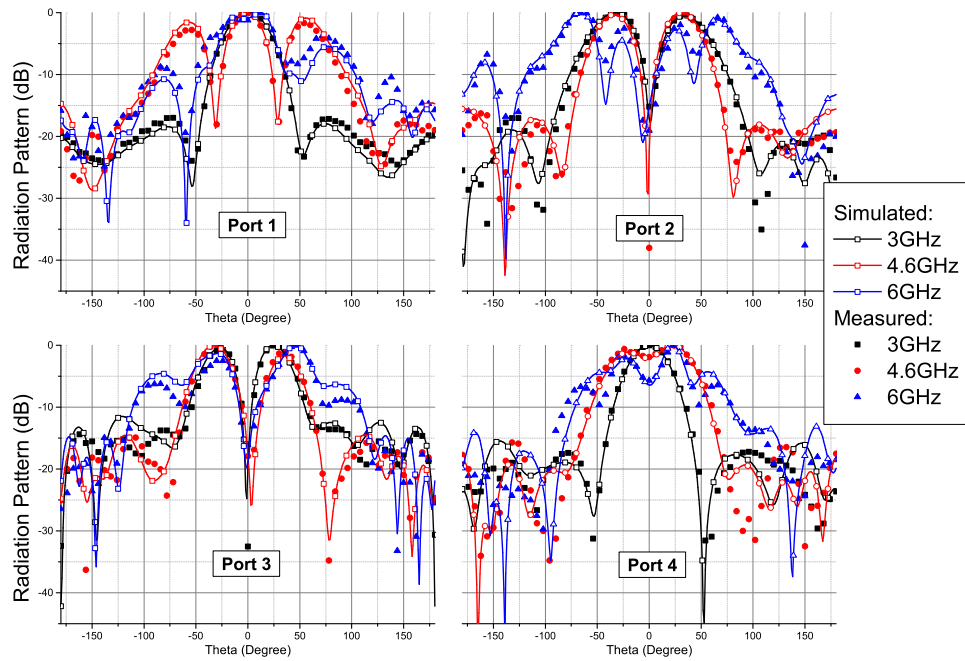


Figure 5.15: Far-field pattern of all four ports at three frequencies (3 GHz, 4.6 GHz, and 6 GHz) at y-z plane

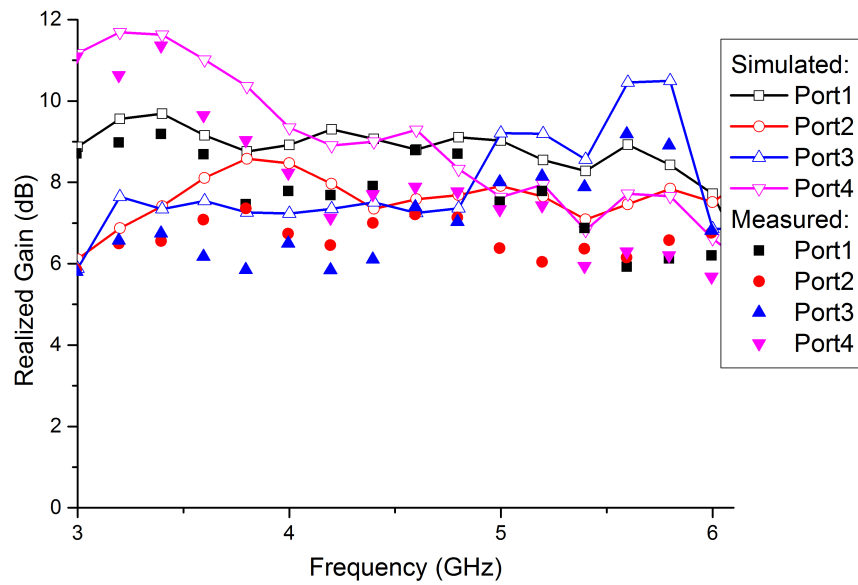


Figure 5.16: Realized Gain of all ports at 3 ~ 6 GHz

Table 5-C: Parameters for feeding network in Fig. 5.6

Parameter	$l_1$	$l_2$	$l_3$	$w_1$	$w_2$	$w_3$	$w_0$
Value (mm)	5.2	8.2	9.4	0.7	0.93	1.4	1.8
Parameter	$D_1$	$D_2$	$D_3$	$w_s$	$l_s$	$l_{s1}$	$l_{s2}$
Value (mm)	5.1	3.32	5.4	3.3	21	14.2	12.9
Parameter	$l_{s3}$	$l_m$	$w_m$	L	$R_1$	$R_2$	$R_3$
Value (mm)	7	8.9	3.18	150	98	123.9	341

## 5.4 Summary

In this chapter, MEOC analysis method continues to be used to study isolation for multiport antenna. It is illustrated that MEOC is able to simultaneously consider both radiation and coupling, thus could be a suitable and convenient tool for multiport antenna design. A hexagonal wide-band antenna is proposed as an example. The antenna uses multiport on a single radiator, which provides a broad-band (relative bandwidth 66.7%) performance for four ports within a compact structure. It is shown that the isolation of this antenna is well enough in its working frequency band. A comparison of the hexagonal antenna in this chapter with previous four-port antenna designs and the proposed ones in Chapter 3 is listed in Table. 5-D. The comparison shows that the proposed antenna has obviously wider bandwidth than any previous work while maintaining high port-to-port isolation.

## References

- [1] T. Svantesson, "An antenna solution for mimo channels: the multimode antenna," in *Conference Record of the 34th Asilomar Conference on Signals, Systems and Computers (Cat. No.00CH37154)*, vol. 2, 2000, pp. 1617–1621.

Table 5-D: Comparison of several four-port antennas

Antennas Types	Rectangular ant. in [9]	Ring ant. in [10]	Square ant. in [11]
Feed Network Needed?	Yes	Yes	No
Frequency Band	around 2.3 ~ 2.5 GHz	around 3.2 ~ 5 GHz (−6 dB reference)	1.85 ~ 2.95 GHz
Relative Bandwidth	8.4%	43.55% (−6 dB reference)	45.8%
Outer Dimension at $f_c$	$0.8\lambda(f_c) \times 0.32\lambda(f_c)$	$0.42\lambda(f_c) \times 0.42\lambda(f_c)$	$1.12\lambda(f_c) \times 0.96\lambda(f_c)$
Reference Coupling	< −12 dB	< −15 dB	< −15 dB
Antennas Types	Square ant. in [4]	Circular patch ant. in [12]	Original hex. ant. W/O loadings in Ch. 3
Feed Network Needed?	Yes	No	Yes
Frequency Band	6 ~ 8.5 GHz	2.5 ~ 2.72 GHz	3.43 ~ 4.92 GHz
Relative Bandwidth	34%	8.4%	36.7%
Outer Dimension at $f_c$	$0.85\lambda(f_c) \times 0.85\lambda(f_c)$	$0.52\lambda(f_c) \times 0.52\lambda(f_c)$	$0.9\lambda(f_c) \times 0.78\lambda(f_c)$
Reference Coupling	< −20 dB	< −18 dB	< −20 dB
Antennas Types	Proposed hex. ant. W/ lumped loadings in Ch. 3	Proposed hex. ant. W/ distributed loadings in Ch. 3	Proposed wide band hex. ant. in this Ch.
Feed Network Needed?	Yes	Yes	Yes
Frequency Band	2.17 ~ 3.45 GHz	2.21 ~ 3.40 GHz	3 ~ 6 GHz
Relative Bandwidth	45.5%	42%	66.6%
Outer Dimension at $f_c$	$0.84\lambda(f_c) \times 0.73\lambda(f_c)$	$0.84\lambda(f_c) \times 0.73\lambda(f_c)$	$1.4\lambda(f_c) \times 1.2\lambda(f_c)$
Reference Coupling	< −20 dB	< −20 dB	< −20 dB

- [2] M. Bouezzeddine and W. L. Schroeder, “Design of a wideband, tunable four-port mimo antenna system with high isolation based on the theory of characteristic modes,” *IEEE Transactions on Antennas and Propagation*, vol. 64, no. 7, pp. 2679–2688, Mar. 2016.
- [3] J. Molins-Benlliure, E. Antonino-Daviu, M. Cabedo-Fabrs, and M. Ferrando-Bataller, “Four-port wide-band cavity-backed antenna with isolating x-shaped block for sub-6 ghz 5g indoor base stations,” *IEEE Access*, vol. 9, pp. 80 535–80 545, 2021.
- [4] D. Manteuffel and R. Martens, “Compact multimode multielement antenna for indoor uwb massive mimo,” *IEEE Transactions on Antennas and Propa-*

- gation, vol. 64, no. 7, pp. 2689–2697, Mar. 2016.
- [5] H. Jaafar, S. Collardey, and A. Sharaiha, “Optimized manipulation of the network characteristic modes for wideband small antenna matching,” *IEEE Transactions on Antennas and Propagation*, vol. 65, no. 11, pp. 5757–5767, 2017.
- [6] J. L. Ethier and D. A. McNamara, “Antenna shape synthesis without prior specification of the feedpoint locations,” *IEEE Transactions on Antennas and Propagation*, vol. 62, no. 10, pp. 4919–4934, July 2014.
- [7] A. M. Abbosh and M. E. Bialkowski, “Design of compact directional couplers for uwb applications,” *IEEE Transactions on Microwave Theory and Techniques*, vol. 55, no. 2, pp. 189–194, Feb. 2007.
- [8] S. Y. Zheng, W. S. Chan, and K. F. Man, “Broadband phase shifter using loaded transmission line,” *IEEE Microwave and Wireless Components Letters*, vol. 20, no. 9, pp. 498–500, June 2010.
- [9] S. K. Chaudhury, H. J. Chaloupka, A. Ziroff, S. Ag, C. T. Ps, and D. Munich, “Novel MIMO Antennas for Mobile Terminal,” in *Proceedings of the 38th European Microwave Conference*, 2008, pp. 1751–1754.
- [10] E. Antonino-Daviu, M. Cabedo-Fabres, M. Gallo, M. Ferrando-Bataller, and M. Bozzetti, “Design of a multimode mimo antenna using characteristic modes,” in *2009 3rd European Conference on Antennas and Propagation*, pp. 1840–1844.
- [11] A. Moradikordalivand, T. A. Rahman, and M. Khalily, “Common Elements Wideband MIMO Antenna System for WiFi / LTE Access-Point Applications,” *IEEE Antennas and Wireless Propagation Letters*, vol. 13, pp. 1601–1604, 2014.
- [12] D. Yang, H. Zeng, R. Chen, J. Qu, Y. Wen, and S. Liu, “Four port compact multimode patch antenna system for vehicular application,” *2016 IEEE*

*International Workshop on Electromagnetics, iWEM 2016 - Proceeding*, pp. 21–23, 2016.

# Chapter 6

## Base Station Antenna Radiation Control with Sub-Structure TCM

### 6.1 Introduction

In the previous chapters, TCM has primarily been employed as a means to excite CMs for the purpose of antenna construction (Chapter 3), as well as to evaluate and then analyse radiation and coupling energy (Chapters 4 and 5). Therefore, the focus of the earlier chapters was mainly on the bandwidth, isolation, and additional port numbers of multiport antennas. However, the radiation performance of multiport antennas has not yet been discussed. In this chapter, the application of TCM on multiport antenna radiation will be comprehensively explored, with TCM being employed to control the radiation characteristics of base station (BS) antennas. For a dual-port BS antenna unit, the port number and coupling, which were the main focus of TCM in the previous discussions, are no longer the most challenging aspects. Instead, the degradation of beamwidth at high frequencies

becomes the primary concern. Therefore, dual-polarized antennas present an ideal scenario for extending the application of TCM on multiport antenna as discussed in this paper.

Along with the extensive increase of global mobile data traffic and developing of modern communication techniques, there has been a rising requirement for BS antenna design.

The first challenge encountered in BS antenna design is achieving a sufficiently wide bandwidth, in order to support multiple systems (2G/3G/LTE) and standards. Various studies have proposed BS antennas that exhibit excellent impedance matching across a wide bandwidth [1–3]. Undoubtedly, TCM involves a lot in this field [4, 5]. Parasitic elements are introduced in those studies so that new CMs occur, resulting in new resonances and consequently widen the bandwidth.

In addition to impedance bandwidth, a more challenging task is to achieve relative stability of the radiation pattern across a wide frequency range. A consistent beamwidth is essential for ensuring reliable signal coverage and maintaining a robust wireless connection. In urban areas [6], it is necessary to maintain the half-power beamwidth (HPBW) at approximately  $65^\circ$ . However, achieving wide bandwidth and stable wide beamwidth in the design of BS antennas is a challenging task, particularly because the beamwidth tends to significantly degrade at higher frequencies. In [2], a folded dipole antenna excited by a pair of L-shape crossed balun was proposed. Two pairs of current path on the folded arms were set to increase the stability of HPBW in a range of  $66.5^\circ \pm 5.5^\circ$  at  $1.69 \sim 2.71$  GHz. In [3], a broadband dual-polarized antenna working at  $1.7 \sim 2.7$  GHz was introduced and enhanced. A couple of parasite components were added near the antenna to improve the HPBW at high frequency.

Although there are various realizations of TCM in BS antenna design [4, 5, 7–11], controlling its radiation pattern remains a relatively uncommon approach.

In [12, 13], TCM has been used to enhance radiation stability, but the antenna configurations and application differ from those of BS antennas. In [9–11], the analysis of an BS arrays' radiation pattern is conducted. However, this analysis is limited to ideal scenarios involving dipoles and is not related to practical BS design.

In this work, the focus will be on radiating pattern of multiport antenna from a TCM perspective. Sub-structure TCM is used to analyse a  $\pm 45^\circ$  dual-polarized BS antenna unit and separate the antenna from the ground plate. Unlike the previous work, the antenna modes and corresponding ground modes are also studied. Modifications have been made to enhance the beamwidth stability over the entire band. The HPBW variation range is improved from  $25^\circ$  to  $20^\circ$  over the whole band after the modification. Furthermore, the previously introduced MEOC will also be utilized for analysing radiation mechanism across a wide frequency band. All calculation of TCM in this chapter are performed using the MATLAB environment with impedance matrix generated from FEKO. The final antenna design is simulated in CST Microwave Studio.

## 6.2 Sub-structure Characteristic Mode Theory and BS Antennas

### 6.2.1 Sub-structure Characteristic Mode Theory

Firstly presented by Garbacz and Turpin in 1971 [14], the TCM was then refined and analysed with comprehensive depiction by Harrington *et al.* with linear operators [15], [16]. The theory started from analysing the scattering problem related



to a conducting surface. The impedance matrix  $[Z]$  of the conducting body, which is usually obtained from method of moments (MOM) as [14]

$$[Z]J = [V], \quad (6.1)$$

is solved with a generalized eigenvalue problem

$$[X]J_n = \omega_n[R]J_n, \quad (6.2)$$

where  $J$  is the surface current,  $[V]$  is the incident voltage,  $[X],[R]$  are the real and imaginary parts of impedance matrix  $[Z]$ ,  $\omega_n$  is the  $n^{th}$  Characteristic Mode (CM), and  $J_n$  is the  $n^{th}$  modal current.

In the conventional definition of TCM, the scattering body, no matter how complex the structure might be, is regarded as a whole conducting surface. It works well on the analysis of many antenna types, e.g., dipole, monopole, ring antenna, etc. However, for other antennas with composite structures (e.g., patch antenna, antenna on mobile chassis), the conventional TCM is insufficient to cover the problem, since those antennas may include lossy materials, volume meshes or non-radiate components. EFIE In [17], the sub-structure TCM was introduced to focus the on the PEC radiator instead of the whole structure. In sub-structure TCM, the antenna is divided into two parts: the main radiator (denoted as  $A$ ), and secondary structure (denoted as  $B$ ). (6.1) is partitioned into blocks as

$$\begin{bmatrix} Z_{AA} & Z_{AB} \\ Z_{BA} & Z_{BB} \end{bmatrix} \begin{bmatrix} J_A \\ J_B \end{bmatrix} = \begin{bmatrix} V_A \\ V_B \end{bmatrix}, \quad (6.3)$$

where  $Z_{AA}$  and  $Z_{BB}$  are the self matrices for object  $A$  and  $B$  separately and  $Z_{AB}$

and  $Z_{AB}$  are matrices represent the interaction between  $A$  and  $B$ .  $J_A$ ,  $V_A$  are current and incident voltage on  $A$  respectively.

In most cases, especially when it is BS antenna which consists of two parts, the excitation only happens on the object  $A$ , the radiator, while there is no exterior excitation on the secondary structure. Therefore  $[V_B] = 0$ , and (6.3) can be rewritten as

$$\begin{aligned} Z_{AA}J_A + Z_{AB}J_B &= V_A \\ Z_{BA}J_A + Z_{BB}J_B &= 0. \end{aligned} \tag{6.4}$$

Substitute the second equation in 6.4 into the first to replace  $J_B$  and get

$$\begin{aligned} [Z_{AA} - Z_{AB}(Z_{BB})^{-1}Z_{BA}][J_A] &= [V_A] \\ [Z_{sub}] &= [Z_{AA} - Z_{AB}(Z_{BB})^{-1}Z_{BA}]. \end{aligned} \tag{6.5}$$

The new impedance matrix  $Z_{sub}$  in (6.5) is used for the sub-structure TCM decomposition

$$[X_{sub}]J_n^A = \omega_n^A[R_{sub}]J_n^A, \tag{6.6}$$

where  $J_n^A$  and  $\omega_n^A$  are the  $n_{th}$  modal current and eigenvalue for radiator A in the presence of structure B, respectively, and  $[X_{sub}]$  and  $[R_{sub}]$  are the imaginary and real parts of  $[Z_{sub}]$ .  $J_n^A$  is the  $n^{th}$  modal current on object A.  $J_n^A$  is similar to those in the conventional TCM and has same properties. The modal currents and fields of sub-structure TCM inherit the orthogonality of conventional ones. The modal current on object  $B$  is calculated with

$$J_n^B = -[Z_{BB}]^{-1}[Z_{BA}]J_n^A, \tag{6.7}$$

where  $J_n^B$  is the  $n^{th}$  mode on object  $B$ , or ground in a BS scenario. For the ground modes,  $J_n^A$  represents the coming electronic magnetic excitation from antenna which transmits through the interaction  $[Z_{BA}]$  and maps to ground board.

The excitation of the sub-structure modes resembles the conventional ones

$$\begin{aligned} J_A &= \sum_n \frac{V_{1n}^i J_n^A}{1 + j\omega_n^A} \\ J_B &= -[Z_{BB}]^{-1}[Z_{BA}] \sum_n \frac{V_{1n}^i J_n^A}{1 + j\omega_n^A}, \end{aligned} \quad (6.8)$$

in which  $V_{1n}$  is the MEC on the object  $A$ .

In order to examine the radiation and coupling for BS antennas, MEOC in (4.9) in chapter 4 is rewritten here as

$$M_{in} = \frac{1}{\sqrt{1 + (\omega_n^A)^2}} \frac{V_i I_n(p) l_p}{\sqrt{P_{radi}}}. \quad (6.9)$$

$M_{in}$  is the MEOC of  $n_{th}$  CM of the object  $A$  in the presence of structure  $B$  on port  $i$ .

From (6.7) to (6.9), Sub-structure TCM separates the main radiator from the passive radiator, and for the main radiator, the separated CM still inherits the characteristics of the original CM.

The most significant advantage of sub-structure TCM is that it abandons most of the redundant CMs in conventional TCM. When dealing with a BS array unit in which the ground size is much larger than the antenna, conventional TCM leads to a large number of unnecessary modes that seriously interfere with the analysis. This is because that the operating wavelength, which is comparable to the main radiator size, is much smaller than the ground size. Using the sub-structure TCM not only greatly reduces the number of dominant CMs but also focuses the analysis on the antenna's radiation.

## 6.2.2 Sub-structure TCM Analysis on Base Station Antennas

BS antennas have been playing an indispensable part in modern wireless communications. The common basic element of a BS array is usually composed of a dipole antenna and a long flat reflector below it. The antenna is fed with external source while reflector reflects EM waves coming from antenna. Therefore, the BS antenna is naturally divided into two parts, which enables the utilization of Sub-structure TCM.

Fig. 6.1(a)(b) is a typical broadband BS antenna [18]. The antenna is an unit of a  $\pm 45^\circ$  dual-polarized broadband antenna array with spline-edged bowties as the radiator. This array works at a wide band of  $1.427 \sim 2.9$  GHz and serves as a good candidates for BS. As shown in Fig. 6.1, the antenna unit consists two crossed bowtie dipoles, which are fed with two coaxial cables. Another two conducting cables are added at symmetrical positions. The design parameters are annotated in the figure. There is just one problem with the design: the radiation pattern, including HPBW, deteriorates significantly at high frequency.

The radiation performance [18] at  $1.427 \sim 2.9$  GHz is drawn in Fig. 6.2. The red solid line represents the HPBW variation over the whole band. It begins around  $77^\circ$  and reaches its minimum at approximately 2.7 GHz. After reaching the minimum, it gradually increases and reaches  $55^\circ$  at 2.9 GHz. Additionally, the blue solid line on the graph represents the relationship between antenna gain and frequency. As the frequency increases, the gain also increases, resulting in a narrower HPBW.

To analyse and improve this instability, the Sub-structure TCM is used to isolate

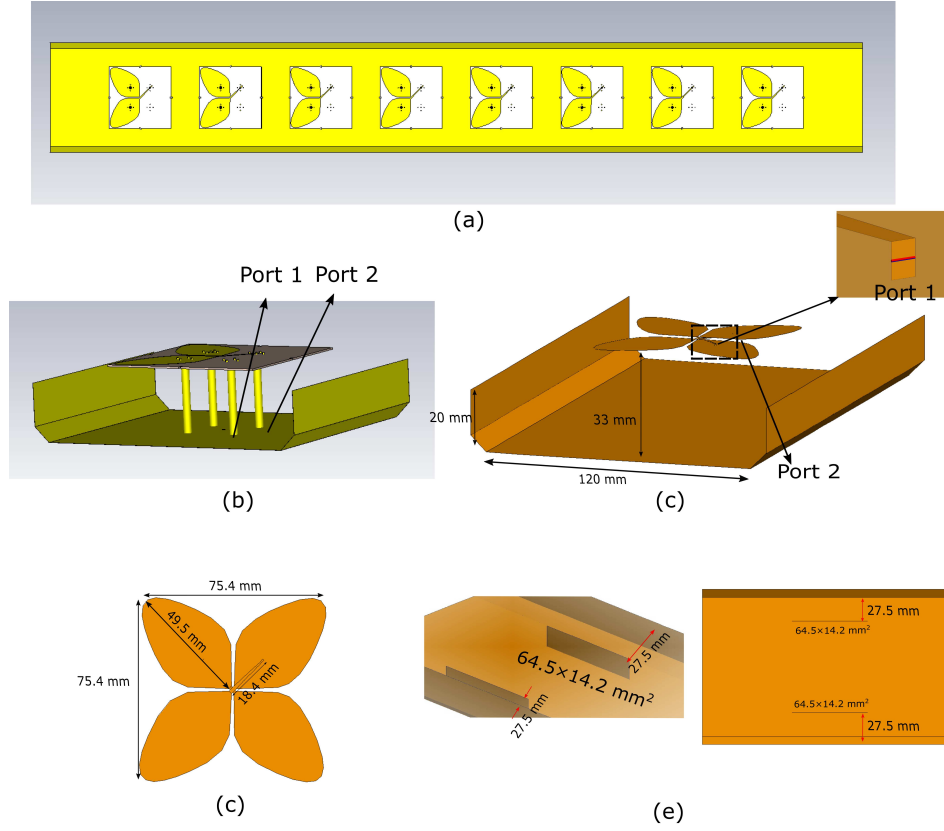


Figure 6.1: (a) The original BS array configuration [18]. (b) The original BS antenna unit [18], where the antenna is fed by two coaxial cables. The feeding coaxial cables are pointed out by arrows. Another two conducting cables are added for symmetry. (c) The antenna unit with feed cable omitted. The new feeding configuration enables the calculation of MEOC. (d) The aerial view of the antenna. (e) Two different views of the ground plate with two extra strips to improve beamwidth stability. The relevant parameters have been annotated in the figure.

the antenna from ground and decompose its radiation. Assuming all the feeding cables are well-balanced and generate no extra radiations, the antenna structure is simplified as in the Fig 6.1 (c), where the coaxial feedings degenerate into edge ports in FEKO. The simplified structure can be easily divided into two parts, the radiator (object  $A$ ) and ground reflector (object  $B$ ). By utilizing (6.5) and (6.7),

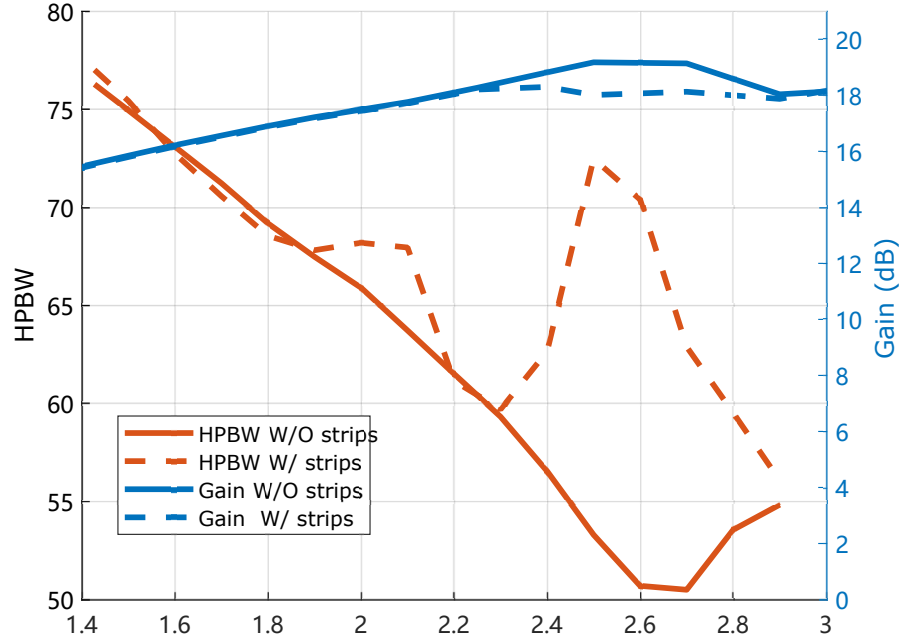


Figure 6.2: The comparison of HPBW and Gain before and after the modification. The details for the extra strips can be found in Fig. 6.1(e).

the radiator modes in the existence of the ground plane are isolated and then calculated.

#### 6.2.2.1 Comparison between Conventional and Sub-structure TCM

Before the actual examination on the radiation is implemented, a comparison between the conventional TCM and sub-structure TCM is given here to show the advantages of sub-structure TCM on two-object structure.

Table 6-A listed the characteristic angle (CA) [19] of the first 16 modes of the mentioned antenna at 2.5 GHz decomposed by conventional TCM and sub-structure TCM, respectively. According to [19], characteristic modes that have the potential

to radiate should have its CA  $\alpha_n$  in a range of  $135^\circ \leq \alpha_n \leq 225^\circ$ . If  $\alpha_n$  is beyond this range, this mode is considered as lacking the ability to radiate. Thus, CA  $\alpha_n$  plays a crucial role in filtering and identifying the required modes within a limited range.

As evident from the CAs, when conventional TCM is used to decompose the whole structure of the BS antenna in Fig. 6.1, all the first 16 modes (in bold style) listed in the first row of Table 6-A are capable of contributing to the radiation ( $135^\circ \leq \alpha_n \leq 225^\circ$ ). However, in the second row, which describes the resonance of the radiator only rather than the entire structure, only the first a few modes exhibit such behavior. This is because the ground plane has a significantly larger electrical size than the radiator, resulting in a larger number of ready-to-radiate modes. It is not practical to examine radiations of such a large number of modes. However, the presence of the ground plane must be taken into consideration to enable later modifications on it. The conventional TCM meets its shortcoming. On the other hand, the third row in Table 6-A is the CAs calculated by sub-structure TCM. The CAs of each mode in the third row closely correspond to those listed in the second row.

Thus, sub-structure TCM describes the resonance of the radiator in the presence of the reflector. It separates two components of the system, avoids the interference from higher-order modes of the ground plane, and helps to concentrate on the resonance on the radiator.

Table 6-A: The characteristic angles of the first 16 modes of the BS antenna composed by TCM and sub-structure TCM (sub-TCM) at 2.5 GHz. The modes capable of radiating are written in bold style.

	Mode1	Mode2	Mode3	Mode4	Mode5	Mode6	Mode7	Mode8
by TCM (whole structure)	<b>180.51</b>	<b>178.78</b>	<b>181.4</b>	<b>174.73</b>	<b>171.1</b>	<b>170.8</b>	<b>169.58</b>	<b>166.87</b>
by TCM (radiator only)	<b>201.87</b>	257.65	258.51	264.11	265.69	92.99	92.94	268.29
by sub-TCM	<b>178.51</b>	248.45	250.19	259.06	263.98	267.87	91.98	268.63
	Mode9	Mode10	Mode11	Mode12	Mode13	Mode14	Mode15	Mode16
by TCM (whole structure)	<b>163.5</b>	<b>159.45</b>	<b>157.25</b>	<b>207.83</b>	<b>148.12</b>	<b>145.6</b>	<b>218.43</b>	<b>221.26</b>
by TCM (radiator only)	268.31	91.67	90.48	269.66	90.13	269.93	90.07	90.05
by sub-TCM	91.35	91.1	90.24	269.78	90.12	269.91	90.03	90.03

### 6.2.2.2 Antenna CMs in the Presence of the Ground Plate

With the help of mode tracking algorithm [20, 21] and MEOC calculation in sub-structure TCM (6.9), Fig. 6.3 is drawn to illustrate the variation of the dominant modes with frequency. The left side of Fig. 6.3 demonstrates that the dominant modes on the antenna occupy the majority radiation power from the antenna of  $+45^\circ$  polarization. From top to bottom, the tracking result of modes from low frequency 1.5 GHz to high frequency 3 GHz is illustrated. Given that the summation of MEOC should be 1 as (4.10), it is worth mentioning that some of the bar length sums in Fig. 6.3 does not equal 1 because the other modes, aside from the four dominant ones, have been omitted.

According to their current and radiation pattern, it is noticed that at each frequency, the dominant modes can be roughly categorized as vertical and horizontal modes. The two types of modes act simultaneously and generate the  $+45^\circ$  polarisation. At lower frequency, the dominant modes can be named as the 'dipole-like' modes 1 & 2, for their radiation acts in a very similar way as a typical dipole antenna. As frequency increases, the 'dipole-like' mode radiation becomes more



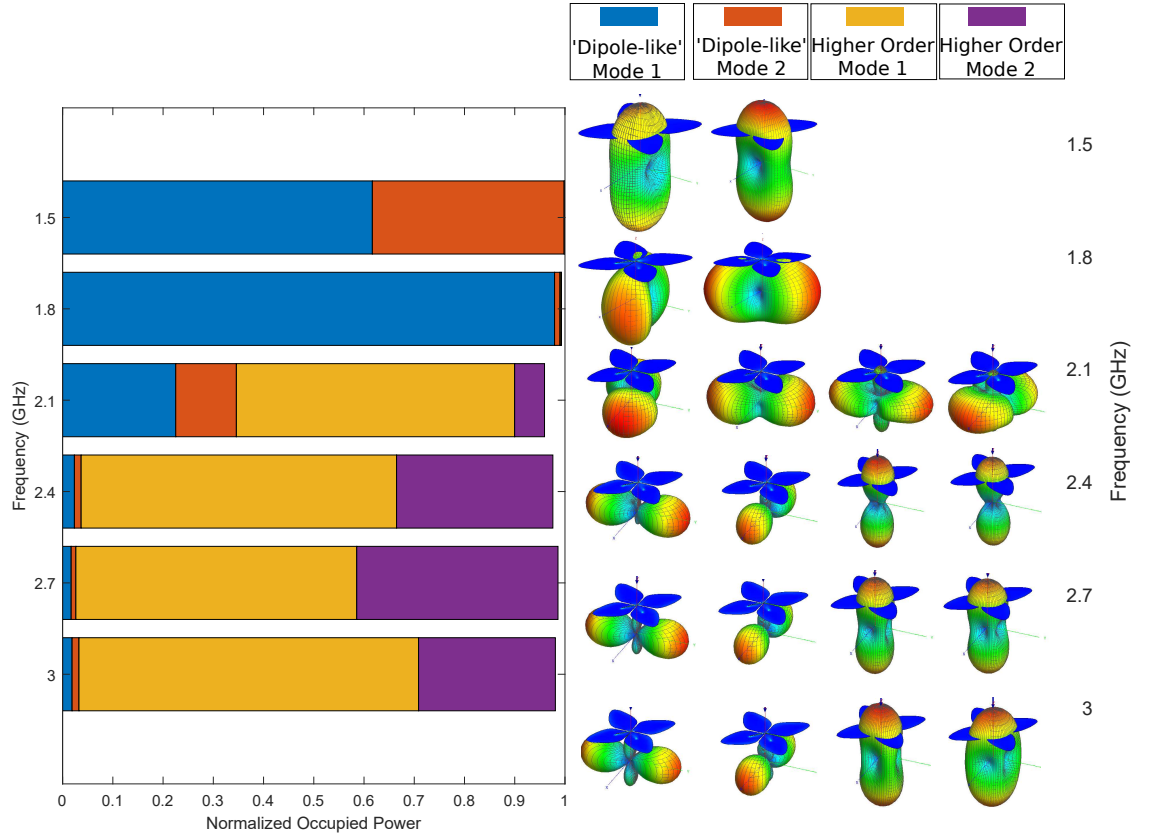


Figure 6.3: The dominant mode's occupied power (Left) and pattern (Right) variation with frequency. From top to bottom, the tracking result of modes from low frequency 1.5 GHz to high frequency 3 GHz is illustrated.

and more flat and tend to be end-fire patterns. Their occupancy rate on radiation power also decreases.

Meanwhile, a new kind of modes (named as 'Higher order' Mode 1 and 2) with broadside radiation pattern appears and starts to take up much of the antenna radiation. At high frequency, e.g., 2.7 GHz, the  $+45^\circ$  polarisation is almost completely dominated by the new 'higher-order' modes, while the 'dipole-like' modes radiate end-fire patterns and take up only a little share of the radiation.

In general, Fig. 6.3 shows that at lower frequency, like 1.4 GHz, it is the 'dipole-like' modes that dominates the radiation, while at higher frequency 2.7 GHz, higher-

order mode 1, 2 dominates the radiation. Additionally, the raise of higher order modes explains why the HPBW curves in Fig. 6.2 goes down at higher frequency.

Due to its limited size, any minor modification on the radiator (antenna) is very likely to disrupt the mechanism of the original design and degenerate the performance. It is best to look at the ground plate where there is enough space and much freedom to modify. Thanks to the sub-structure TCM, a close look at the ground mode with respect to the dominant modes of the antenna in Fig. 6.3 is possible.

### **6.2.2.3 Ground CMs with respect to antenna CMs**

The ground modes corresponding to the antenna modes, are calculated following the equation (6.7). The dominant ones' current distribution (left column) and radiation pattern (right column) are drawn in Fig. 6.4. Similar to the antenna modes, the two dominant modes at each frequency can be roughly categorized as vertical and horizontal modes, according to the current distributions. These two types of modes make up the  $\pm 45^\circ$  polarization. As shown in the chart, the dominant ground modes at different frequencies contrast with each other, which coincides with their counterpart modes on the antenna.

The current distribution reveals that the 'dipole-like' modes exhibit currents in the same direction near the central region. As for the higher-order modes 1', the modal current flows parallel to the longer edges of the ground plate. Their beamwidths on the right side of Fig. 6.4 are relatively wide. In contrast, the current distributions of higher order modes 2' have notable discontinuities near the central area, where

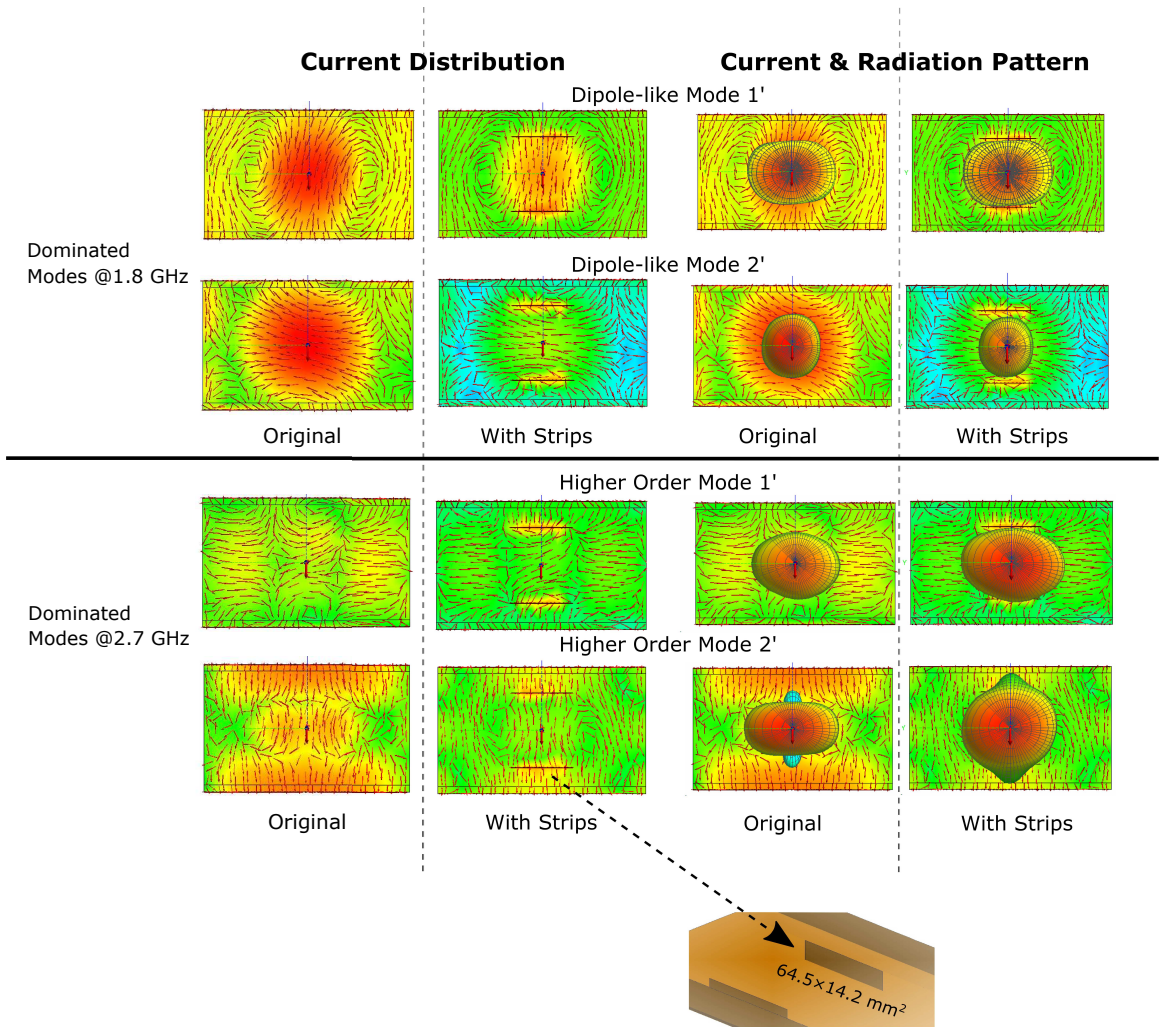


Figure 6.4: The dominant modes current and pattern comparison before and after the modification at 2.7 GHz.

currents with opposite directions flow out. As a consequence, the generated far fields by those currents cancel each other and thus attenuate the beamwidth. That is why in Fig. 6.4, the radiation pattern of 'higher order' mode 2' appears to be much narrower than all the other modes.

Therefore, the ground mode, higher order modes 2', is chosen for its narrow beamwidth in Fig. 6.4. It will be suppressed, in order to improve the stability of overall beamwidth.

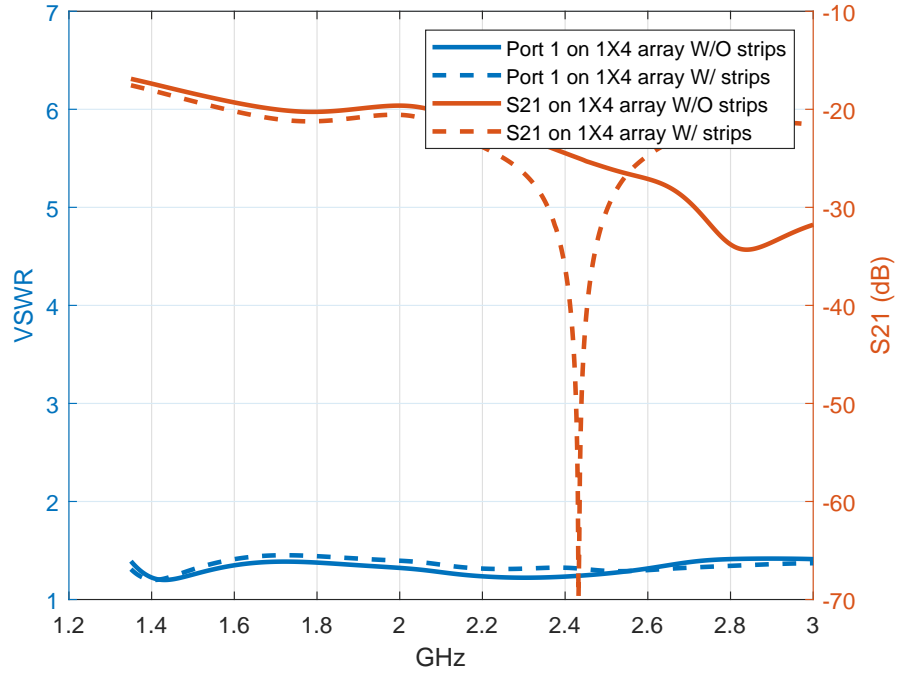


Figure 6.5: The VSWR and  $S_{21}$  comparison before and after the modification.

### 6.2.3 Modification to Improve Radiation Stability

The vicinity of the current discontinuities of the higher order mode  $2'$  in Fig. 6.4 shows that currents flow in different directions and has weak magnitudes, which implies intense surface charges in the vicinity area, according to Gauss's law. To compensate the cancellation of opposite currents in far-field, two vertical strips (shown in Fig. 6.1 and Fig. 6.4) are then put on the symmetric discontinuities of higher order mode  $2'$  on the ground plate. The strips generate vertical currents to the ground plane and thus attenuate the opposite currents. The size of the strip is  $64.5 \times 14.2 \text{ mm}^2$ . The length of the strips is chosen so that the discontinuities of higher order mode 2 are fully covered.

Fig. 6.4 shows that the discontinuities only exist on the higher order mode 2, and not on other ground modes. Thus, the currents of other ground modes should

bypass the strips easily. Therefore, the modification shall not affect other modes' functions and does little effect on the overall antenna performance.

The comparison of radiation patterns before and after the insertion of the plates is also depicted in the columns of Fig. 6.4. Apparently, the modification only changes the current distribution and radiation pattern of the higher mode 2 and barely affect the other dominant modes. The new strips weaken the reverse current in the center between the two strips and thus expand the beamwidth on the y direction. As a result, the stabilization of the HPBW is improved and other properties barely change.

This modification is utilized into the  $1 \times 4$  array. The simulation results of the modified array shown in Fig. 6.2 illustrate the improvement of the HPBW. With the extra strips, the red dashed curve stops dropping at higher frequency. The HPBW variation is improved from  $25^\circ$  to  $20^\circ$  in the frequency range of  $1.4 \sim 2.9$  GHz. The variation of gain at high frequencies has become smoother as well. It is noteworthy that the red dashed line in Figure. 6.2 remains indistinguishable from the red solid line until the frequency is higher than approximately 1.9 GHz. This aligns with Fig. 6.3, where higher order mode 2 gets significant after 1.8 GHz. Therefore, it is illustrated that only higher order mode 2 is sensitive to the extra strips, whereas the dominant 'dipole-like' modes at lower frequency are insensitive to them.

Additionally, Fig. 6.5 shows that the port reflections barely changes after the modification. The mutual couplings before and after the modification are also shown in the figure, which are both below  $-20$  dB.

## 6.3 Summary

In this work, the sub-structure TCM is used on the radiation improvement of dual-port BS antenna. Sub-structure TCM is used to isolate the antenna and study its mode variations when frequency increases. To prevent alterations on the antenna and degradation of its performance, the ground modes associated with the antenna modes are examined and modifications are made to enhance the beamwidth stability across the entire frequency range. The HPBW variation range is improved from  $25^\circ$  to  $20^\circ$  after the modification.

## References

- [1] Y. Liu, H. Yi, F.-W. Wang, and S.-X. Gong, “A novel miniaturized broadband dual-polarized dipole antenna for base station,” *IEEE Antennas and Wireless Propagation Letters*, vol. 12, pp. 1335–1338, 2013.
- [2] H. Sun, C. Ding, and Y. J. Guo, “A wideband base station antenna with reduced beam squint,” in *12th European Conference on Antennas and Propagation (EuCAP 2018)*, 2018, pp. 1–5.
- [3] Y. Cui, L. Wu, and R. Li, “Bandwidth enhancement of a broadband dual-polarized antenna for 2g/3g/4g and imt base stations,” *IEEE Transactions on Antennas and Propagation*, vol. 66, no. 12, pp. 7368–7373, 2018.
- [4] Y. H. Zhu and F. H. Lin, “Metasurface loaded dual-mode wideband dipole antenna using characteristic mode analysis,” in *2022 International Applied Computational Electromagnetics Society Symposium (ACES-China)*, 2022, pp. 1–2.
- [5] T. A. Vu, T. T. Do, D. N. Nguyen, V. X. T. Nguyen, T. T. Truong, D. H. T.

- Hoang, and M. T. Le, “Broadband dual-polarized antenna element for 5g base station using characteristic mode analysis,” in *2021 IEEE International Symposium on Antennas and Propagation and USNC-URSI Radio Science Meeting (APS/URSI)*, 2021, pp. 985–986.
- [6] N. Alliance, “Recommendation on base station active antenna system standards,” *NGMN Alliance, Frankfurt, Germany, Tech. Rep*, vol. 1, 2020.
- [7] D. Zhang, Y. Chen, and S. Yang, “An in-band decoupling technique for base station antennas,” in *2021 IEEE International Workshop on Electromagnetics: Applications and Student Innovation Competition (iWEM)*, vol. volume1, 2021, pp. 1–3.
- [8] L. Li, Y. He, L. Zhang, W. Li, and C. Song, “A broadband dual-polarized metasurface antenna for 5g mmwave communication using characteristic mode analysis,” in *2023 IEEE International Symposium on Antennas and Propagation and USNC-URSI Radio Science Meeting (USNC-URSI)*, 2023, pp. 641–642.
- [9] P. K. Gentner, “On the use of characteristic mode analysis for the design of antenna arrays,” in *2020 14th European Conference on Antennas and Propagation (EuCAP)*, 2020, pp. 1–5.
- [10] Y. Chen, W. Wang, S. Lian, S. Lou, H. Bao, L. Song, and G. Leng, “Far field pattern calculation for antenna array with displacement and rotation of elements using characteristic mode analysis,” in *2022 IEEE International Symposium on Antennas and Propagation and USNC-URSI Radio Science Meeting (AP-S/URSI)*, 2022, pp. 2072–2073.
- [11] P. K. Gentner and M. Pietzka, “Base station antenna array design with characteristic mode analysis,” in *2021 15th European Conference on Antennas and Propagation (EuCAP)*, 2021, pp. 1–5.
- [12] D. Wen, Y. Hao, H. Wang, and H. Zhou, “Design of a wideband antenna

- with stable omnidirectional radiation pattern using the theory of characteristic modes,” *IEEE Transactions on Antennas and Propagation*, vol. 65, no. 5, pp. 2671–2676, 2017.
- [13] D. Wen, Y. Hao, M. O. Munoz, H. Wang, and H. Zhou, “A compact and low-profile mimo antenna using a miniature circular high-impedance surface for wearable applications,” *IEEE Transactions on Antennas and Propagation*, vol. 66, no. 1, pp. 96–104, 2018.
- [14] R. Garbacz and R. Turpin, “A generalized expansion for radiated and scattered fields,” *IEEE Transactions on Antennas and Propagation*, vol. 19, no. 3, pp. 348–358, May 1971.
- [15] R. Harrington and J. Mautz, “Theory of characteristic modes for conducting bodies,” *IEEE Transactions on Antennas and Propagation*, vol. 19, no. 5, pp. 622–628, Sep. 1971.
- [16] R. Harrington, J. Mautz, and Y. Chang, “Characteristic modes for dielectric and magnetic bodies,” *IEEE Transactions on Antennas and Propagation*, vol. 20, no. 2, pp. 194–198, Mar. 1972.
- [17] J. Ethier and D. McNamara, “Sub-structure characteristic mode concept for antenna shape synthesis,” *Electronics letters*, vol. 48, no. 9, pp. 471–472, 2012.
- [18] Q. Zhang and Y. Gao, “A compact broadband dual-polarized antenna array for base stations,” *IEEE antennas and wireless propagation letters*, vol. 17, no. 6, pp. 1073–1076, 2018.
- [19] M. Cabedo Fabres, “Systematic design of antennas using the theory of characteristic modes,” Ph.D. dissertation, 2008.
- [20] B. D. Raines and R. G. Rojas, “Wideband tracking of characteristic modes,” in *Proceedings of the 5th European Conference on Antennas and Propagation (EUCAP)*. IEEE, 2011, pp. 1978–1981.



- [21] Z. Miers and B. K. Lau, “Wideband characteristic mode tracking utilizing far-field patterns,” *IEEE Antennas and Wireless Propagation Letters*, vol. 14, pp. 1658–1661, 2015.

# Chapter 7

## Conclusion and Future Work

### 7.1 Conclusion

In this thesis, various multiport applications with TCM have been studied.

In chapter 3, a TCM study on planar plate is proposed firstly in this report. The relationship between the shape symmetry and degenerate CM pair is studied. A hexagonal antenna with four ports is firstly designed. Blended slots are inserted onto the hexagon plate to excite CMs simultaneously. In order to control the impedance bandwidth, a loading method is used onto the antenna. However the result is not satisfying although the common bandwidth is fulfilled, because the symmetrical structure is destroyed. In addition, the relationship between the inserted slots and overall multimode performance is discussed. The result implies that various slots with specific characteristic could be inserted onto the plate to get the resulting multimode inherit similar impedance property.

In Chapter 4, a novel method is presented, to evaluate the radiation energy and mutual coupling in multiport antennas. With the benefit of TCM, the radiation

and mutual coupling for multiport system are analysed with the modal energy occupied coefficients (MEOC). Moreover, the linear transformation of feeding network in multimode antenna system has been adopted to develop the modal based method.

Furthermore, this method is utilized to analyse and improve the performance of a four-port antenna as an example. The proposed hexagonal antenna is a four-port hexagonal antenna consisting a planar hexagonal plate, vertical tapered baluns and feeding network at the ground plane. The whole antenna works in  $3 \sim 6$  GHz and all its four ports are well-matched with high port-to-port isolation.

In the last chapter, an alternative version of TCM, i.e., the sub-structure TCM is introduced to analysis dual port antenna. This method specializes at dealing with the problem of a radiator with reflector. It is then used to study on a base station antenna. With the help of TCM tracking method, sub-structure TCM isolates the antenna unit of a typical dual-polarized base station from its ground and enables to study its CM variations when frequency increases. The ground modes corresponding to the antenna modes are also studied and modifications have been made to improve the beamwidth stability over the entire band. The HPBW variation range is improved from  $25^\circ$  to  $20^\circ$  after the modification.

## 7.2 Future Work

In this section, the potential applications and further research of the proposed topics are addressed for future work.

### 7.2.1 Radiation Pattern Synthesis

In the last chapter, sub-structure TCM has been used to analysis and improve the radiation of a dual-polarized antenna. It shows that TCM is a great candidate tool to synthesis the performance of antenna, especially for an antenna with a relatively wide frequency band or working at high frequency. When antenna works at lower frequency, only a few modes are excited and radiating, and conventional analysis methods and TCM have little difference dealing with it. When antenna works at higher frequency (physical size  $> \lambda$ ), multiple modes are excited and would be too complicated to handle if not using TCM to divide them into modes.

### 7.2.2 Applications on MIMO Antenna

Multiport antennas have been discussed and analysed in this thesis. Exploiting applications of TCM on MIMO antenna design would be an interesting task, especially at millimeter wave. Recent applications stay on simple planar structures while TCM also works on a three-dimension condition, which could lead to a solid shape antenna design (e.g. the outer shell of a device) or make synthesis on the placement of antenna element for massive array in 3-D space.

### 7.2.3 Broadband Antennas Design

It is known that characteristic modes resonating at different frequencies and it is possible to combine some of them to make a broadband antenna. TCM provides a physical vision to view those modes with their resonating frequencies and enables designers to choose radiating modes. The tricky part is how to excite needed modes simultaneously while leaving alone unnecessary ones.

# Appendix A

## Author's publications

### Journal papers

1. **W. Su**, Q. Zhang and Y. Gao, "Base Station Antenna Ground Radiation Controlling Based on Sub-Structure Theory of Characteristic Mode," *IEEE Antennas Wireless Propag. Lett.* (submitted).
2. **W. Su**, Q. Zhang, S. Alkaraki, Y. Zhang, X. Zhang and Y. Gao, "Radiation Energy and Mutual Coupling Evaluation for Multimode MIMO Antenna Based on the Theory of Characteristic Mode," *IEEE Transaction on Antennas and Propagation*, vol. 67, no. 1, pp. 74-84, Jan. 2019.
3. Q. Zhang, R. Ma, **W. Su** and Y. Gao, "Design of a Multimode UWB Antenna Using Characteristic Mode Analysis," *IEEE Transaction on Antennas and Propagation*, vol. 66, no. 7, pp. 3712-3717, July 2018.

## Books

1. Y. Gao, **W. Su**, X. Zhang and Y. Cao, “Massive MIMO Antenna Designs,” *Wiley 5G Ref: The Essential 5G Reference Online (2019)*, 1-34.

## Conference papers

1. **W. Su**, Q. Zhang, S. Alkaraki and Y. Gao , “A Broadband Mutimode Antenna Based on the Theory of Characteristic Mode,” *IEEE International Symposium on Antennas and Propagation (AP-S)* , Atlanta, Georgia, USA June, 2019.
2. **W. Su**, Q. Zhang, and Y. Gao , “A Novel Method to Interpret the Mutual Coupling Based on Characteristic Mode Theory,” *European Conference on Antennas and Propagation (EuCAP)*, April 2019.